XNPIG 2019
X-ray and Neutron Phase Imaging with Gratings

5th International Conference on
X-ray and Neutron Phase Imaging with Gratings

Tutorial Lectures

20 October, 2019
Tohoku University, JAPAN

Opening address

Since the first meeting in 2012 (Tokyo, Japan), XNPIG conferences were held worldwide almost every two years, and we are excited to meet again for XNPIG2019 in Sendai, Japan. The field relevant to XNPIG is growing steadily and young scientists, students, and new faces are joining the field of X-ray and neutron phase imaging and contributing to the development of this field.

This time at XNPIG2019, the international advisory committee (IAC) has organized a tutorial session for the first time prior to the main conference. Lectures on fundamentals and historical views of X-ray and neutron phase imaging, grating fabrication, and image processing are arranged. IAC aims at promoting and encouraging young scientists, students, and new faces with the lectures. Another merit of this trial must be that the presenters at the main part of XNPIG2019 can use time more for their specific subjects following brief introductions.

The number of registered attendees of the tutorial session is as much as 81 including 25 students at the time of writing, exceeding the estimation of the local organizing committee. Although we needed to find a larger room for the session in haste, it was a nice surprise.

I greatly appreciate our lecturers for their presentations and preparations for this handout in advance. Feedbacks from attendees about the organization and the contents of the session are welcome to LOC. I expect that this trial is effective and succeeded in the future XNPIGs. Finally I wish everybody enjoy XNPIG2019 and the stay in Sendai, Japan.

Prof. Atsushi Momose
Chair of XNPIG2019

<u>XNPIG2019 Tutorial Lectures</u>

Sunday, 20 October 2019
(Auditorium at Bldg. 2, Institute for Material Research,
Katahira Campus, Tohoku University)

13:20 – 13:30	**Opening** Atsushi Momose, *Tohoku University, Japan*	
13:30 – 14:15	**Tutorial 1** **Historical view of X-ray imaging especially using phase information** Alessandro Olivo, *University College London, UK*	p.3
14:15 – 14:45	**Tutorail 2** **Historical view of neutron radiography** Dmitry A. Pushin, *University of Waterloo, Canada*	p.19
14:45 – 15:05	***Coffee Break***	
15:05 – 15:50	**Tutoral 3** **Introduction to phase imaging principles & potential applications** Franz Pfeiffer, *Technische Universität München, Germany*	p.33
15:50 – 16:20	**Tutorial 4** **Introduction to tomographic image reconstruction** Marco Stampanoni, *Paul Scherrer Institut / Eidgenössische Technische Hochschule Zürich, Switzerland*	p.51
16:20 – 16:40	***Coffee Break***	
16:40 – 17:10	**Tutorial 5** **Fabrication technology of gratings** Christian David, *Paul Scherrer Institut, Switzerland*	p.65
17:10 – 17:25	**Closing with expectation to XNPIG2019** Atsushi Momose, *Tohoku University, Japan*	

Tutorial 1

(13:30 – 14:15)

Historical view of X-ray imaging especially using phase information

Alessandro Olivo

University College London,

UK

L1-1

XNPIG 2019 — UCL

Historical view of X-ray imaging especially using phase information

Sandro Olivo, Spokesperson, AXIm Group
Medical Physics and Biomedical Engineering, UCL

https://www.ucl.ac.uk/medical-physics-biomedical-engineering/research/groups-and-centres/advanced-x-ray-imaging-group-axim

L1-2

XNPIG 2019 — UCL

Nov 8, 1895 (a Friday, so Roentgen could continue working through the weekend…)

And only 2 weeks later:

L1-3

XNPIG 2019 — UCL

Nov 8, 1895 (a Friday, so Roentgen could continue working through the weekend…)

Many years later:

L1-4

XNPIG 2019 — UCL

Diagnostic radiology

Graph 1: NHS imaging activity in England, March 2015 to March 2016

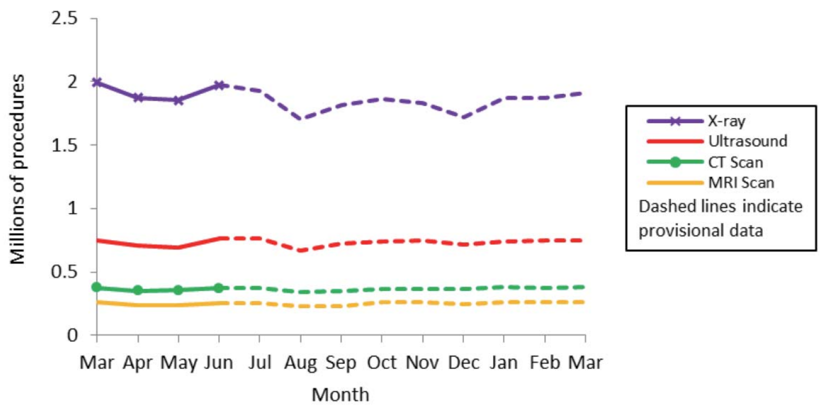

L1-5

How are x-rays generated?

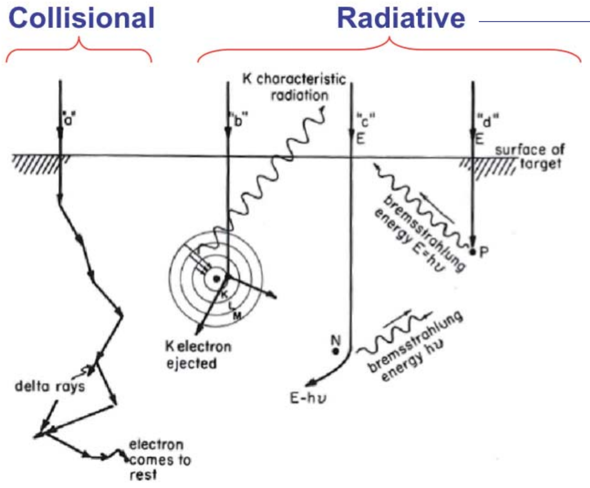

Only 1% of the total! X-ray tubes are very inefficient machines.

L1-6

The x-ray tube

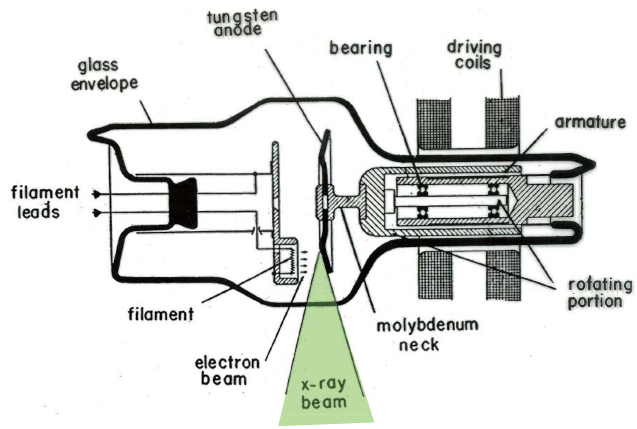

L1-7

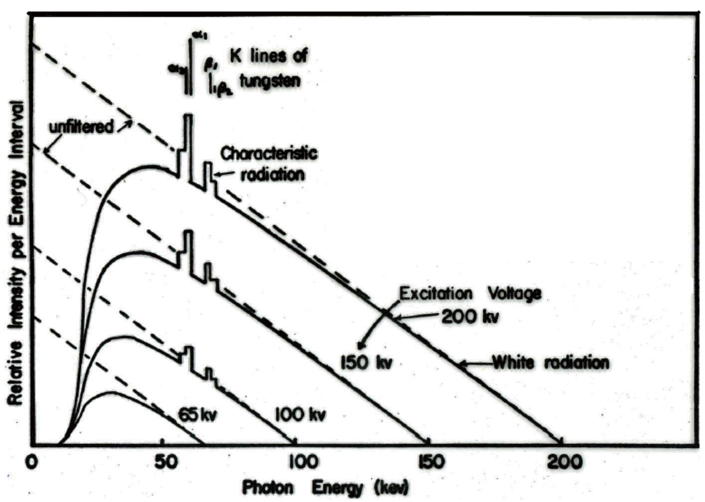

L1-8

Why triangular? Thin Target Theory

- Consider target thin enough so that every electron undergoes only **one** radiative interaction while passing through it
- Assume flat distribution for the energy of the emitted x-ray

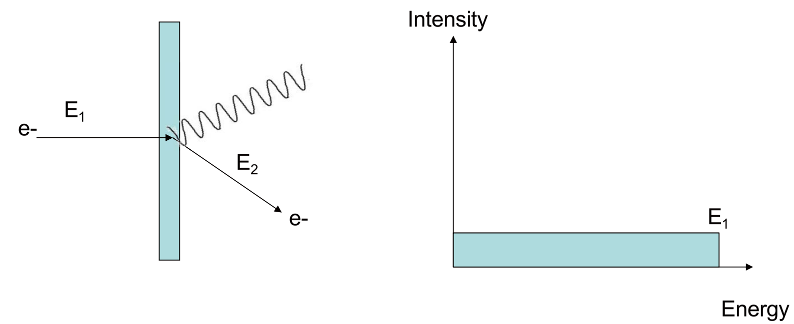

L1-9

XNPIG 2019 UCL

Thick Target

- Consider a thick target to be a number of thin targets superimposed, repeat process! (But with a lower energy every time because you've lost some in the previous step). You obtain a triangular shaped spectrum.

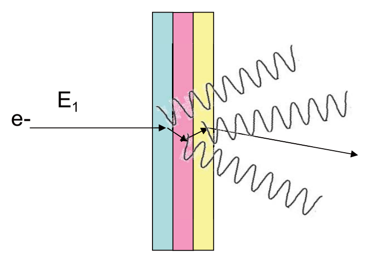

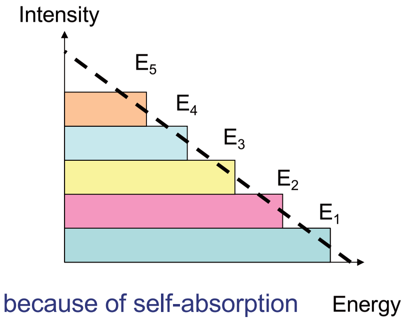

The triangle is "cut" at lower energies because of self-absorption

L1-10

XNPIG 2019 UCL

Lines -> Characteristic radiation

- The bombarding electron ionises the target atom (e.g. the k shell)
- an e$^-$ from a higher shell drops down to fill the vacancy

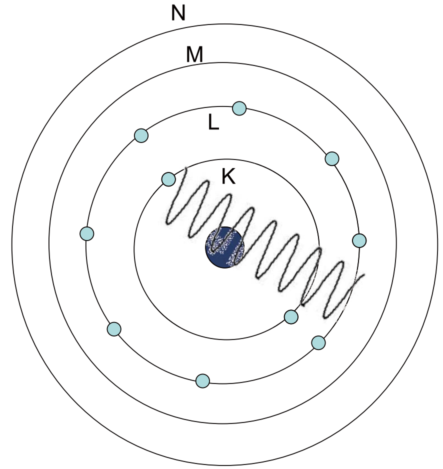

L1-11

XNPIG 2019 UCL

Energy of characteristic radiation

- Photon energy given by difference in energy levels
- Intensity of line depends on electron density in shells and quantum mechanics selection rules (including e.g. energy difference between shells)

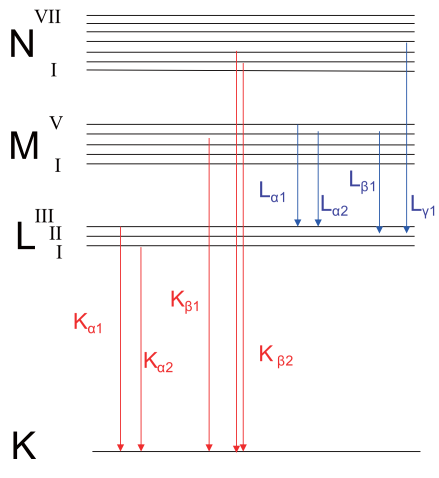

L1-12

XNPIG 2019 UCL

	Tungsten (Z=74)	Molybdenum (Z=42)
K	69.525	20.000
L_I	12.098	2.867
L_{II}	11.541	2.625
L_{III}	10.204	2.521
M_I	2.820	0.505
M_{II}	2.575	0.410
M_{III}	2.281	0.392
M_{IV}	1.871	0.230
M_V	1.809	0.228

L1-13

Processes

- Absorption
- Scatter

ATTENUATION

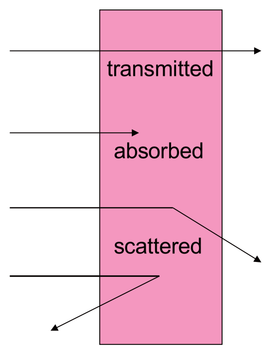

Attenuation is the removal of photons from the primary beam

L1-14

Compton scattering

- Incident **x-ray photon*** scattered by a loosely bound electron (= considered free in the calculations)
- Inelastic: energy of the scattered x-ray <energy of incident x-ray
- Incoherent-scattering centres (electrons) scatter independently

*NOTE: I tend to use "x-ray" or "photon" interchangeably

L1-15

Compton scattering

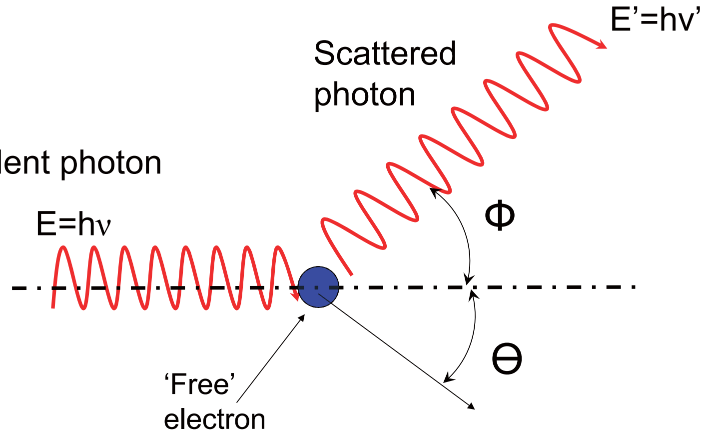

$E^2=p^2c^2 + m_o^2c^4$

L1-16

Some equations

- Wavelength shift

PHOTON scatt. angle

$$\lambda'-\lambda = \frac{h}{m_o c}[1-\cos\varphi]$$

- Scattered Photon energy

$$h\nu' = \frac{m_o c^2}{(1-\cos\varphi)+1/\alpha}$$

- Recoil electron kinetic energy

$$T = h\nu - h\nu' = h\nu . \frac{\alpha(1-\cos\varphi)}{1+\alpha(1-\cos\varphi)}$$

- Relation between scattering angles

$$\cot\vartheta = (1+\alpha)\tan(\varphi/2)$$

$\alpha = h\nu/m_0c^2$ i.e. it is the initial x-ray energy expressed in "electron rest masses"

L1-17

Probability of Compton Scatter

- Attenuation coefficient $\mu_{Compton} \propto \rho$

- Why do I express the probability with an attenuation coefficient?

BEER'S LAW $N=N_o e^{-\mu t}$ where N is the number of photons transmitted through a layer of material with thickness t and attenuation coefficient μ hit by N_o photons:

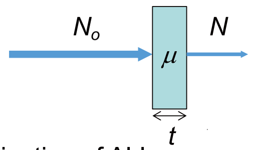

That "μ" is the combination of ALL processes that can remove photons from the initial beam i.e. $\mu = \mu_{\text{photoelectric}} + \mu_{\text{Compton}} + \mu_{\text{coherent}} + \mu_{\text{pair production}}$

↑ If beam collimated and small detector since coherent -> small-angle scattering (under μ_{coherent})

↑ If beam energy > 1.02 MeV (under $\mu_{\text{pair production}}$)

L1-18

Coherent Scattering

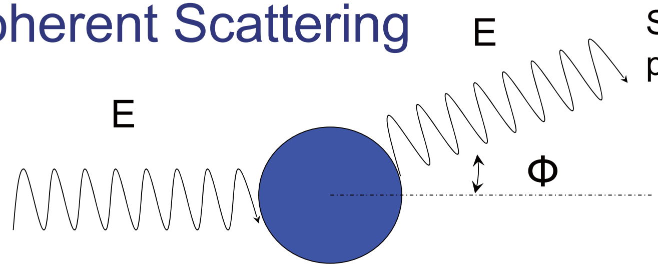

- Elastic scattering from bound atomic electrons (from the "electron cloud" of the atom)

- interaction is no longer with individual electrons but rather with the entire "electron cloud" – the whole atom takes up the recoil

L1-19

Coherent scattering is confined to small angles

Al	Z = 13	< 15° — 0.1 MeV
		< 2° — 1.0 MeV
Pb	Z = 82	< 30° — 0.1 MeV
		< 4° — 1.0 MeV

- SMALL CONTRIBUTION to the total cross section, especially at high x-ray energy

L1-20

Compton or Coherent scatter ?

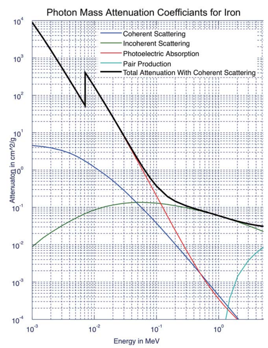

They coexist (see blue & green lines in graph on the left – but note the vertical scale is **logarithmic**!); Compton "takes over" after a certain energy which depends on the material.

Basically the probability depends on whether the electrons are seen as almost free or tightly bound, i.e. on the energy of the incoming x-ray compared to the binding energy of the electron (which depends on Z)

L1-21

Photoelectric Effect and Characteristic Radiation

- Photons incident on ***bound*** electrons can be totally absorbed as atom as a whole takes up recoil momentum
- **Photoelectric effect**
- The excited electron is then emitted with energy $T = h\nu - B_e$ where B_e is the binding energy of the electron
- Effect dominates at low energies (<< 0.1 MeV)

L1-22

Photoelectric effect

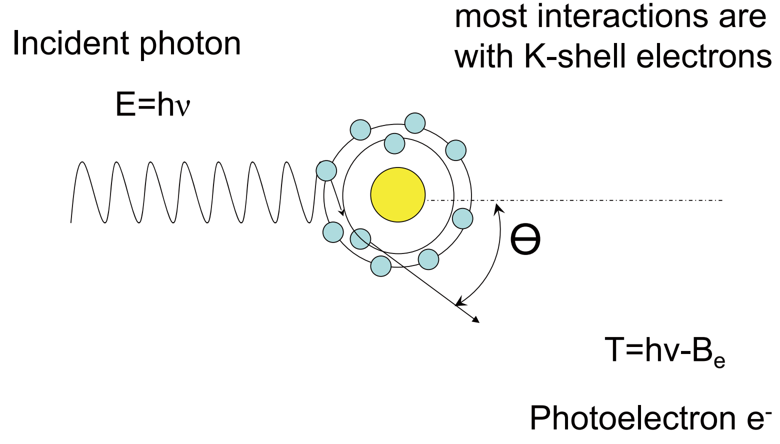

L1-23

What happens when the ionized atom de-excites?

Either

- Characteristic X-ray
  - Electron drops down from higher shell
  - Energy of x-ray depends on relative shell energies

Or

- Auger electron
  - Energy given to outer shell electron - emitted
  - More likely for low atomic number materials

L1-24

Fluorescence yield

- Relative probability of characteristic x-ray production compared to auger electron emission

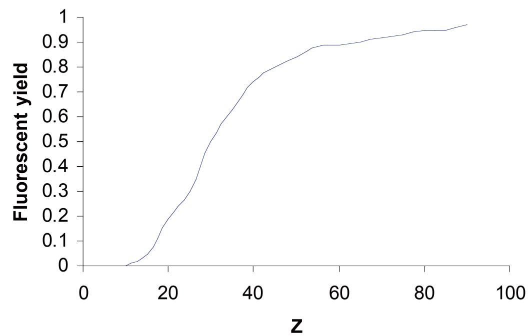

L1-25

Characteristic X-ray emission

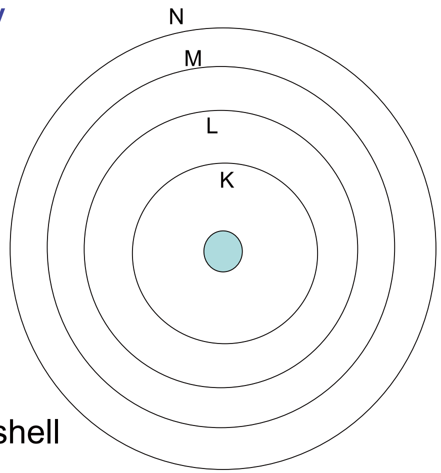

- Element: W
- K shell BE: 69.5
- L_{iii} shell BE: 10.2
- M_{iii} shell BE: 2.3

- If vacancy filled by L_{iii} shell electron hv=……. (K_β)

L1-26

Energy dependence

photoelectric cross-section varies with ~ $1/E^3$ - hence it constantly decreases but there are exceptions at attenuation edges.

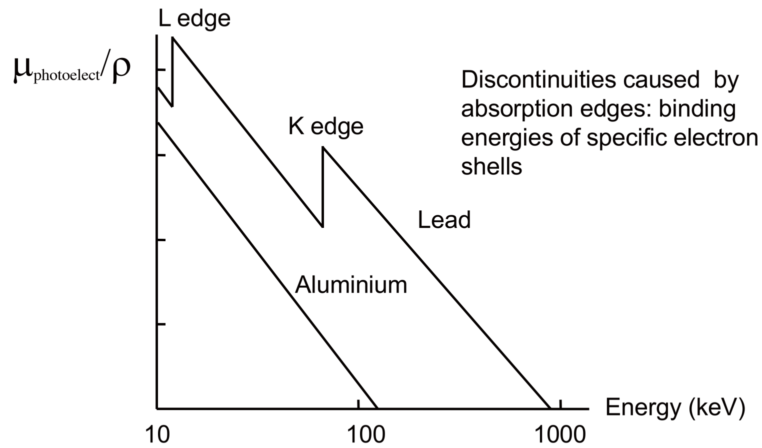

L1-27

Absorption Edges

- As the photon energy increases, photoelectric absorption decreases…

- So long as incident x-ray energy is less than binding energy of K-shell electron, x-rays can only kick out L and M shell electrons

- When the x-ray energy becomes greater than K shell binding energy, the attenuation coefficient for photoelectric absorption "jumps up" because the x-rays can now kick out **also K shell electrons** as well as L and M

L1-28

K-edges

- For low Z materials, Ek low (<1keV) so K edge not significant

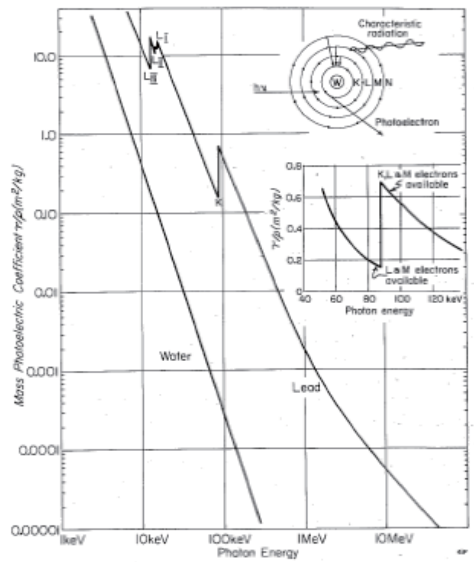

L1-29

Probability of Photoelectric absorption

- Attenuation coefficient

$$\mu_{photoelect} \propto \frac{Z^3 \rho}{E^3}$$

L1-30

- **Photons interact** and are removed from beam
- **Attenuation** (absorption + scattering) depends on:
  - Z
  - Density
  - Thickness
- Leads to variation in detected intensity

This is how we create an x-ray image

L1-31

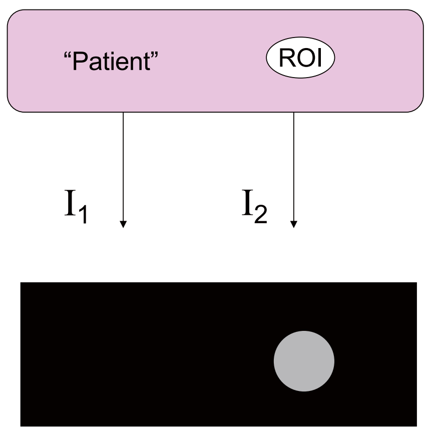

L1-32

Contrast: $C = \dfrac{(I_1 - I_2)}{I_1}$

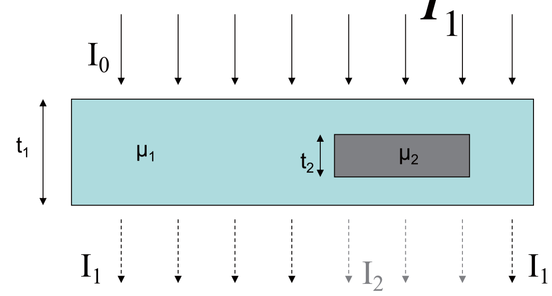

With:

$$I_1 = I_0 \exp(-\mu_1 t_1)$$
$$I_2 = I_0 \exp[-\mu_1 (t_1 - t_2)] \exp(-\mu_2 t_2)$$

L1-33

Therefore:

$$C = \frac{(I_1 - I_2)}{I_1} = \frac{I_0 \exp(-\mu_1 t_1) - I_0 \exp[-\mu_1 (t_1 - t_2)]\exp(-\mu_2 t_2)}{I_0 \exp(-\mu_1 t_1)} =$$

$$= \frac{I_0 \exp(-\mu_1 t_1) - I_0 \exp(-\mu_1 t_1)\exp(\mu_1 t_2)\exp(-\mu_2 t_2)}{I_0 \exp(-\mu_1 t_1)} =$$

$$= \frac{I_0 \exp(-\mu_1 t_1) - I_0 \exp(-\mu_1 t_1)\exp[(\mu_1 - \mu_2) t_2]}{I_0 \exp(-\mu_1 t_1)} = 1 - \exp[(\mu_1 - \mu_2) t_2]$$

C does not depend on I, only on μ's and t's - > SUBJECT characteristics (sometimes called "subject" contrast).

L1-34

$$C = 1 - \exp[(\mu_1 - \mu_2) t_2]$$

What happened to t_1?

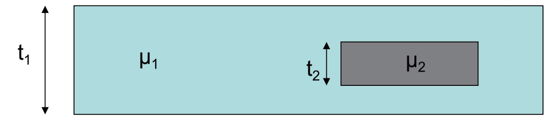

look at it this way:

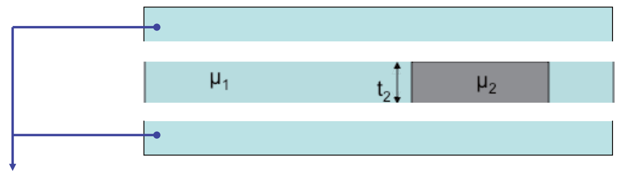

These are two uniform absorbers -> they only change I!

L1-35

C increases with detail thickness (quite obviously) and with the difference between the attenuation coefficients of detail & background:

HOW DOES THIS BEHAVE WITH X-RAY ENERGY?

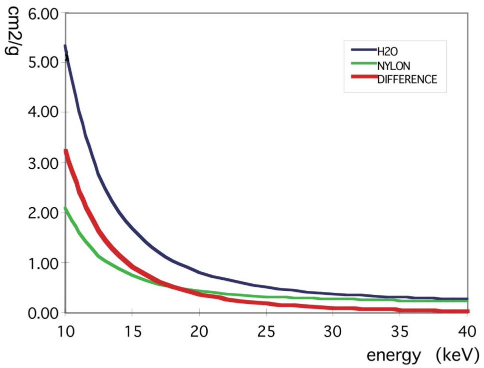

Away from absorption edges, attenuation coefficients decrease with increasing x-ray energy. Therefore, generally speaking the contrast DECREASES with increasing energy.

L1-36

So the Contrast tells you how much a given detail, in percentage, stands out of the surrounding background

It depends on the detail (t, μ) and on the x-ray energy (through μ), but

NOT ON THE AMOUNT OF X-RAYS you've used

-> IT DOES NOT TELL YOU how well you'll see it!

e.g. if you shoot 2 x-rays in total, you'll hardly see anything even if your detail has C=90%!

L1-37

Here's where the SNR (or the CNR) becomes important:

(e.g. Rose criterion: a detail is visible if SNR≥5)

THE NOISE IN YOUR IMAGE determines how likely you are to see a detail with a given contrast;

NOISE is normally driven by the amount of x-rays you use (plus quality of your detector and other practical factors)

SNR: two "versions" found in the literature:

1) (most common) signal VS background noise;
2) Signal VS uncertainty on the signal itself.

L1-38

For simplicity's sake -> PHOTON COUNTING detector;

-> Instead of I, we can use N (i.e. $I_1=N_1$, etc);

-> Poisson statistics: Var[N]=N i.e. $\sigma_N = \sqrt{N}$

SO for example, using definition 1):

(signal vs. background noise)

$$SNR = \frac{N_1 - N_2}{\sigma(N_1)} = \frac{N_1 - N_2}{\sqrt{N_1}}$$

L1-39

NOTE THAT: $$SNR = \frac{N_1 - N_2}{\sqrt{N_1}} = \sqrt{N_1}\frac{N_1 - N_2}{N_1} = \sqrt{N_1}C$$

SO HERE'S HOW WELL YOU SEE SOMETHING: it depends on ***C*** (-> object, x-ray energy), and it gets better with the **SQUARE ROOT** of the number of x-rays

$$SNR = \sqrt{N_1}\{1-\exp[(\mu_1-\mu_2)t_2]\} = \sqrt{N_0\exp(-\mu_1 t_1)}\{1-\exp[(\mu_1-\mu_2)t_2]\}$$

Where N_0 is the number of photons (per unit area) hitting the sample.

NOTE THAT t_1 now plays a role: the thicker the sample, the more the beam is attenuated

Therefore less photons reach the detector -> higher noise -> lower SNR

L1-40

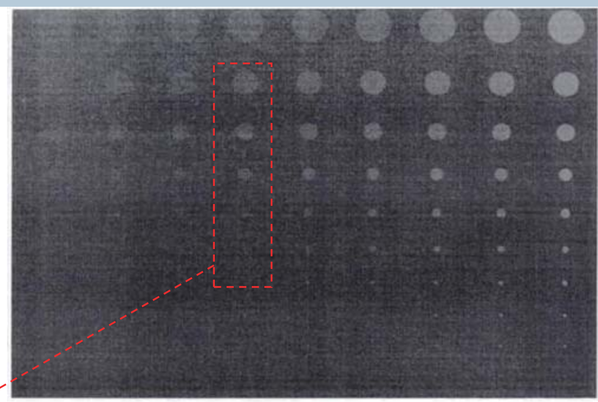

THESE DETAILS have the same *C* and the same number of photons was clearly used. So if SNR = sqrt(*N*)**C*, how comes I do not see them anymore below a certain size?

THE FORMULAS I'VE GIVEN YOU ARE SIMPLIFIED AND ARE VALID FOR **1 PIXEL ONLY**:
the extension is straightforward and it involves multiplying x (# pixels involved)$^{1/2}$

L1-41

i.e. if a detail covers m pixels, then

$$SNR = \sqrt{m}\sqrt{N_1}C$$

The explanation is extremely intuitive: imagine **binning** your pixels (e.g. 2x2 in the simple case the detail covers 4 pixels)

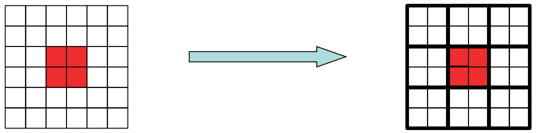

Now the detail covers 1 pixel, which receives 4 times as many counts i.e $4N_1$ counts in total:

$$SNR = \sqrt{4N_1}C = \sqrt{4}\sqrt{N_1}C$$

L1-42

Ways to improve contrast

A. Remove scatter

L1-43

Effect of scatter on contrast:

- WITHOUT scatter:

$$C = \frac{I_1 - I_2}{I_1}$$

- WITH scatter:

$$C' = \frac{(I_1 + S) - (I_2 + S)}{I_1 + S} = \frac{I_1 - I_2}{I_1 + S} < C$$

L1-44

Ways to improve contrast

A. Remove scatter
B. Increase inherent contrast
   - **Contrast agent**
C. Reduce kV
   - **Photoelectric effect α Z^3 E^{-3}**
D. Remove effects of overlying tissues
E. **USE PHASE CONTRAST!**

L1-45

Phase Contrast Imaging vs. Conventional Radiology

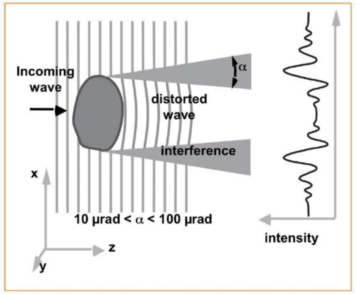

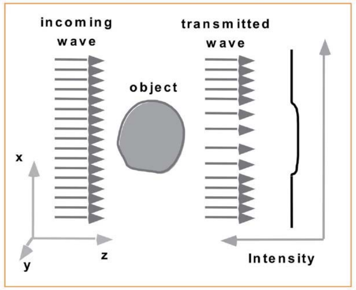

Refractive index: $n = 1 - \delta + i\beta$; $\delta >> \beta$ ->
phase contrast (**$\Delta I/I_0 \sim 4\pi\delta\Delta z/\lambda$**) >> absorption contrast (**$\Delta I/I_0 \sim 4\pi\beta\Delta z/\lambda$**)

Two possible approaches:

- detect interference patterns
- detect angular deviations

L1-46

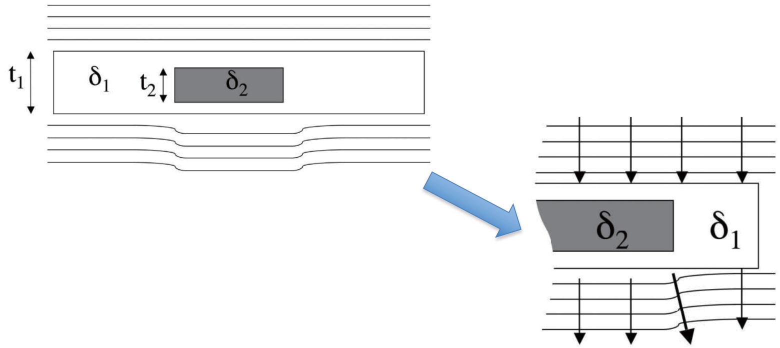

L1-47

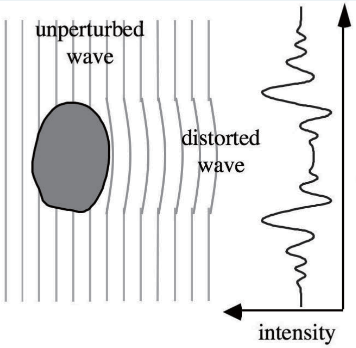

NB you can also model FSP on the same basis; if coherence is relaxed, you will get approximately the same results.

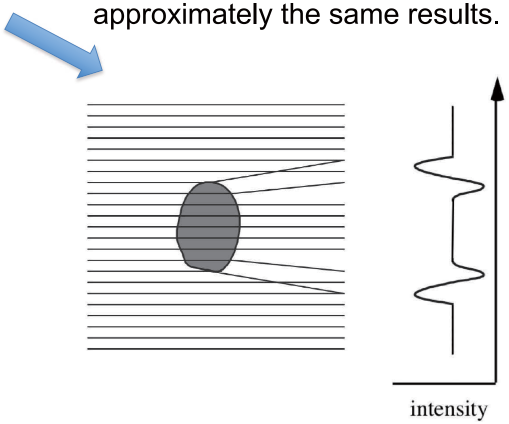

L1-48

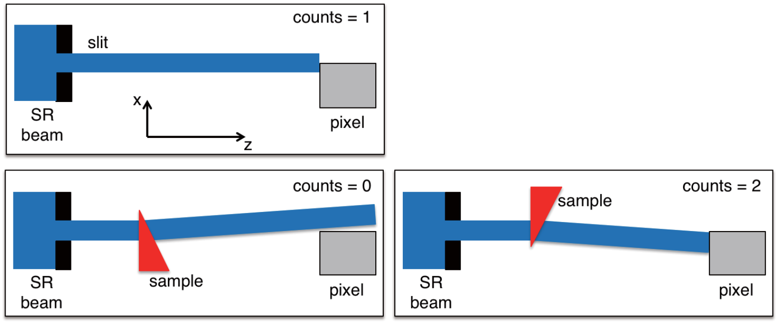

A simple way to exploit refraction is to shape the x-ray beam and aim it at a “sensitivity edge”

L1-49

Which can be extended to full FoV imaging using large area masks
(see e.g. invited talk by Massimi and talks by Endrizzi later in the conference)

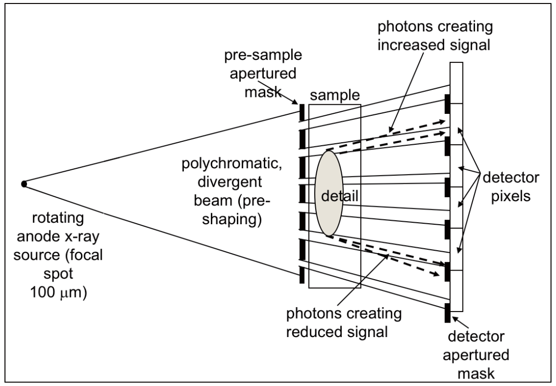

There are of course many other ways to exploit phase effects, even more based on interferometric effects – **Prof Franz Pfeiffer** will tell you all about that in the lecture following this one.

L1-50

Before I leave you to Franz, a few historic milestones:

Film-Screen

- Use fluorescent screen
- \+ μ higher
- \+ Thicker than emulsion
- \+ Optical photons 1-3eV → gain
- \- Reduced spatial resolution

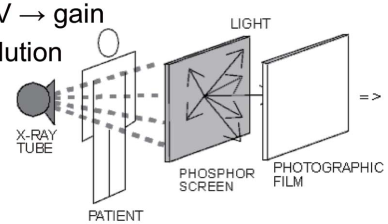

The stopping power of the plain film is only 1-3% of the one provided by a modern intensifier screen (Sabel and Aichinger, 1996).

L1-51

a few historic milestones

"A new system of computed radiography that is based on new concepts and the latest computer technologies has been developed. This system eliminates the drawbacks of conventional screen-film radiography. The basic principle of the system is the conversion of the x-ray energy pattern into digital signals utilizing scanning laser stimulated luminescence (SLSL)" (Sonoda *et al*, 1983)

Computed Radiography: Photostimulable Phosphor (PSP) plate

L1-52

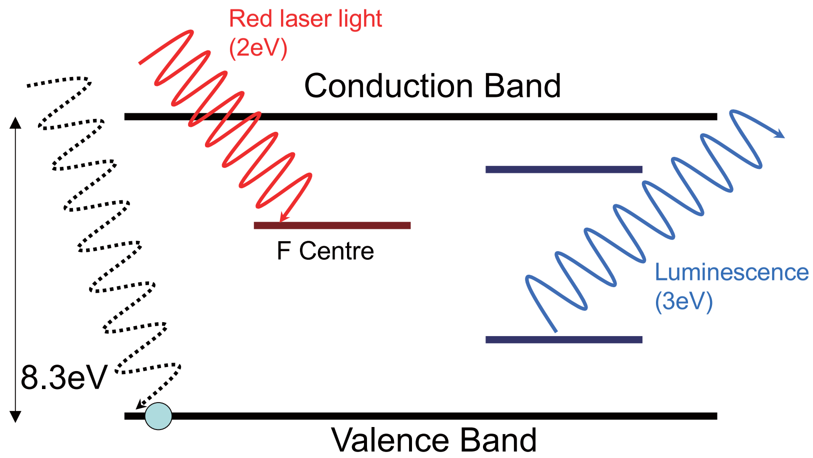

L1-53

a few historic milestones

Flat Panel Detectors

- Direct conversion
  - Amorphous selenium
- Indirect conversion
  - Scintillator
  - Amorphous silicon

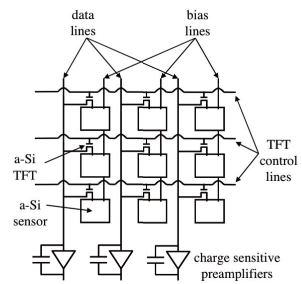

L1-54

a few historic milestones

CMOS sensors

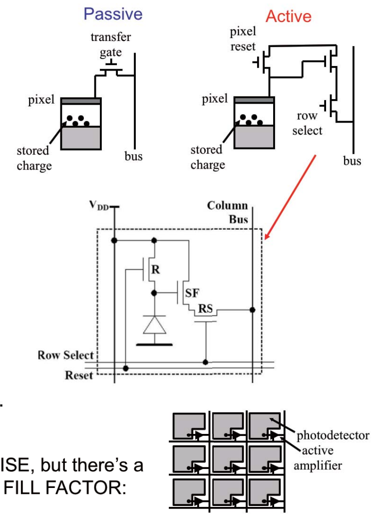

- Reset transistor 'R' clears the pixel of integrated charge
- Source Follower transistor 'SF' amplifies/buffers the signal (ACTIVE pixel)
- Row Select transistor 'RS' selects the row for readout.

ACTIVE-> reduces NOISE, but there's a price to pay in terms of FILL FACTOR:

L1-55

a few historic milestones

Single-photon counting readout scheme

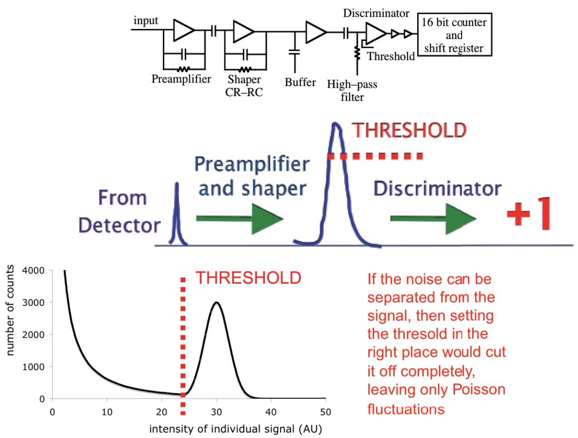

If the noise can be separated from the signal, then setting the thresold in the right place would cut it off completely, leaving only Poisson fluctuations

L1-56

a few historic milestones

Computed Tomography

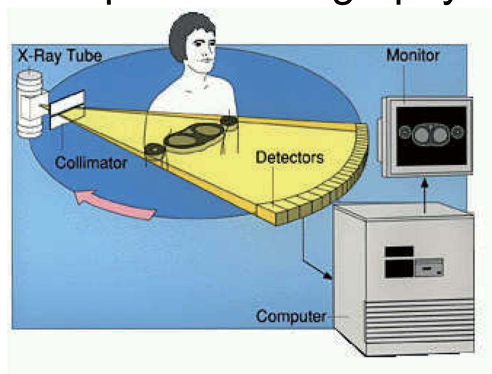

L1-57

a few historic milestones

Computed Tomography

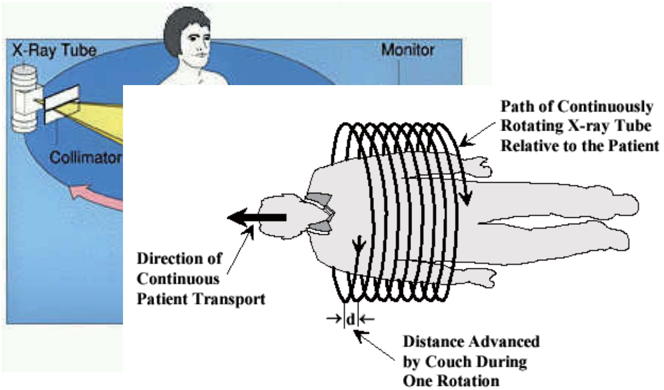

… all details in Prof Marco Stampanoni's lecture later today

L1-58

Thanks for listening

QUESTIONS??

a.olivo@ucl.ac.uk
https://www.ucl.ac.uk/medical-physics-biomedical-engineering/research/research-groups/advanced-x-ray-imaging-group-axim

Tutorial 2

(14:15 – 14:45)

Historical view of neutron radiography

Dmitry A. Pushin

University of Waterloo,

Canada

L2-1

HISTORICAL VIEW OF NEUTRON RADIOGRAPHY

Dmitry Pushin, IQC and University of Waterloo/NIST

L2-2

Acknowledgements – NIST Neutron Imaging Team

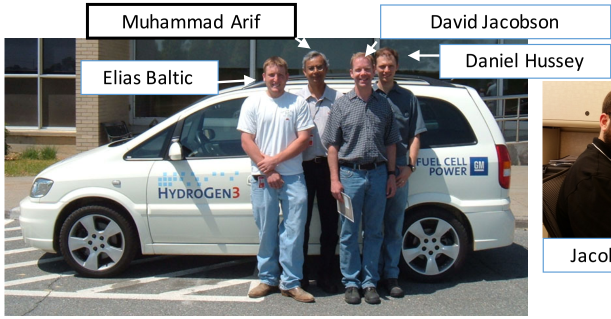

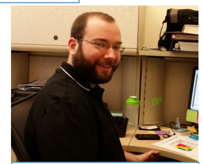

Jacob LaManna

L2-3

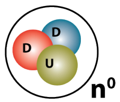

The Neutron

1935, nobelprize.org

- Discovered 1932 by James Chadwick
- A fundamental building block of atomic nucleus
- Free neutron lifetime ~ 15 min (880.2±1.0 s)
- Neutron mass = 1.001378419 proton mass
- Produced from fission (nuclear reactor) or scattering of high energy proton beams (spallation source)
- Electrically neutral but has magnetic moment
- Thermal neutron unique penetrating abilities

L2-4

Neutron production

Neutrons are Produced by Fission of ^{235}U

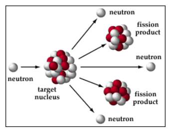

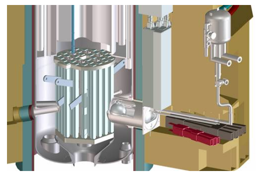

NIST 20 MW Reactor

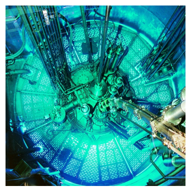

ILL 60 MW Reactor

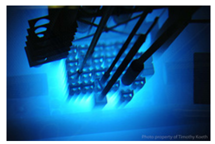

250 kW Training Reactor (MUTR)

L2-5

Neutron Spectrum

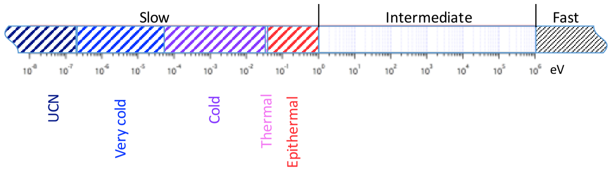

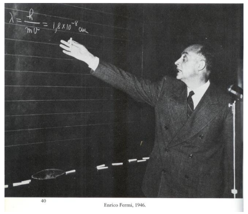

A thermal neutron has:

- Energy of 20 meV
- Wavelength of 2 Å
- Speed of 2000 m/s

L2-6

Imaging with Neutrons

The fine details of the water concentration in these lilies are clear to neutrons even in a lead cask

Ordinary photography

Hussey, NIST

Neutron radiography

L2-7

Daniel Hussey, NIST

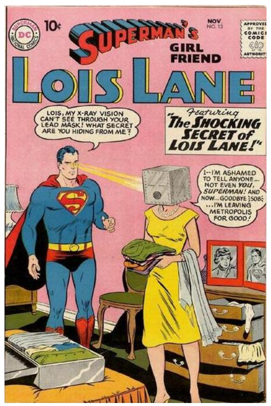

DC Comics

L2-8

Great things about neutrons

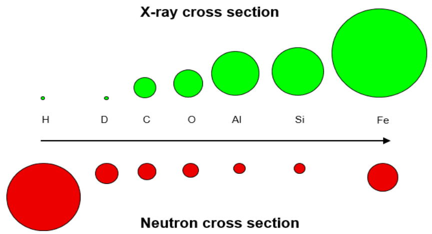

- Neutrons penetrate many materials well yet remain extremely sensitive to liquid water, hydrocarbons and lithium
- This allows one to study a wide range of transport related issues like:
  - Liquid water in fuel cells
  - Lithium in batteries
  - Multiphase flow in geological rock cores

X-ray image
- Metal parts: opaque
- Plastic parts: transparent

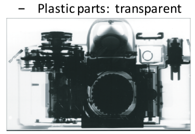

PSI

Neutron image
- Metal parts: transparent
- Plastic parts: opaque

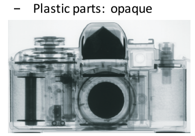

PSI

L2-9

Brief Historical Perspective

THE FIRST DEMONSTRATION OF NEUTRON RADIOGRAPHY WAS MADE BY HARTMUT KALLMANN AND E. KUHN IN THE LATE 1930S

THE FIRST NEUTRON RADIOGRAPHS OF REASONABLE QUALITY WERE MADE BY J. THEWLIS (UK) IN 1955

AROUND 1960, HAROLD BERGER (US) AND JOHN BARTON (UK) BEGAN EVALUATING NEUTRONS FOR INVESTIGATING IRRADIATED REACTOR FUEL

- BERGER WORKED AT ARGONNE NATIONAL LAB AND LATER MOVED TO NIST

1979 NEUTRON PHASE TOPOGRAPHY WITH NEUTRON INTERFEROMETER BY U. BONSE

1981 FIRST WORLD CONFERENCE ON NEUTRON RADIOGRAPHY SAN DIEGO

1990's

- RADIOGRAPHY HAS DISAPPEARED AT NIST
- CCD FIRST USED FOR NEUTRON RADIOGRAPHY
- PERSONAL COMPUTER PROCESSING POWER SUFFICIENT TO PROCESS IMAGES EFFICIENTLY

2000 FRESNEL PROPAGATION PHASE IMAGING BY ALLMAN ET. AL.

2006 TALBOT-LAUE NEUTRON GRATING INTERFEROMETER BY F. PFEIFFER ET. AL.

2007 RECIPROCAL SPACE NEUTRON IMAGING BY D. PUSHIN ET. AL.

2008 NEUTRON DARK-FIELD TOMOGRAPHY BY M. STROBL ET. AL.

2017 PHASE-GRATING MOIRÉ NEUTRON INTERFEROMETER BY D. PUSHIN ET. AL.

2019 XNPIG2019 SENDAI, JAPAN

L2-10

Neutron Imaging Geometry

- Pinhole optics is the basis for images
- Aperture at reactor face, form image of core at detector
- Optimal resolution when object contacts detector
- Geometric blur is given approximately by:

  $\lambda_g \approx z\, d\, /\, L$

- High resolution of finite objects requires large L/d
  - small aperture (d) fewer neutrons
  - Large L low intensity due to $1/r^2$ loss
- Intrinsic detector resolution is also critical for higher resolution

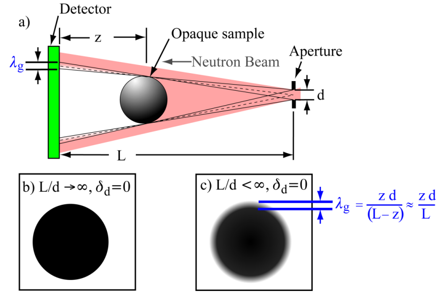

L2-11

Quantification

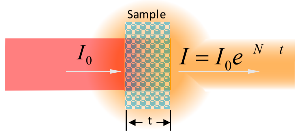

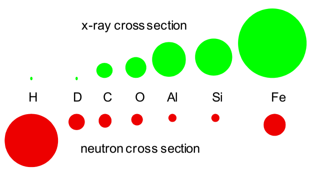

- N – numerical density of sample atoms per cm^3
- I_0 - incident neutrons per second per cm^2
- σ - neutron cross section in ~ 10^{-24} cm^2
- t - sample thickness

$$T(i,j) = e^{-N(i,j)\sigma t}$$

or

$$m(i,j) = m_N N(i,j)t = -m_N \frac{\ln[T(i,j)]}{\sigma}$$

$m(i,j)$ = area mass in grams

m_N = molar mass

L2-12

Cross Sections

- Values below 10 have low contrast
- Between 10 -100 contrast is good for high resolution imaging
- Values above 100 are difficult to penetrate
- Greater than 300 they make excellent beam stops

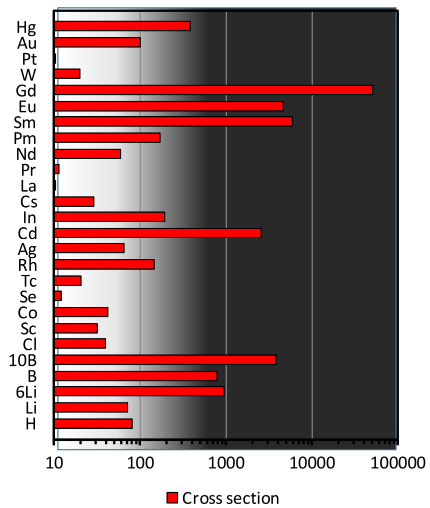

L2-13

Contrast Agents

Used to turn contrast on or off

Deuterium and Hydrogen

- Replacement of hydrogen with deuterium is frequently used to turn off the hydrogen signal
- Thick hydrogen samples can be imaged better in some cases by replacing the hydrogen with deuterium

Gadolinium has an enormous cross section

- $Gd(NO_3)_3$ salts can be used to image cracks

3-D Hydrogen (Deuterium) Distribution across a storage bed

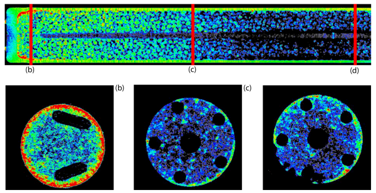

L2-14

Water Sensitivity

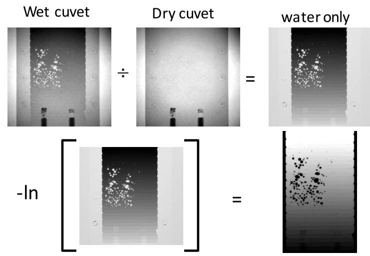

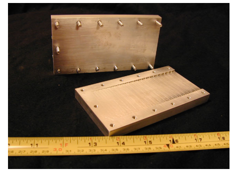

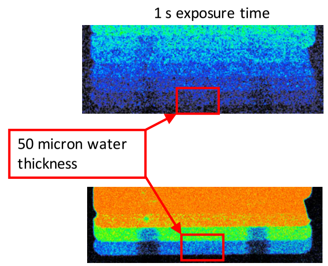

- Thin stepped wedge with steps machined with 50 micron.
- CCD camera exposure of 1 s yields a sensitivity of 0.005 g cm^{-2} s^{-1}
- After 100 s a factor of 10 improvement gives 0.0005 g cm^{-2} s^{-1}

L2-15

NEUTRON IMAGING DETECTORS

L2-16

Nuclear Reactions for Neutron Imaging

- n + ^{6}Li $\rightarrow$ ^{4}He (2.04 MeV) + ^{3}H (2.75 MeV)
- n + ^{10}B $\rightarrow$ ^{7}Li* + ^{4}He$\rightarrow$^{7}Li (0.84 MeV) + ^{4}He (1.47 MeV) + 0.48 MeV γ (93%)
  $\rightarrow$ ^{7}Li + ^{4}He + 2.78 MeV (7%)
- n + ^{155}Gd $\rightarrow$ Gd* $\rightarrow$ γ-ray spectrum $\rightarrow$ conversion electron spectrum
- n + ^{157}Gd $\rightarrow$ Gd* $\rightarrow$ γ-ray spectrum $\rightarrow$ conversion electron spectrum

- ^{3}H range in ZnS > 30 mm (SRIM calculation) but as much as 120

L2-17

Neutron Scintillators

ZnS:^{6}LiF

- n + ^{6}Li → ^{4}He (2.04 MeV) + ^{3}H (2.75 MeV)
- *Spatial Resolution from 70* μm *to 300* μm, thermal stopping power 20%
- Highest light yield 10^5 photons/neutron

GadOx (x-rays and neutrons)

- n + ^{155}Gd → Gd* → γ-ray spectrum → conversion electron spectrum
- n + ^{157}Gd → Gd* → γ-ray spectrum → conversion electron spectrum
- *Resolution ~20-60* μm, thermal stopping power up to 80%
- Low light yield (10^3 photons/neutron) since conversion electrons are < 100 keV

Other Gd type scintillators (GGG) resolution of 7 μm reported

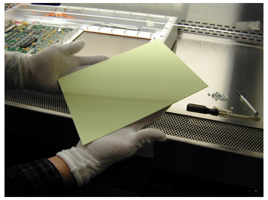

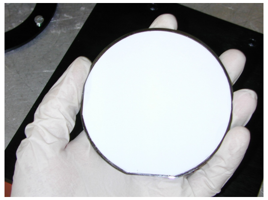

L2-18

Microchannel Plate Detectors

Microchannel plate detectors

- 1984, R. Schrack, NIMA
- 1990 Boron Doped MCPs (Fraser, et al, NIMA, 377,p119)
- 1996 ND&M (Dietze, et al, NIMA,377,p320)
  - Counting detector SNR
  - Incorporates centroiding to get 50 μm resolution
  - Count rate very limited
  - Extremely innovative detector developed in Munich!
  - Led to rebirth of Neutron Radiography at NIST!
- 2006 Boron/Gd Doped MCPs with Cross delay line anode detectors
- 2009 Boron/Gd Doped MCPs with Cross strip detectors (1-2 Mhz max count rates) (Tremsin, et al, NIMA, 604, p140 (2009)

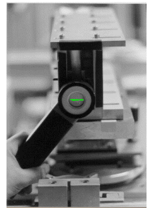

L2-19

Borated MCP Neutron Detection Mechanism

n+^{10}B → ^{7}Li + ^{4}He + Q (2.79 MeV)

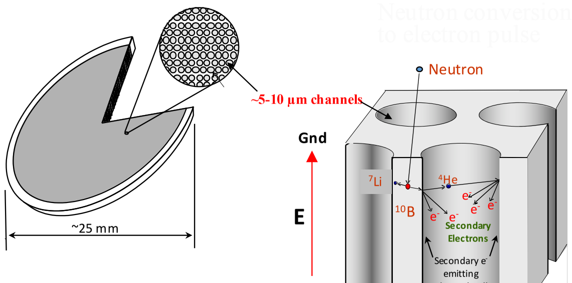

Typical MCP structure

L2-20

Advanced High Resolution Neutron Imaging Detector

- Faster – handles 10x the previous rates
- Better – ~10 μm improves resolution by factor of 2
- More – next generation will have 10 cm by 10 cm field of view

40mm Cross Strip (XS) neutron detector

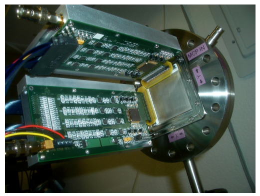

40mm XS anode neutron detector showing the back of the detector with the amplifier boards for X and Y axis event position encoding.

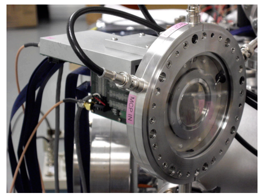

40mm XS anode neutron detector showing the front of the detector on the 6" conflat flange, and the HV connections.

•Berkley Space Sciences Laboratory
•Sensor Sciences, LLC.
•NOVA Scientific

L2-21

Detectors: Light Imagers

Amorphous Silicon
- Estermann, et al, NIMA, 542, p253 (2005)
- Fixed pixel pitch of 127 µm, 25x20cm FOV
- Up to 30Hz frame rate (2x2 binning)
- Amorphous silicon sensor is mostly rad hard
- Non-rad hard readout electronics are folded out of the beam
- LiF:

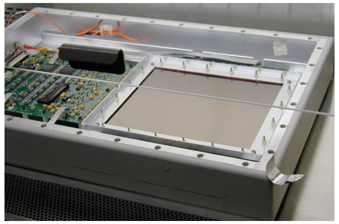

L2-22

Neutron CCD/sCMOS Imaging Device

First method used by many to capture digital radiographs

Most versatile
- Can use standard Nikon lenses
- Any light emitting converter
- MCP intensified and gated cameras for dynamic imaging

Images are high quality except for those distorted by the lens

Light collection efficiency is low due to distance and lens

Current generations low noise allow single photon counting

Readout Time/Frame Rate
- CCD 3 s – 5 s or more
- EMCCD 10 Hz
- sCMOS 100 Hz and more

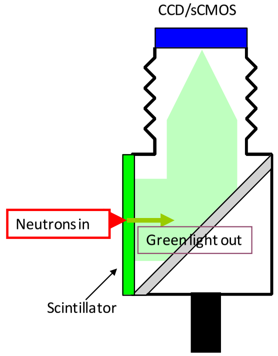

L2-23

NIST Camera Box

Lens/Camera is soft coupled by a flexible bellows for light tightness

Lens adjusted by hand or mechanical control

Fine focus by moving camera on a translation stage

Lens coupled enables flexibility

CCD has slow readout that limits time resolution

Andor Neo sCMOS,
- 2560 x 2160,
- 6.5 µm pixels,
- 30 fps, burst mode 100 fps with on board 4 Gb memory
  - 1 e⁻ read noise
- Combinations lenses and mirror boxes allow FOVs:
  - 1.66 cm x 1.40 cm
  - To 26 cm x 26 cm (beam size)

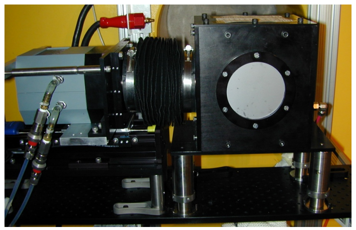

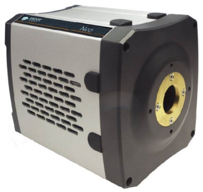

L2-24

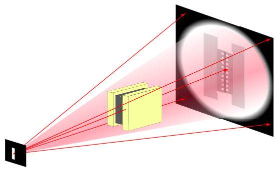

Fuel Cell Water Profile

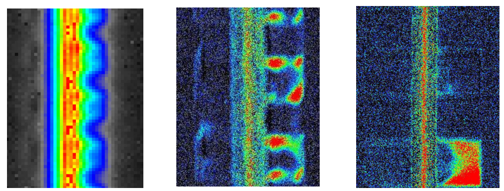

Amorphous silicon	CCD/sCMOS	MCP
Spatial Resolution: 250 µm	Spatial Resolution: 20 µm	Spatial Resolution : 13 µm
Field of View: 25 cm x 20 cm	Field of View: 1 cm x 1 cm	Field of View: 3.5 cm x 3.5 cm
Frame Rate: 30 frame/s	Frame Rate: 100 frame/s	Frame Rate: 10 s – 20 min

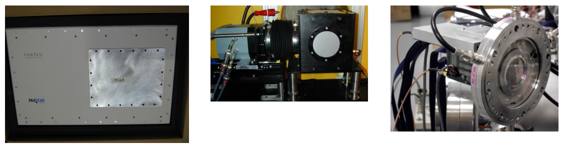

L2-25

Another Potential Path to High Resolution: Light Centroiding

- Light from scintillator blooms out
- Size of the light bloom results in blurring in the image
- Spatial resolution is 25 μm due to blurring
- Image intensifier improves signal
- New sCMOS cameras allow very high frame rates 100 fps
- individual neutron strikes can be captured
- Centroiding the light clouds could get to sub 5 μm resolution
- Modern field-programmable gate array (FPGA) could allow efficient centroiding

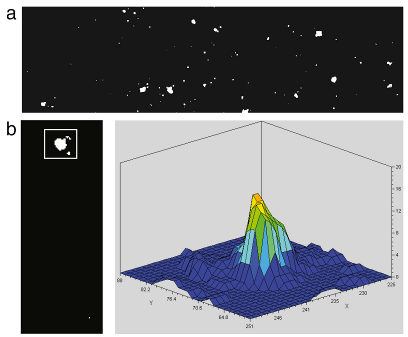

D. S. Hussey, J. M. LaManna, E. Baltic, D. L. Jacobson, Nucl. Inst. and Meth. A, **866** (2017) 9–12

L2-26

Spatial Resolution

- Resolution described by point spread function (PSF) which introduces cross-talk between all the pixels
- The cross-talk, besides blurring out detail, also introduces an effective background which changes the observed attenuation
- This is seen in the "Measured Image" where black areas are now grey
- Deconvolution algorithms can be used to correct this systematic effect

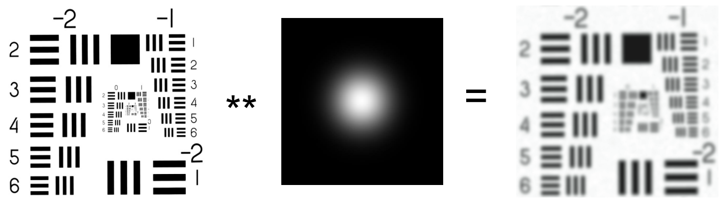

True, Sharp Image — Blurring function — Measured Image

L2-27

Spatial Resolution

- 1951 USAF Target
- Limiting resolution
  - 10 % contrast (MTF 10 %)
  - Here 28.5 line pairs per millimeter for line pair widths of 17.54 mm.
  - Spatial Resolution is ~18 mm

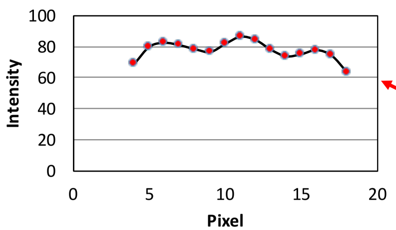

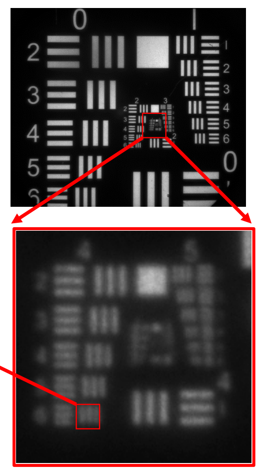

L2-28

Setting up the Image for Radiography or Tomography

- Lots of room for sample setup
- 6 meters from aperture to sample position.
- Aluminum flight tube evacuated.
- Short sections can be made into a shorter tube for closer positions.
- Closest position is 1 meter.

L2-29

Why combine neutrons and X-rays? Awesome complementarity!

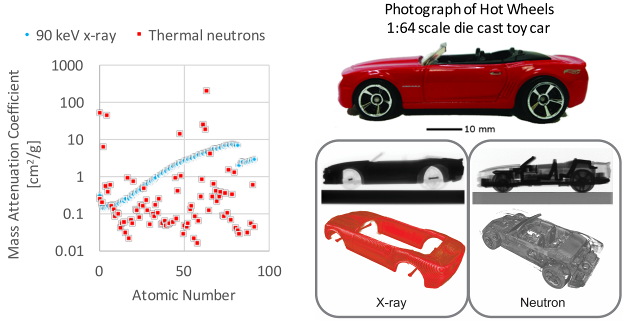

L2-30

Why combine neutrons and X-rays? Awesome complementarity!

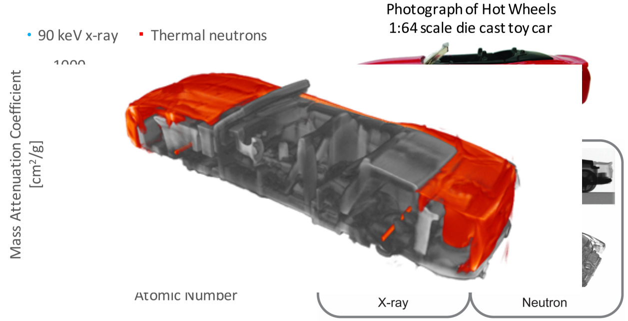

L2-31

The NIST **Simultaneous** Neutron and X-ray Tomography System

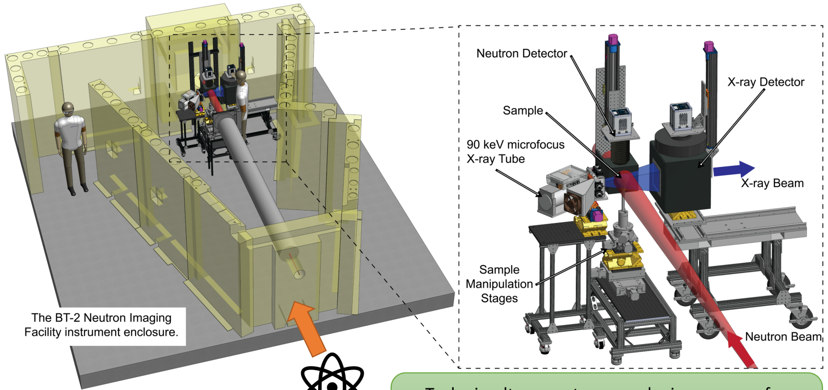

Truly simultaneous tomography is necessary for samples slowly evolving with time or under stochastic processes.

J.M. LaManna et al., "Neutron and X-ray Tomography (NeXT) System for Simultaneous, Dual Modality Tomography", Rev. Sci. Inst., 88, 113702 (2017).

L2-32

Identification of Organic and Mineral Distributions in Shale

- Aim: Understand distribution of shale constituents to improve understanding of hydraulic fracturing
- Initial well characterized open literature samples

Neutrons -> **organic content**

X-rays -> **mineral content**

Hydrocarbons, dense minerals, and fractures all identified for improved computational modeling.

1 inch diameter cores, 30 micrometer resolution

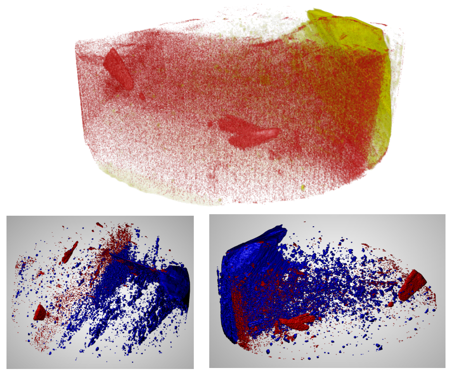

W.S. Chiang et al, "Simultaneous Neutron and X-Ray Imaging of 3D Structure of Organic Matter and Fracture in Shales", PETROPHYSICS, VOL. 59, NO. 2 (APRIL 2018), PAGES 153–161.

L2-33

Extended Analysis to Cores from Production Wells

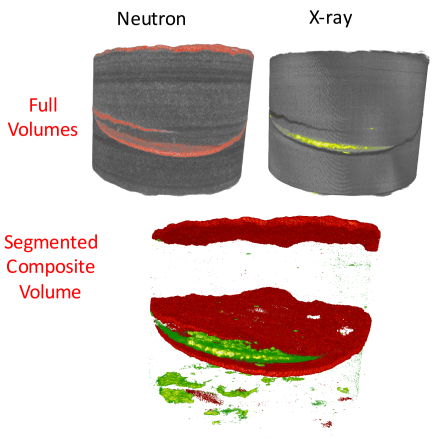

- Typical techniques for shale analysis are at pore scale, NeXT provides details at the core scale
- Organic rich kerogen layers not seen before
- Cores will be scanned while in a pressure vessel to facilitate gas loading with methane

Neutrons -> **organic content**

X-rays -> **mineral content**

Generated volumes will provide geometry and compositional information for computational flow models in large formations.

W.S. Chiang et al, "Simultaneous Neutron and X-Ray Imaging of 3D Structure of Organic Matter and Fracture in Shales", PETROPHYSICS, VOL. 59, NO. 2 (APRIL 2018), PAGES 153–161.

L2-34

MORE EXAMPLES

L2-35

NEUTRON PHASE CONTRAST RADIOGRAPHY

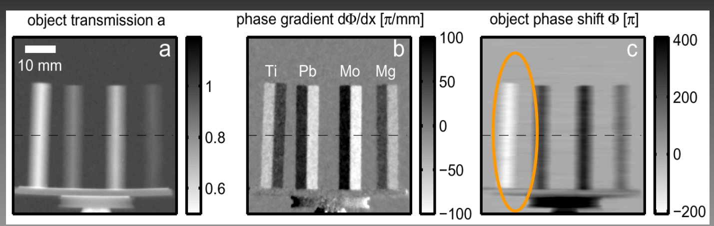

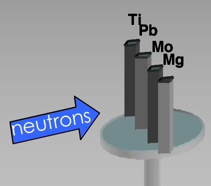

total exposure time ~ 100 sec,
spatial resolution ~ 250 micron

F. Pfeiffer, C. Grünzweig, O. Bunk, G.Frei, E. Lehmann and C. David, ***PRL 96***, 215505 (2006).

L2-36

Grating Phase Imaging

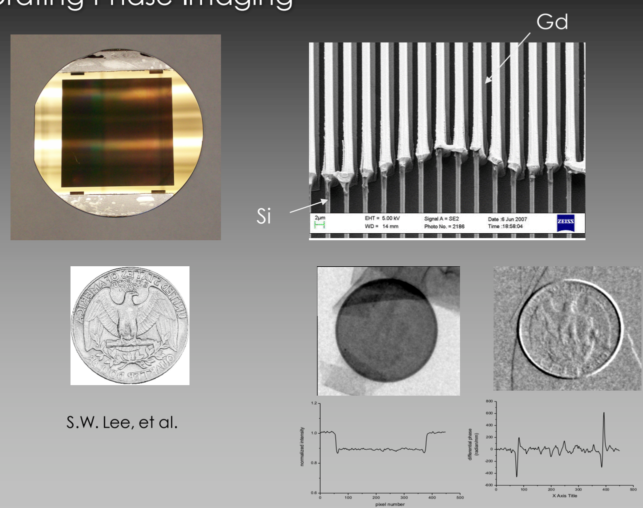

S.W. Lee, et al.

L2-37

IMAGING WITH POLARIZED NEUTRONS

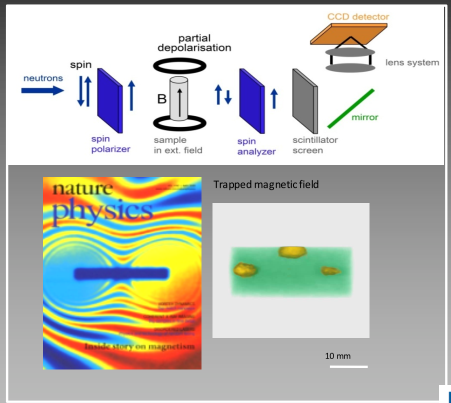

N. Kardjilov et al, Nature Physics 4, 399, 2008

L2-38

Phase transitions in magnetic systems

PdNi crystal (3.24% Ni) at different temperatures imaged by polarized neutrons

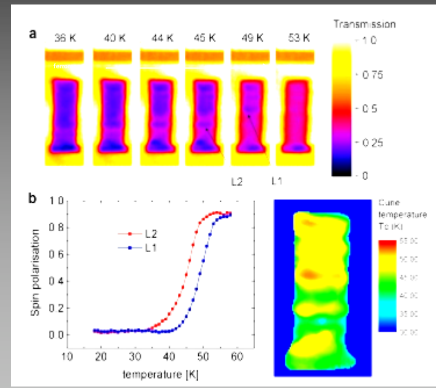

Technische Universität München

L2-39

ENERGY SELECTIVE IMAGING

- Bragg Edge of Al is at 4.7 Å
- Wavelength dependent attenuation was measured from 2.7 Å to 6.0 Å
- Low attenuation of Al leads to long exposure times of 45 min to give sufficient contrast
- Texture: preferred orientation of crystallites wrt. the incoming beam leads to dark areas at certain wavelengths
- Each wavelength corresponds to one reflection angle

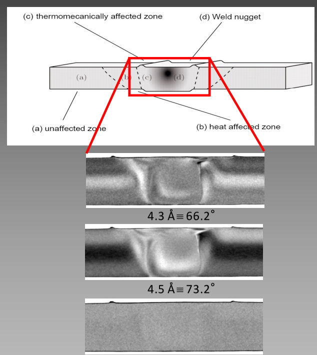

Forschungsneutronenquelle Heinz Maier-Leibnitz (FRM II)

L2-40

Imaging of Laser Weld

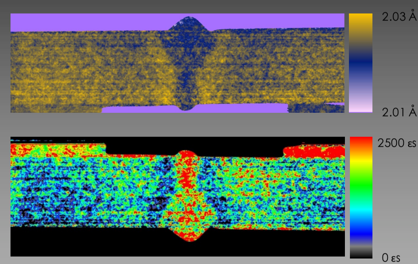

"Bragg Edge" is increase in transmission when $\lambda > 2d_{hkl}$
Acquire many images over narrow λ band

Compressive strain map constructed from Bragg-edge image (chemical and mechanical) Here, image spatial resolution is 50 μm, sample is 1 cm x 2 cm x 6 cm

L2-41

Studying Root Growth of Lentils

- Absorbent additives can improve water retention of soil, especially in drought
- Neutrons penetrate soil and measure the saturation
- Treated sample has higher water retention
- Follow-on experiments in root growth

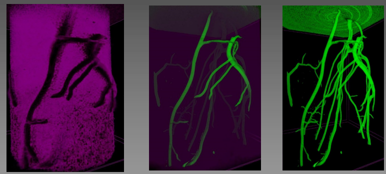

Brown = Sand, Blue = Water

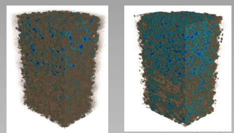

R. Murphy, Rhodia/Solvay

L2-42

LITHIUM BATTERIES

CHARGING SEQUENCE

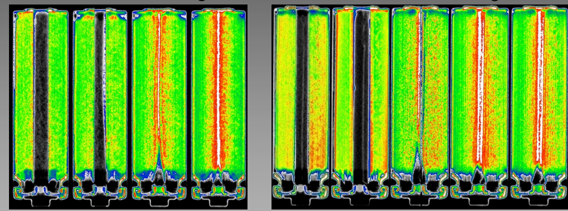

L2-43

TOMOGRAPHY

- If object is 1000 pixels across we need 1570 images to achieve the pixel resolution at the edge
- Usually we set the number of images to be 1000
- Each image requires 1 s – 120 s of exposure time
  - Acquisition time = 16.7 min at 1 s
  - Acquisition time = 34 hours at 120 s
- Much faster acquisition can be achieved if you are willing to sacrifice resolution

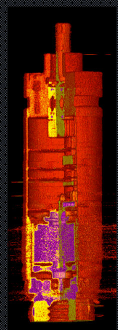

L2-44

Neutron Microscope

Ellipsoid – Hyperboloid for Image Magnification

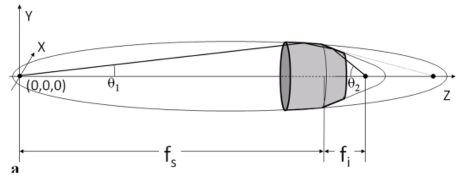

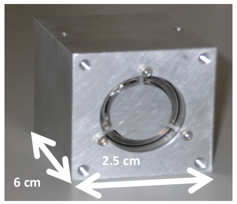

Liu et al., Appl. Phys. Lett. 102, 183508 (2013)

Prototype lens

4 nested Ni mirrors
- nesting increases flux collection

Observed Performance:
- 75 µm spatial resolution
- 1 cm FOV & 4x magnification
- 5 mm depth of focus
- 5x gain in intensity to pinhole

L2-45

Conclusion

Radiography and tomography with neutrons

- Good for two phase flow when x-rays can't penetrate metal or rock
- Unique contrast for certain elements especially hydrogen
- Isotopic contrast as well allows contrast to be varied

Multimodal imaging with X-rays and neutrons

- Overcomes registration of x-ray and neutron tomography
- Produces in situ complete picture for two phase flow problems
- Allows 2-d histogram of x-ray/Neutron attenuation coefficient to better segment phases

Future: Energy selective stress/strain imaging with high spatial resolution

- Impact for understanding stress/strain in additive manufacturing methods

Future: Grating methods

- Dark field pair correlation function measurements have potential to connect the nanoscale to macroscale imaging
- Opens new possibilities in studying porous media

Future: Neutron microscopy

- Could achieve 1 mm resolution with (20 min exposures – quick for neutrons and 100x faster than currently achievable)

L2-46

Thank you!

Tutorial 3

(15:05 – 15:50)

Introduction to phase imaging principles & potential applications

Franz Pfeiffer

Technische Universität München,

Gernmany

L3-1

Introduction to Phase Imaging Principles & Potential Applications

Prof. Dr. rer. nat. Franz Pfeiffer

Munich School of Bioengineering
Faculty of Physics & Medicine
Technical University Munich

Sendai, October 2019

L3-2

Basic Physics

Wave propagation, phase shift, complex index of refraction

L3-3

X-rays as Waves & Phase shift

in vacuum

$$\Psi(\vec{r},t) = \Psi_0\,\mathrm{e}^{i(\vec{k}\cdot\vec{r}-\omega t)}$$

$$\vec{k} = (0,0,k=\tfrac{2\pi}{\lambda})$$

$$\Psi_v(\vec{r},t) = \Psi_0\,\mathrm{e}^{i(\vec{k}\vec{r}-\omega t)} = \Psi_0\,\mathrm{e}^{i(kz-\omega t)}$$

L3-4

X-rays as Waves & Phase shift

in a medium

$$\Psi(\vec{r},t) = \Psi_0\,\mathrm{e}^{i(\vec{k}\cdot\vec{r}-\omega t)}$$

$$n = \underbrace{1-\delta}_{\text{[elastic]}} + \underbrace{i\beta}_{\text{[inelastic]}}$$

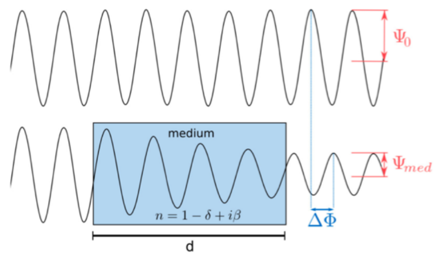

$$\Psi_m(z,t) = \Psi_0\,\mathrm{e}^{i(nkz-\omega t)} = \Psi_0\,\mathrm{e}^{-i\omega t}\,\mathrm{e}^{(1-\delta)ikz}\,\mathrm{e}^{-\beta kz}$$

$$= \Psi_v(z,t)\cdot \underbrace{\mathrm{e}^{-i\delta kz}}_{\text{[phase-shift]}} \cdot \underbrace{\mathrm{e}^{-\beta kz}}_{\text{[attenuation]}}$$

L3-5

X-rays as Waves & Phase shift

transmission & phase shift

$$T(d) = \frac{I_m(d)}{I_v(0)} = \frac{|\Psi_m(d,t)|^2}{|\Psi_v(0,t)|^2} = \mathrm{e}^{-2k\beta d}$$
$$= \mathrm{e}^{-\mu d}$$

$$\Delta\Phi = \delta k d$$

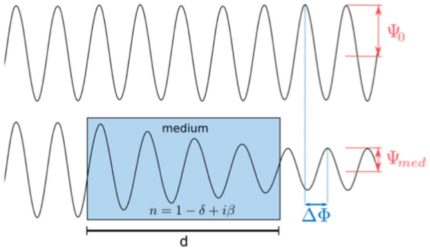

$$T(x,y) = \mathrm{e}^{-2k \int \beta(x,y,z)\, dz}$$
$$\Delta\Phi(x,y) = k \int \delta(x,y,z)\, dz$$

$$\delta = \frac{r_0}{2\pi}\lambda^2 \rho_e = \frac{2\pi r_0 \hbar^2 c^2}{E^2}\rho_e$$

L3-6

X-rays as Waves & Phase shift

cross sections & refractive index values for water

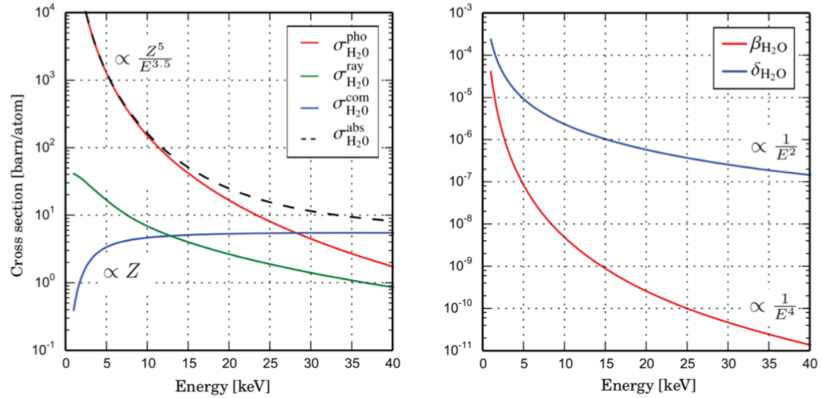

L3-7

The 1960s

Crystal Interferometer Phase Contrast

L3-8

Crystal Interferometry

with perfect single-crystal silicon interferometers

Ulrich Bonse

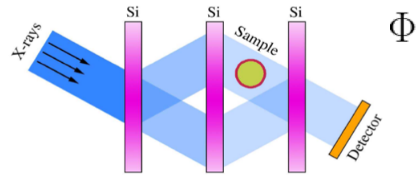

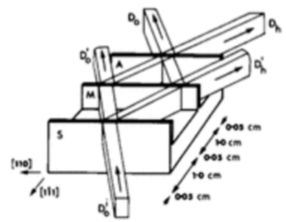

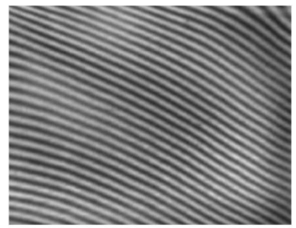

Bonse & Hart | Appl. Phys. Lett. | 1965

L3-9

Crystal Interferometry

with perfect single-crystal silicon interferometers

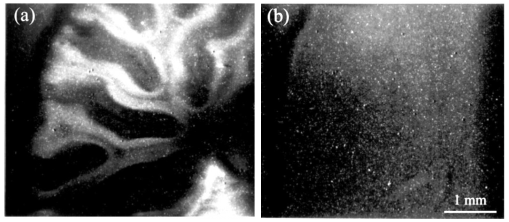

Momose et al
Medical Physics | 1995

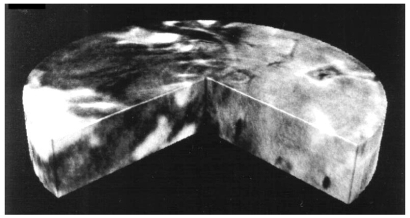

Momose et al
Nature Medicine | 1996

L3-10

The 1990s

Analyzer- and Propagation-Based Phase Contrast

L3-11

Analyzer-Based Phase-Contrast Imaging (ABI)

a.k.a. Diffraction-Enhanced Imaging (DEI)

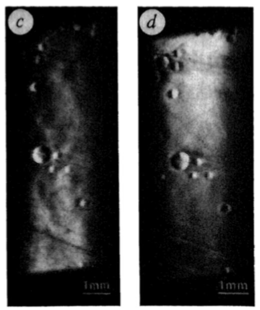

Davis et al | Nature | 1995

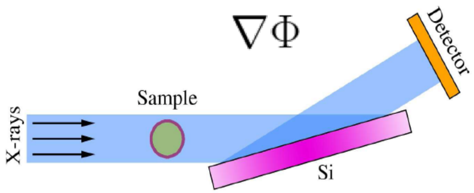

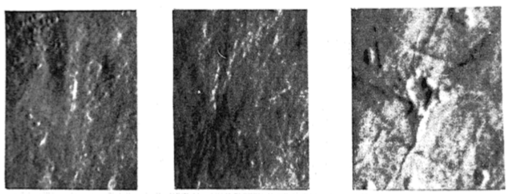

Ingal & Beliaevskaya | J. Physics D | 1995

L3-12

Propagation-Based Phase-Contrast Imaging

uses Fresnel nearfield diffraction

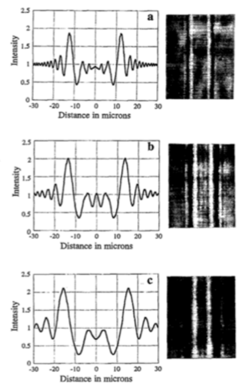

Snigirev et al | RSI | 1995

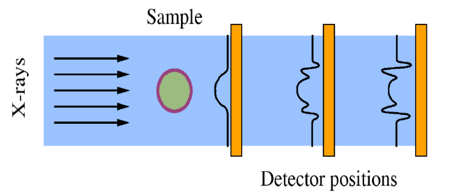

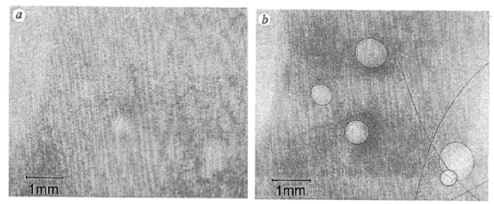

Wilkens et al | Nature | 1996

L3-13

Propagation-Based Phase-Contrast Imaging

de facto standard @ synchrotron sources

Big synchrotrons (ESRF)

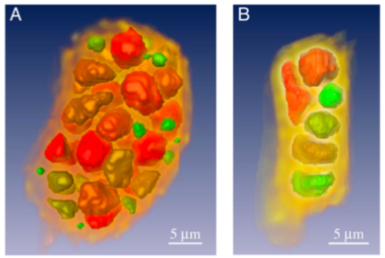

Cloetens et al | PNAS | 2007

Compact synchrotrons (MuCLS)

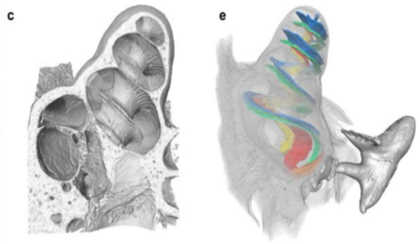

Toppervien et al | Sci Rep | 2018

L3-14

Propagation-Based Phase-Contrast Imaging

works also with high-resolution microfocus lab sources

Microfocus lab sources (Zeiss Xradia Versa 520)

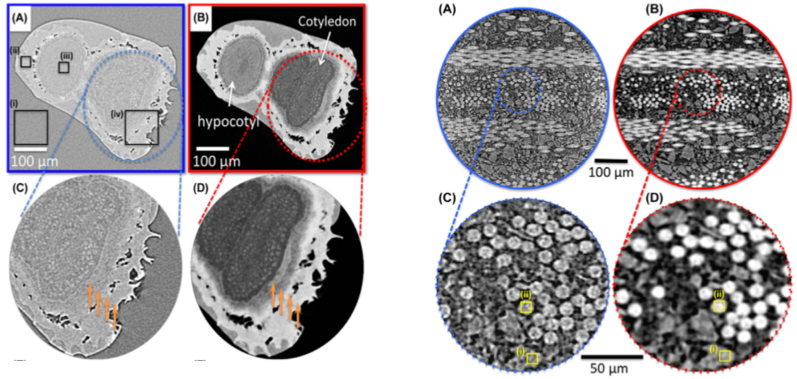

Bidola et al | Journal of Microscopy | 2017

L3-15

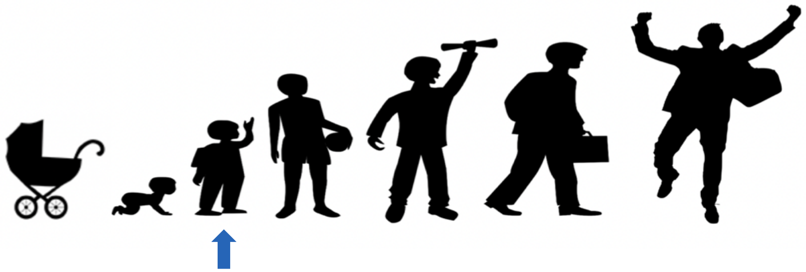

Early 2000s – Teenage Years

Grating-Based Phase Contrast @ Synchrotron Sources

L3-16

Grating-Based X-Ray Phase Contrast

pioneering works at synchrotron sources

ESRF

$\nabla\Phi$

Spring8

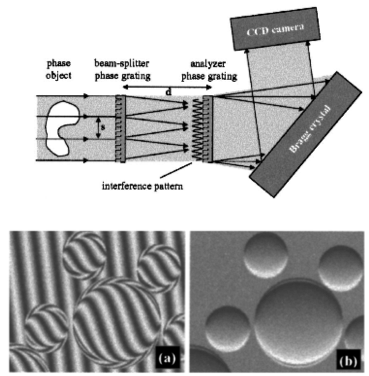

David et al | Appl Phys Lett | 2002

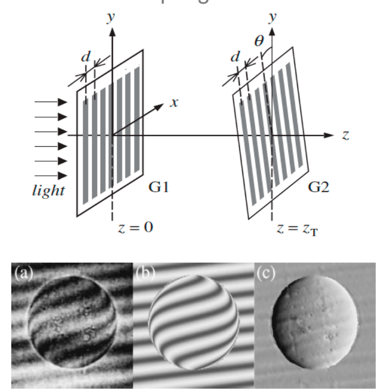

Momose et al | JJAP | 2003

L3-17

Grating-Based X-Ray Phase Contrast

measures **refraction** of X-ray waves in the object

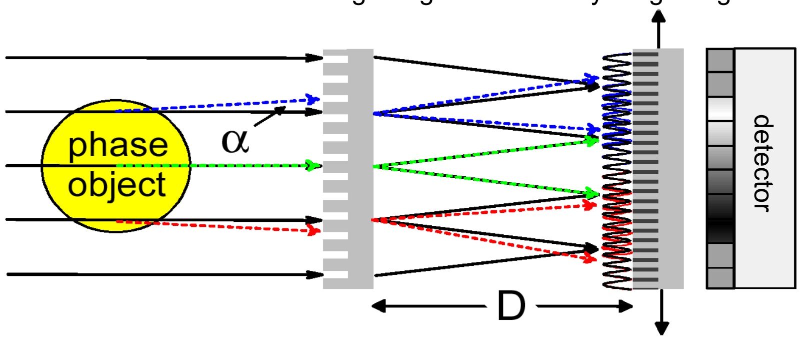

$$\alpha = \frac{\lambda}{2\pi}\nabla\Phi$$

L3-18

Talbot Effect

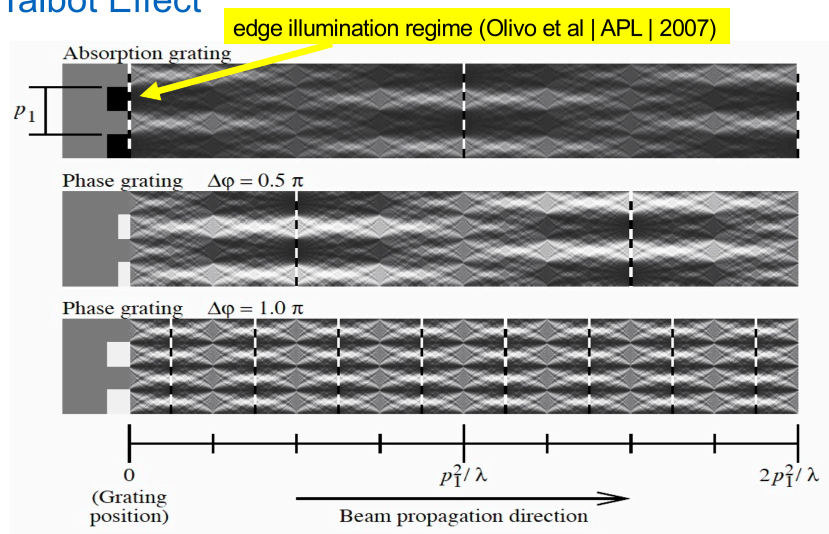

Weitkamp et al | Spie Proc | 2006

L3-19

Grating-Based X-Ray Phase Contrast CT

phase-stepping data processing and quantitative CT

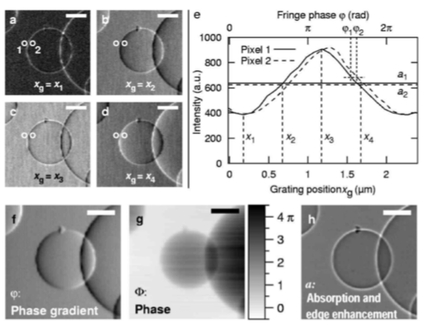

Weitkamp et al | Optics Express | 2005

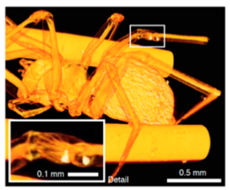

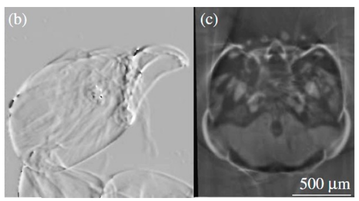

Momose et al | JJ App Phys | 2005

L3-20

Quantitative Signal Extraction

attenuation and differential phase contrast

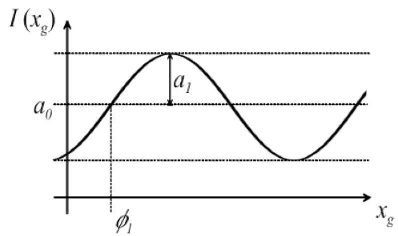

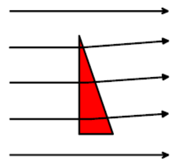

$$I(m,n,x_g) = \sum a_i(m,n)\cos(ikx_g + \phi_i(m,n))$$

$$\approx a_0(m,n) + a_1(m,n)\cos(kx_g + \phi_1(m,n$$

transmission

phase gradien

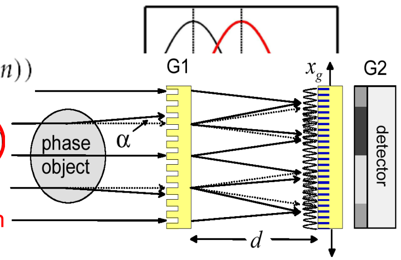

see review: Pfeiffer | AIP Conf. Proceedings (1st XNPIG) | 2012

L3-21

Quantitative CT reconstruction

incorporating the integration into the filter kernel

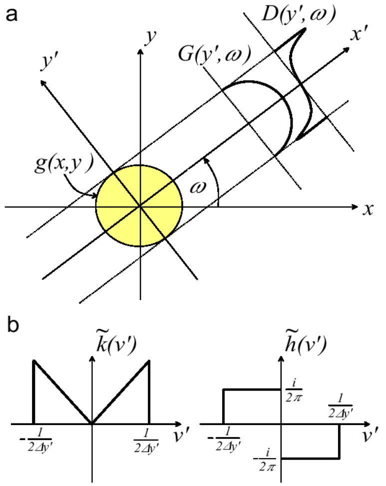

Tomographic reconstruction from absorption projections:
Filtered backprojection with Ramlak filter

$$g(x,y) = \int_0^\pi \mathcal{FT}^{-1}[\widetilde{\mathcal{G}}(v',\omega) \times \widetilde{k}(v')]\mathrm{d}\omega$$

Tomographic reconstruction from phase contrast projections:
Filtered backprojection with Hilbert filter

$$g(x,y) = \int_0^\pi \mathcal{FT}^{-1}[\widetilde{\mathcal{D}}(v',\omega) \times \widetilde{h}(v')]\mathrm{d}\omega$$

Pfeiffer et al | Phys. Rev. Lett. | 2007

L3-22

Review paper on Grating-Based Imaging

Milestones and basic principles of grating-based x-ray and neutron phase-contrast imaging
Franz Pfeiffer

Citation: AIP Conf. Proc. **1466**, 2 (2012); doi: 10.1063/1.4742261
View online: http://dx.doi.org/10.1063/1.4742261

L3-23

Late 2000s

Translation to medical x-ray tubes &

discovery of grating-based darkfield contrast

L3-24

From Synchrotrons to Medical X-ray Tubes

single slit

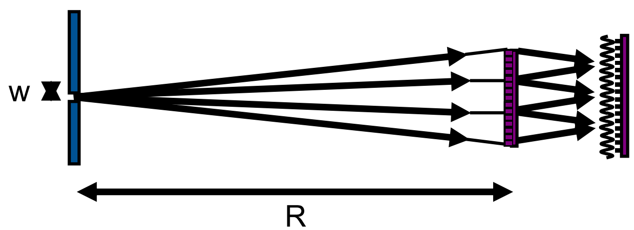

required coherence length

ξ = λR/w > p

Pfeiffer et al. | Nature Physics | 2006

L3-25

From Synchrotrons to Medical X-ray Tubes

slit array/
grating

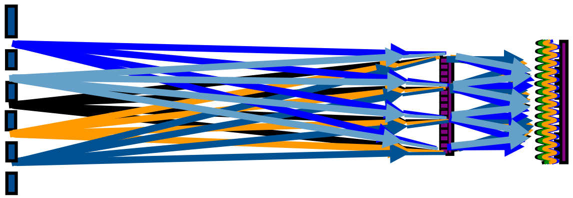

Decouples coherence from spatial resolution !

Pfeiffer et al. | Nature Physics | 2006

L3-26

Talbot-Lau Grating-Based X-Ray Phase Contrast

works also with medical X-ray tubes & incoherent sources

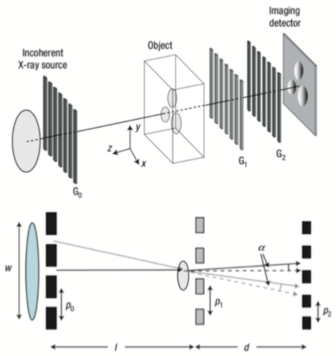

medical
X-ray tube
40 kVp

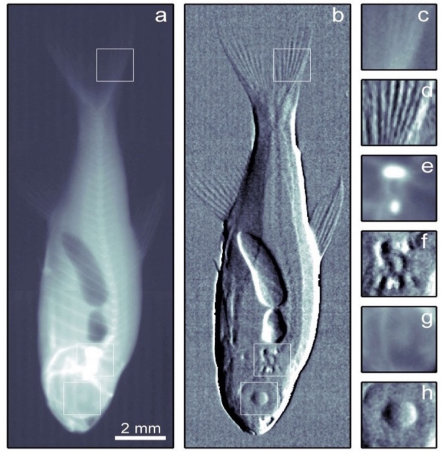

Pfeiffer et al. | Nature Physics | 2006

L3-27

Talbot-Lau Grating-Based X-Ray Phase Contrast

works also with medical X-ray tubes & incoherent sources

Pfeiffer et al. | Nature Physics | 2006

L3-28

X-Ray Phase Contrast

...more examples

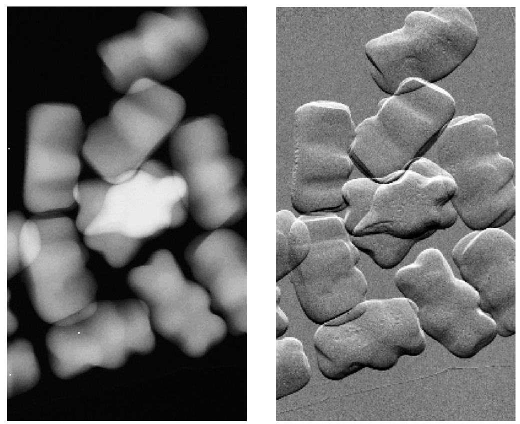

conventional X-ray

phase contrast

medical
X-ray tube
40 kVp

Pfeiffer et al. | Nature Physics | 2006

L3-29

X-Ray Phase Contrast

...more examples

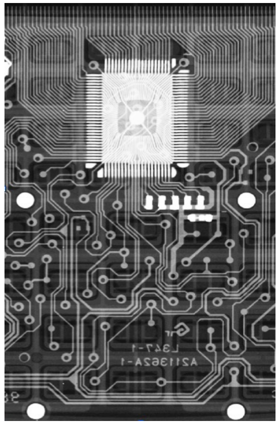

conventional X-ray

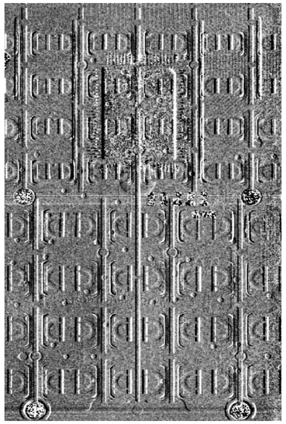

phase contrast

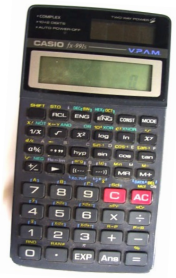

medical
X-ray tube
40 kVp

Pfeiffer et al. | Nature Physics | 2006

L3-30

Discovery of Grating-Based Darkfield Imaging

triggered by SR research on coherent diffraction

PRL **94,** 164801 (2005) PHYSICAL REVIEW LETTERS week ending 29 APRIL 2005

Shearing Interferometer for Quantifying the Coherence of Hard X-Ray Beams

F. Pfeiffer, O. Bunk, C. Schulze-Briese, A. Diaz, T. Weitkamp, C. David, and J. F. van der Veen
Paul Scherrer Institut, CH-5232 Villigen, Switzerland

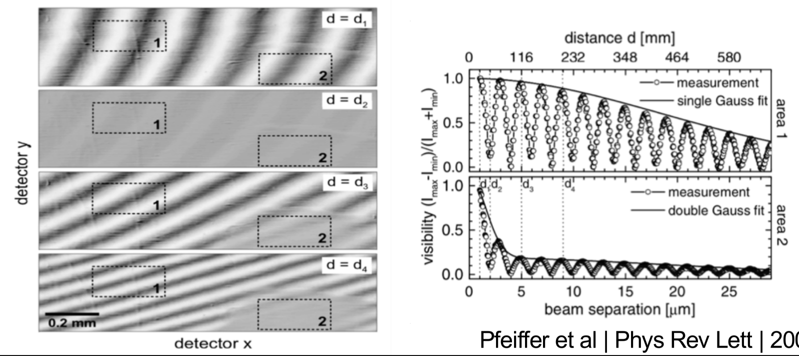

Pfeiffer et al | Phys Rev Lett | 2005

L3-31

Discovery of Grating-Based Darkfield Imaging

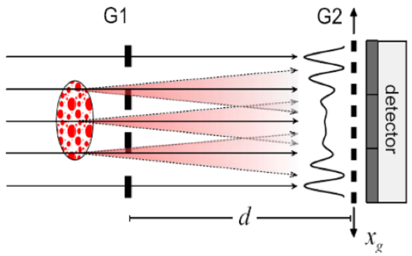

$$I(m,n,x_g) = \sum a_i(m,n)\cos(ikx_g + \phi_i(m,n))$$

$$\approx a_0(m,n) + a_1(m,n)\cos(kx_g + \phi_1(m,n))$$

transmission — scattering/ dark-field — phase gradient

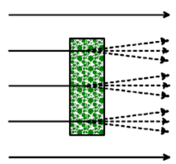

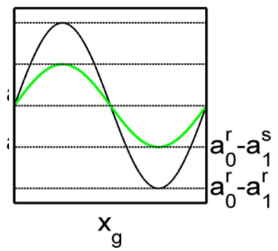

Pfeiffer et al | Nature Materials | 2008

L3-32

Darkfield Contrast

is sensitive to micro-structures in the object

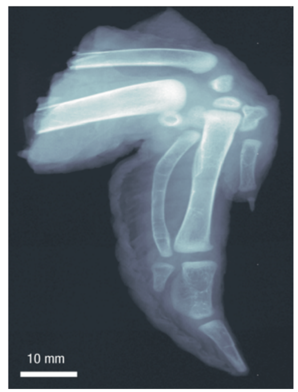

conventional X-ray

darkfield

Pfeiffer et al. | Nature Materials | 2008

L3-33

Darkfield Contrast

is sensitive to micro-structures in the object

conventional X-ray

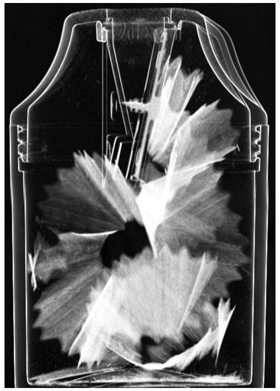

darkfield

Pfeiffer et al. | Nature Materials | 2008

L3-34

Darkfield Contrast

...is sensitive to micro-structures in the object

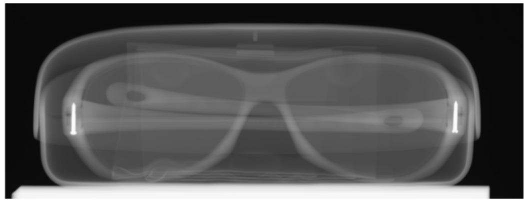

conventional X-ray

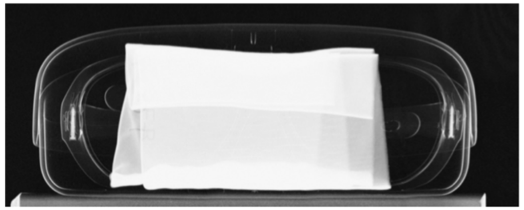

darkfield

Pfeiffer et al. | Nature Materials | 2008

L3-35

Understanding the Darkfield-Signal

introduction of „linear diffusion coefficient“ / „darkfield extinction coefficient“

$$\epsilon \equiv \frac{\sigma^2}{\Delta z} \qquad V(m,n) = \exp\left(\frac{-2\pi^2 d^2}{p_2^2} \int \epsilon_{m,n}(z)\,\mathrm{d}z\right)$$

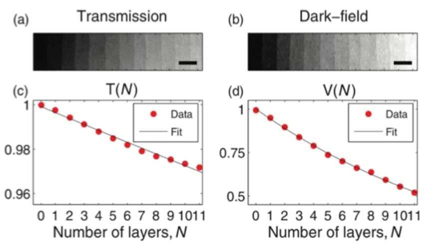

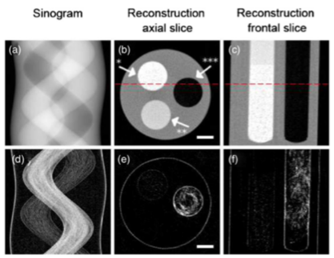

Bech et al. | Phys Med Biol | 2010

L3-36

Understanding the Darkfield-Signal

establishing relationship to correlation length

$$\frac{V}{V_0} \approx \overline{\exp\left[i\Delta\Phi_f(x,y;pd)\right]}\ ,$$
$$\approx \exp\left[-\sigma^2(x,y)\left\{1-\gamma(x,y;-pd)\right\}\right]\ .$$

$$\mu_d = \frac{3\pi^2}{\lambda^2} f|\Delta\chi|^2 d \begin{cases} D' - \sqrt{D'^2-1}(1+D'^{-2}/2) + (D'^{-1}-D'^{-3}/4) \\ \ln[(D'+\sqrt{D'^2-1})/(D'-\sqrt{D'^2-1})], & \text{for } D>d; \\ D', & \text{for } D \le d; \end{cases}$$

$$\gamma(x,y;\Delta x) \approx \exp\left[-\left\{|\Delta x|/\xi(x,y)\right\}^{2H}\right]$$

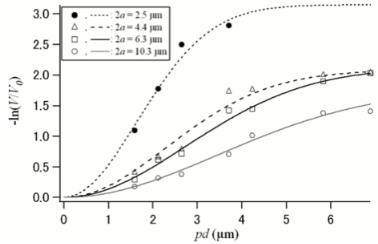

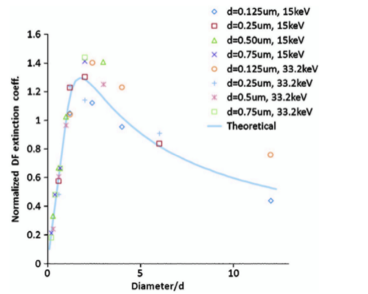

Yashiro et al. | Optics Express | 2010 & Lynch et al. | Optics Express | 2011

L3-37

Darkfield Vector Radiography

exploiting directional dependence

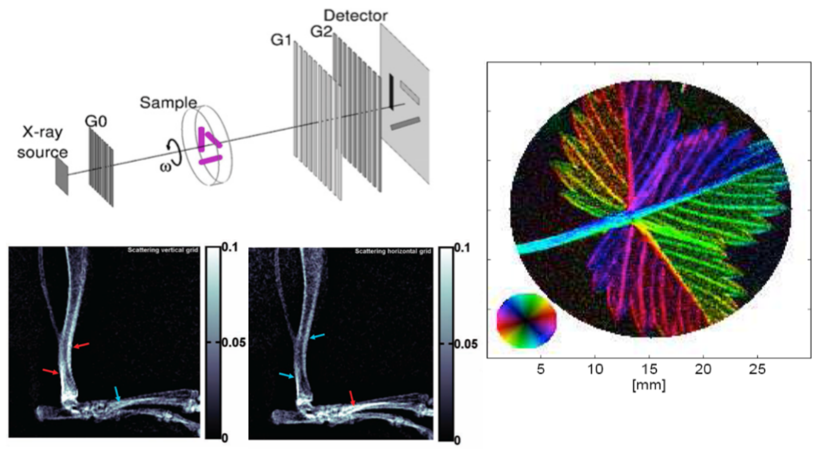

Wen et al. | Radiology | 2009 & Jensen et al. | Phys Med Biol | 2010

L3-38

Early 2010s

Ex-vivo specimen imaging to assess potential medical applications

L3-39

Ex-vivo tissue imaging

see talks in Session II

exploring the potential medical impact – **mammography**

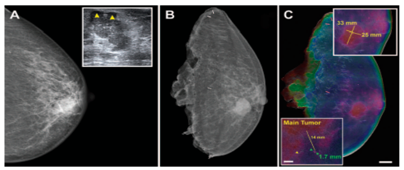

Stampanoni et al. | Inv Radiology | 2011

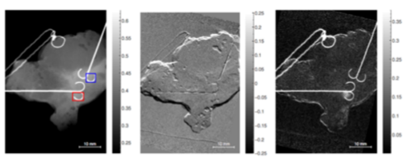

Michel et al. | Phys Med Biol | 2013
Anton et al. | ZMP | 2013

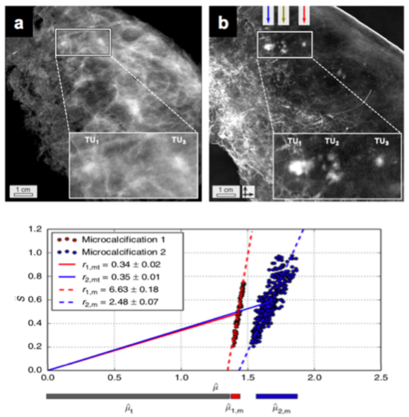

Scherer et al. | PlosOne | 2014
Scherer et al. | Nature Comm | 2016

L3-40

Ex-vivo tissue imaging

exploring the potential medical impact – **musculoskeletal imaging**

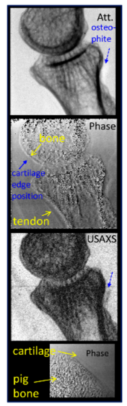

Stutman et al.
Phys Med Biol | 2011

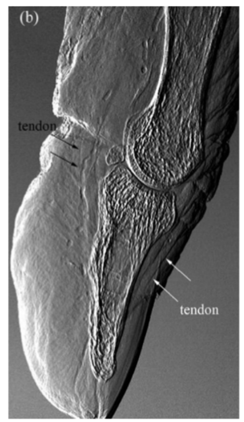

Tanaka et al.
ZMP | 2013

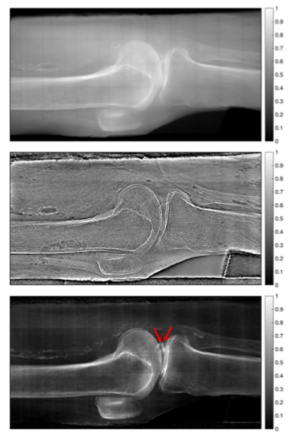

Horn et al.
Phys Med Biol | 2017

L3-41

Quantitative phase CT

'conventional' Hounsfield Units

'phase-contrast' Hounsfield Units

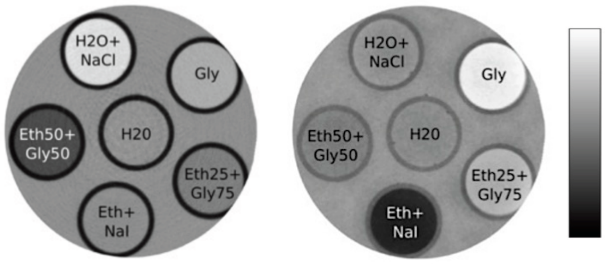

$$\frac{\mu - \mu_{water}}{\mu_{water} - \mu_{air}}$$

$$\frac{\delta - \delta_{water}}{\delta_{water} - \delta_{air}}$$

Tapfer et al | Med Phys | 2011 [see also before: Herzen et al | Opt Express | 2009]

L3-42

Ex-vivo tissue imaging

see talk by Julia Herzen

exploring the potential medical impact – **breast CT**

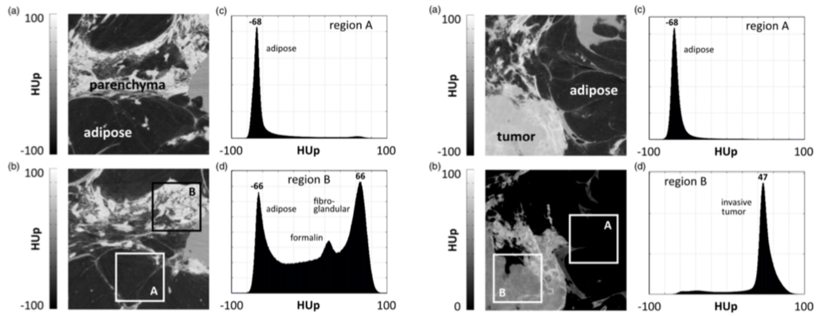

Willner et al. | Phys Med Biol | 2013; Grandl et al. | ZMP | 2013
Grandl et al. | PlosOne | 2014; Grandl et al. | Eur Rad | 2015

L3-43

Ex-vivo tissue imaging

exploring the potential medical impact – **cardiovascular CT**

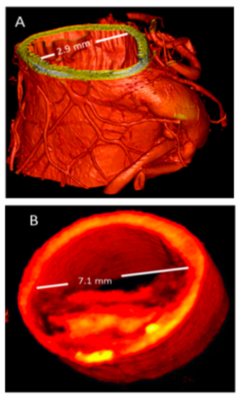

Saam et al.
PlosOne | 2013

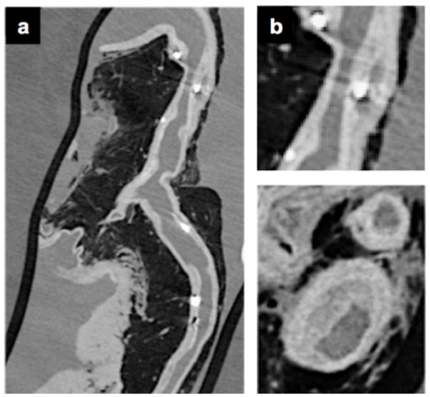

Hetterich et al. | Radiology | 2014
Hetterich et al. | Inv Radiology | 2015

L3-44

Ex-vivo tissue imaging

exploring the potential medical impact – **stone classification & CAs**

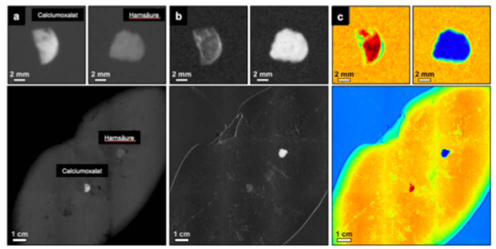

Scherer et al.
Scientific Reports | 2015

Velroyen et al.
PlosOne | 2015

L3-45

Ex-vivo tissue imaging

exploring the potential medical impact – **lung diseases**

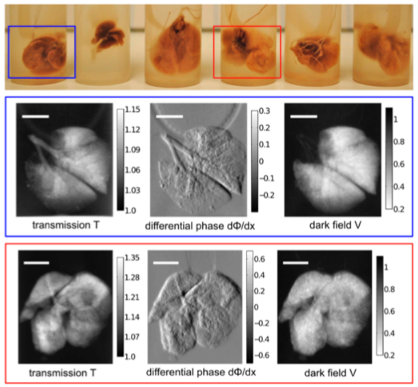

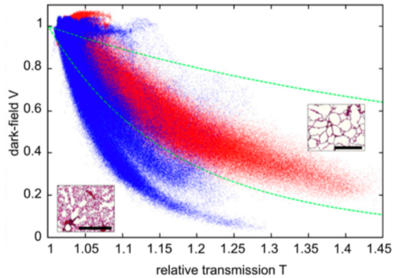

Schleede et al. | PNAS | 2012
Meinel et al. | PlosOne | 2013
Yaroshenko et al. | Radiology | 2013

L3-46

High-sensitivity Farfield Interferometry

with submicron-period phase gratings

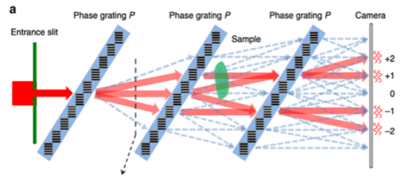

Wen et al. | Nature Communications | 2014

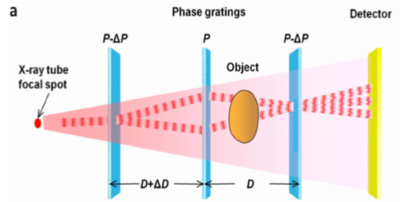

Wen et al. | Scientific Reports | 2015

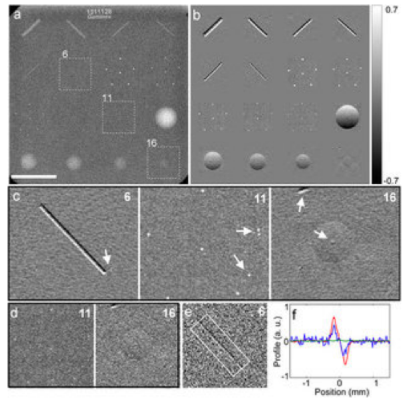

L3-47

Darkfield Tensor CT

see talks in Session III

solving the 6D tensorial scattering reconstruction problem

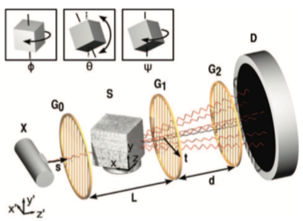

$$D(x,y) = \exp\left[-\int \sum_i (|\boldsymbol{\epsilon}_i(x,y,z)|\,|\boldsymbol{t}|)^2 \cdot (|\hat{\boldsymbol{s}} \times \hat{\boldsymbol{\epsilon}}_i|\,\langle \hat{\boldsymbol{\epsilon}}_i, \hat{\boldsymbol{t}} \rangle)^2 \, \mathrm{d}z\right].$$

Malecki et al. | Eur Phys Lett | 2014
Sharma et al. | Appl Phys Lett | 2016
Sharma et al. | Scientific Reports | 2017
...

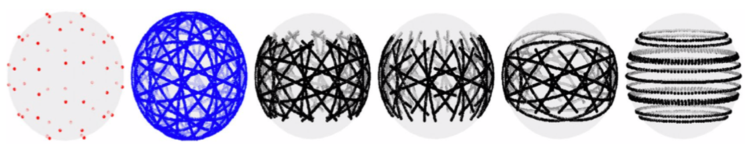

(a) (b) (c) (d) (e) (f)

L3-48

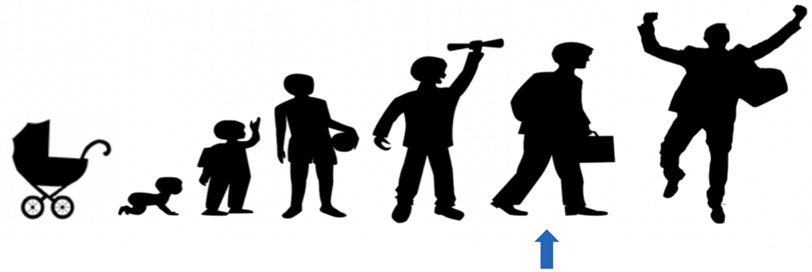

Late 2010s – Adulthood

Translation to Pre-Clinical Small-Animal Imaging & Research

L3-49

First Step: Mouse-CT

first phase-contrast small-animal CT

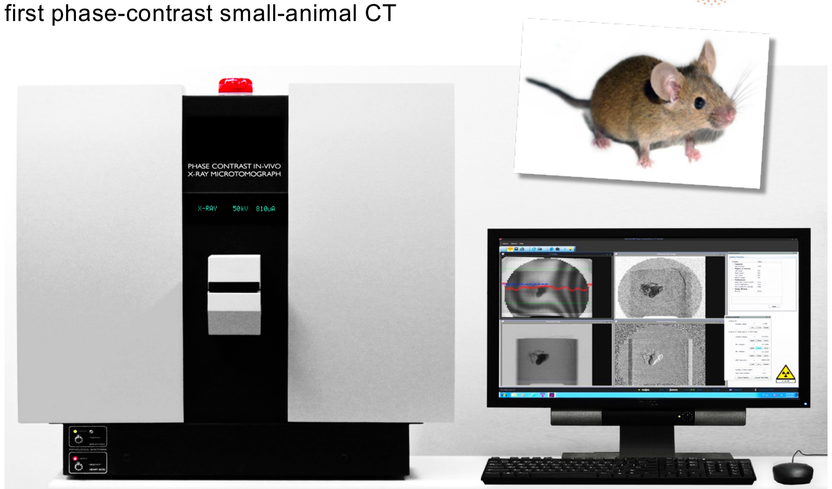

Tapfer et al | Med. Phys. | 2011; Tapfer et al | PNAS | 2012

L3-50

First Step: Mouse-CT

first phase-contrast small-animal CT

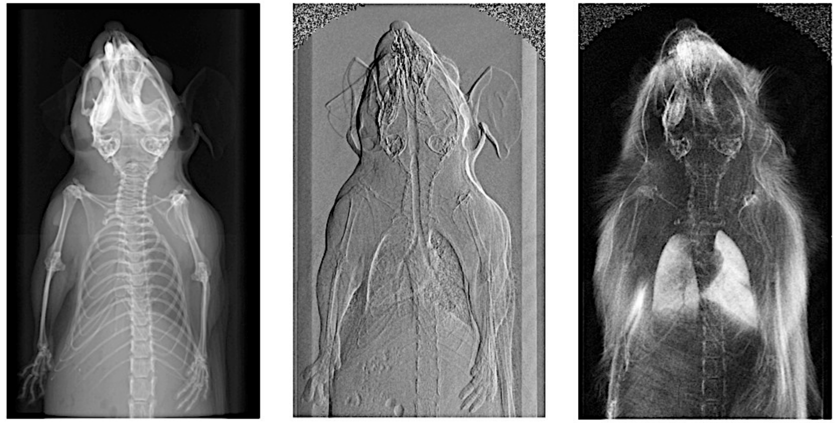

conventional X-ray | phase contrast | darkfield

Bech et al | Nature Sci. Rep. | 2013

L3-51

Medical Relevance

for lung diseases

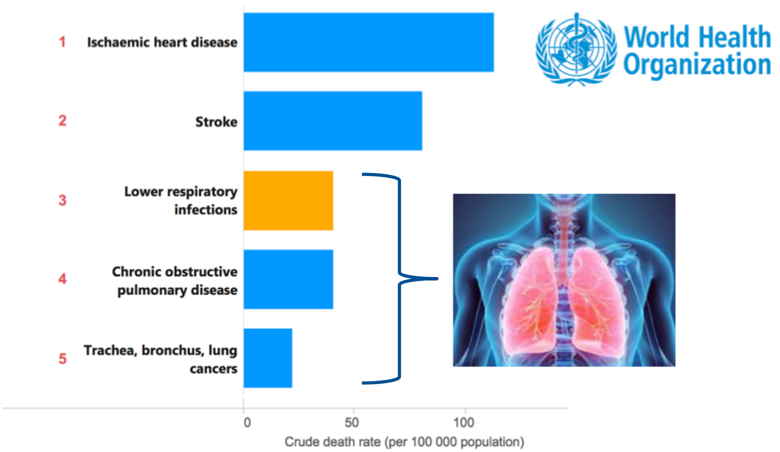

http://www.who.int/mediacentre/factsheets/fs310/en/

L3-52

COPD

chronic obstructive lung disease (ca. 5 Mio. total in Germany)

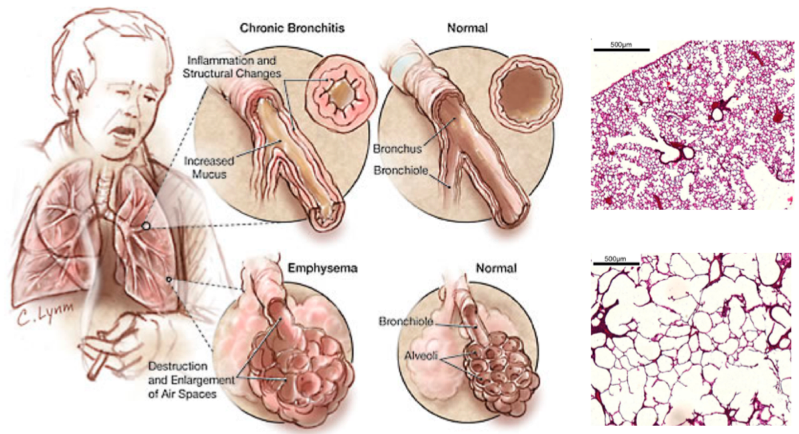

L3-53

Preclinical Study on COPD-Detection in Mice

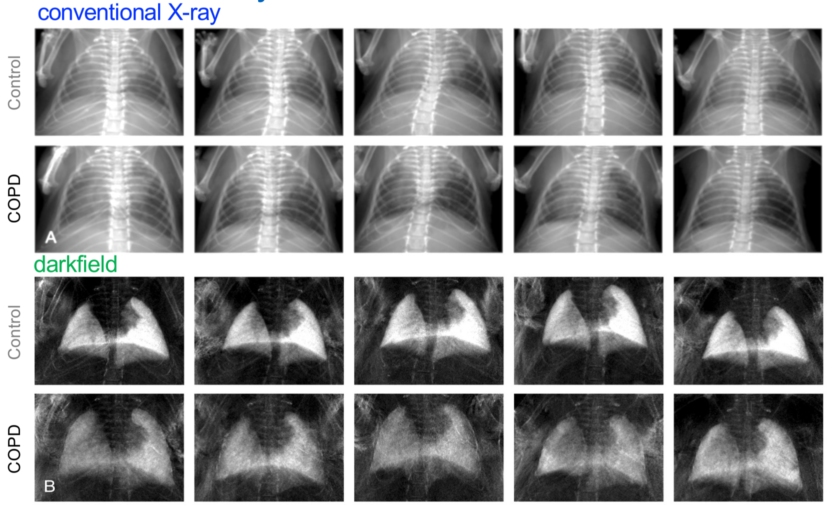

Meinel et al | PlosOne | 2013; Yaroshenko et al | Radiology | 2013
Meinel et al | Inv. Radiology | 2014; Hellbach et al | Inv. Radiology | 2015

L3-54

Preclinical Study on COPD-Detection in Mice

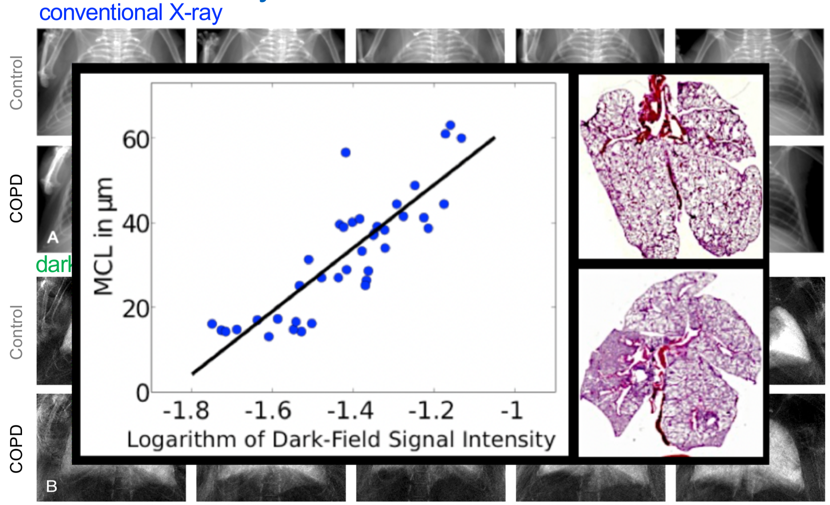

Meinel et al | PlosOne | 2013; Yaroshenko et al | Radiology | 2013
Meinel et al | Inv. Radiology | 2014; Hellbach et al | Inv. Radiology | 2015

L3-55

Preclinical Study on Lung Cancer in Mice

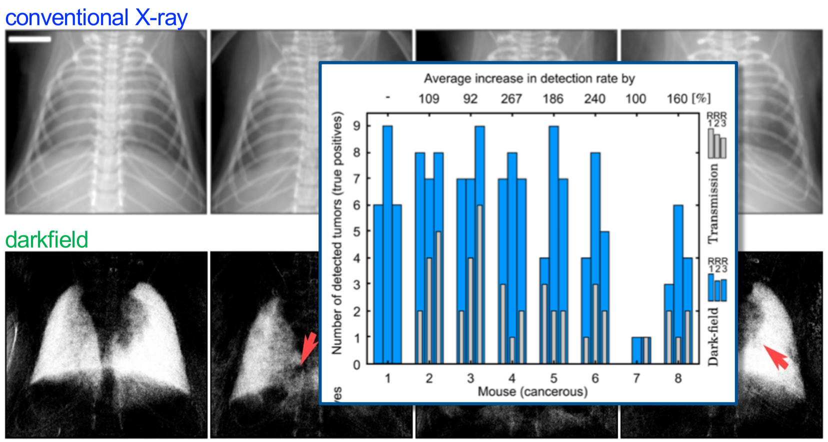

=> **244 %** improvement in lesion detection on chest X-rays !

Scherer et al. | Nature Sci. Rep. | 2017

L3-56

Preclinical Study on Lung Fibrosis in Mice

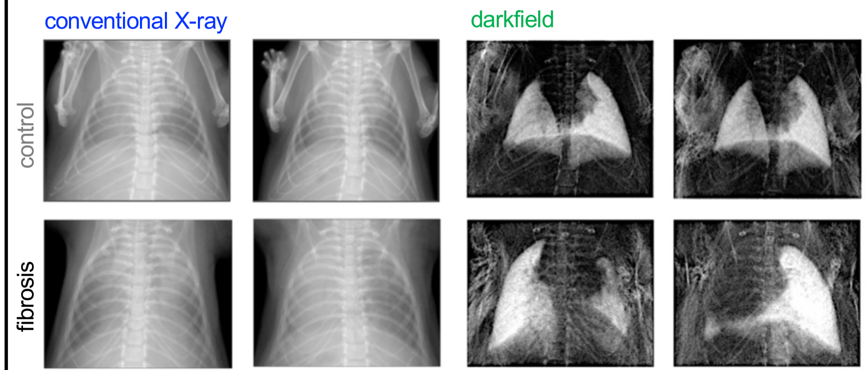

Yaroshenko et al. | Scientific Reports | 2015

L3-57

First In-Vivo Multi-Contrast X-Ray CT

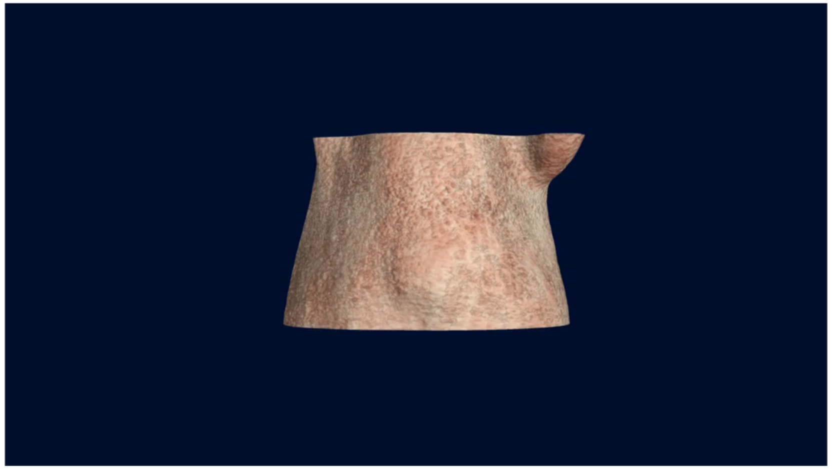

www.youtube.com/watch?v=WeiADQ0h3B4

Velroyen et al. | EBiomedicine | 2015

L3-58

Next Step: Darkfield "Pig-Scanner"

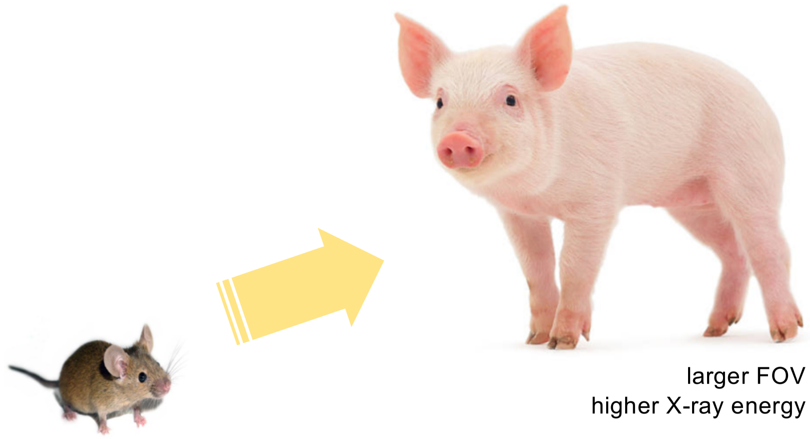

larger FOV
higher X-ray energy

L3-59

Darkfield Pig-Scanner

worldwide first in-vivo large-animal proof-of-principle

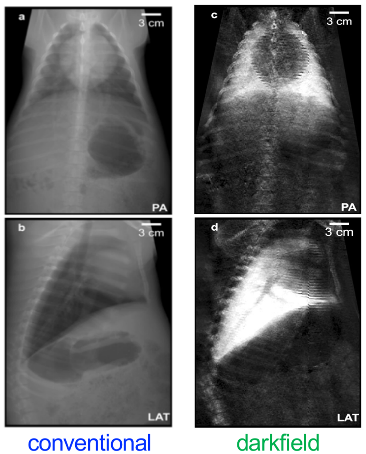

med. X-ray generator 70 kVp
10 sec scan time
dose 80 µSv

Gromann et al. | Scientific Reports | 2017

L3-60

Darkfield Pig-Scanner

improved pneumothorax detection demonstrated

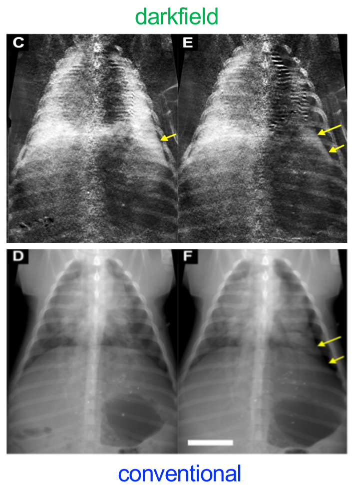

med. X-ray generator 70 kVp
10 sec scan time
dose 80 µSv

Hellbach et al. | Scientific Reports | 2018

L3-61

Starting Now & Future – Application on Patients

Translation to Clinical Application & Commercialization

L3-62

Work Toward Patient Applications

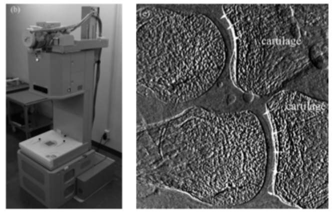

Tanaka et al. | ZMP | 2013

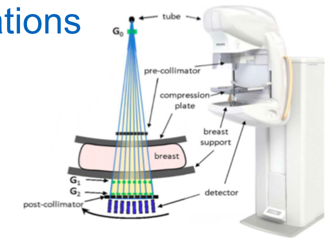

Koehler et al. | Med Phys | 2015

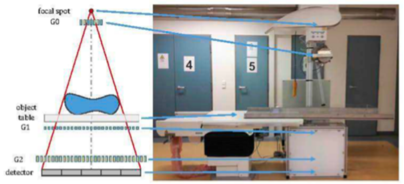

Hauke et al. | Med Phys | 2018

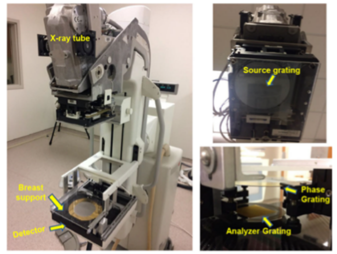

Li et al. | Proc SPIE | 2018

L3-63

First Darkfield Chest X-ray Prototype for Humans

extensive phantom studies

conventional chest X-ray | darkfield chest X-ray

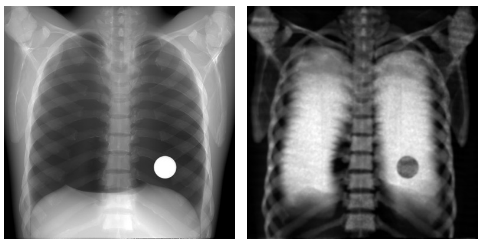

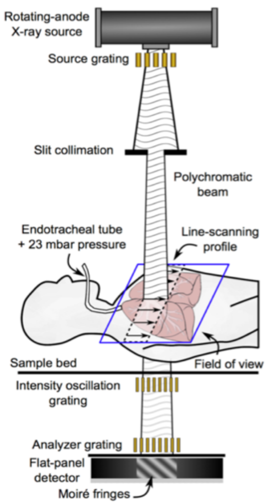

Willer et al. | PlosOne | 2018
de Marco/Fingerle et al. | Eur. Rad. Exp. | 2019
Sauter/Andrejewski et al. | Scientific Reports | 2019

L3-64

First Darkfield Chest X-ray Prototype for Humans

worldwide first ex-vivo darkfield human chest x-rays

conventional chest X-ray | darkfield chest X-ray

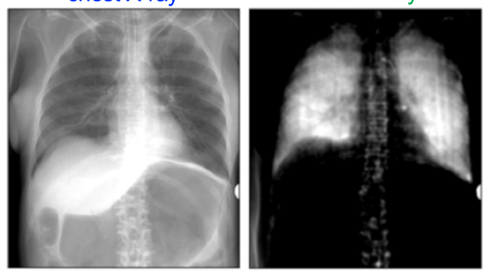

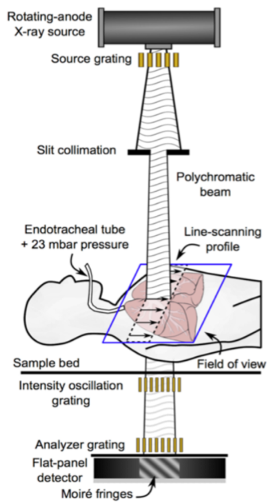

Willer et al. | PlosOne | 2018
de Marco/Fingerle et al. | Eur. Rad. Exp. | 2019
Sauter/Andrejewski et al. | Scientific Reports | 2019

L3-65

First Darkfield Chest X-ray Prototype for Humans

worldwide first ex-vivo darkfield human chest x-rays

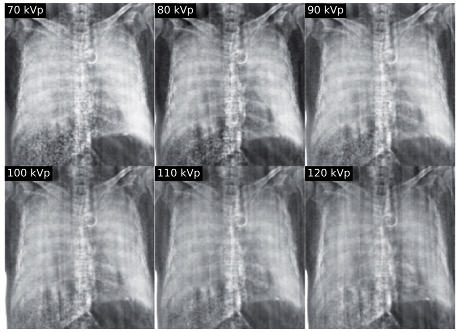

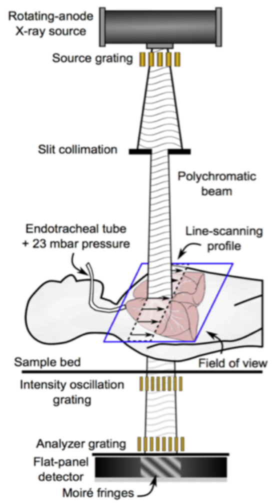

Willer et al. | PlosOne | 2018
de Marco/Fingerle et al. | Eur. Rad. Exp. | 2019
Sauter/Andrejewski et al. | Scientific Reports | 2019

L3-66

First Results with Patients

see talks in Session I & IX

...from prototype in Munich will be presented at this conference (tomorrow)

COPD study > 500 Patienten

Bundesamt für Strahlenschutz

L3-67

Acknowledgements

www.e17.ph.tum.de

Klaus Achterhold, Sebastian Allner, Jana Andrejewski, Alan Begic, Lorenz Birnbacher, **Margarete Kattau,** Nelly de Leiris, Fabio de Marco, Manuela Frank, Alex Gustschin, Nikolai Gustschin, **Martin Dierolf**, **Julia Herzen, Wolfgang Noichl,** Eva Prexl, Dieter Renker, Stephan Umkehrer, **Theresa Urban, Rafael Schick,** Max von Teuffenbach, Manuel Viermetz, Konstantin Willer, ...

Klinikum rechts der Isar Technische Universität München

Thomas Baum, **Alexander Fingerle**, Michael Molls, Fridtjof Nüsslin, **Daniela Pfeiffer,** Bernhard Renger, **Ernst Rummeny**, Andreas Sauter

LMU KLINIKUM

Katharina Hellbach, **Maximilian Reiser**

HelmholtzZentrum münchen
Deutsches Forschungszentrum für Gesundheit und Umwelt

Silke Meiners, Otmar Schmid, Ali Yildirim

MSB

Bernhard Gleich, Axel Haase

KIT Karlsruher Institut für Technologie

Pascal Meyer, **Jürgen Mohr**, **Joachim Schulz**, Tobias Schröter

PHILIPS

Ami Altman, Michael Heider, **Thomas Köhler**, Ingo Maack, Roland Proksa, **Karsten Rindt, Andre Yaroshenko**

DFG Deutsche Forschungsgemeinschaft

erc European Research Council

Bundesministerium für Bildung und Forschung

Tutorial 4

(15:50 – 16:20)

Introduction to tomographic image reconstruction

Marco Stampanoni

Paul Scherrer Institut / Eidgenössische Technische

Hochschule Zürich,

Switzerland

L4-1

ETH zürich

Introduction to Tomographic Image Reconstruction

Marco Stampanoni

Institute for Biomedical Engineering, University and ETH Zürich
Swiss Light Source, Paul Scherrer Institut

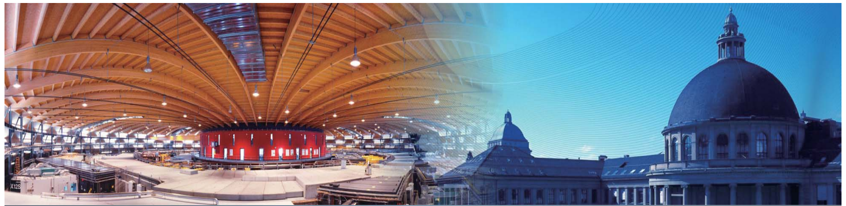

L4-2

ETH zürich

Beer-Lambert's law

$$I = \int_0^{E_{\max}} I_0(E) \cdot e^{-\int_{-\infty}^{\infty} \mu(E,x) \cdot dx} \, dE$$

object dependence

energy dependence

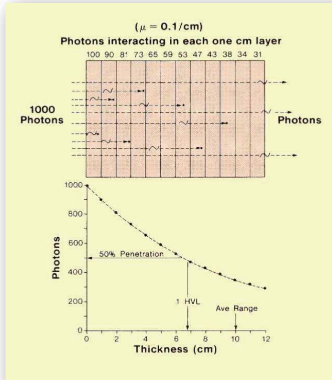

- "Photons do not have the same range, even when they have the same energy"
- "Some of the photons travel a relatively short distance before interacting, whereas others pass through or penetrate the object"

L4-3

ETH zürich

Contrast definition

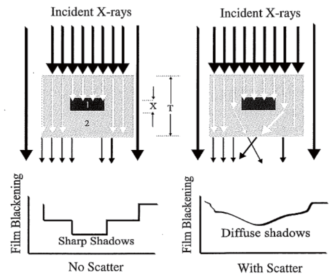

$$\boxed{\text{Definition: } C = \frac{I_1 - I_2}{I_2}}$$

$$I_1 = P_1 + S_1 \quad I_2 = P_2 + S_2 \quad \xrightarrow{\text{Beer-Lambert}} \quad P_1 = Ne^{-\mu_1 x} \times e^{\mu_2 (T-x)} \quad P_2 = Ne^{-\mu_2 T}$$

$$C = \frac{N(e^{-(\mu_1-\mu_2)x} e^{-\mu_2 T}) + S_1 - S_2}{Ne^{-\mu_2 T} + S_2}$$

Using $e^{-x} \approx 1 - x$ for small x

and assuming $S_1 \cong S_2$ we can write:

$$C \cong \frac{(\mu_1 - \mu_2)x}{1 + R} \quad \text{where } R \cong \frac{S_2}{Ne^{-\mu_2 T}}$$

- Contrast maximized by increasing attenuation coefficient difference
- Small scatter contributes to higher contrast

C. Guy, The Principles of Medical Imaging, 2005

L4-4

ETH zürich

Blur vs contrast

- Blurring is present in all imaging processes
- In an ideal situation, each small point within an object would be represented by a small, well-defined point within the image. In reality, the "image" of each object point is spread, or blurred, within the image.
- Blur has little effect on the visibility of large objects but it reduces the contrast and visibility of small objects.
- Relationship between spatial resolution and contrast!!

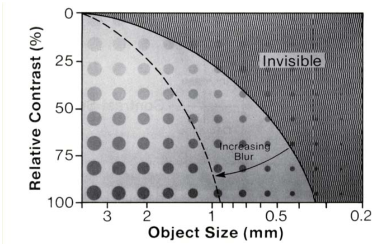

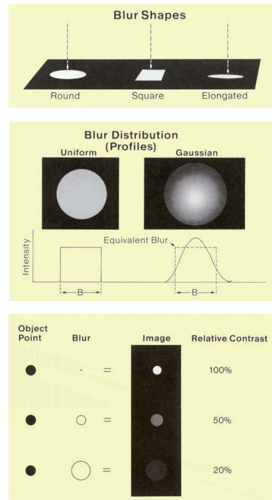

L4-5

ETH zürich

Contrast Transfer Curves

- The resolving ability, or resolution, of an imaging system is relatively easy to measure and is often used to evaluate system blur.
- The common practice is to describe the line width and separation distance in terms of line pairs (lp) per unit distance (millimeters or centimeters). One line pair consists of one lead strip and one adjacent separation space.
- The number of line pairs per millimeter is actually an expression of spatial frequency. As the lines get smaller and closer together, the spatial frequency (line pairs per millimeter) increases.
- A typical test pattern contains areas with different spatial frequencies.
- An imaging system is evaluated by imaging the test object and observing the highest spatial frequency (or minimum separation) at which the separation of the lines is visible

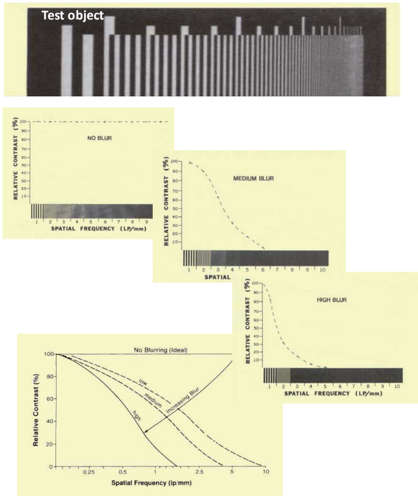

L4-6

ETH zürich

Computed Tomography

L4-7

ETH zürich

Computed tomography: from 2D to 3D

→ Computed tomography!

L4-8

ETH zürich

2D - 3D - 4D

Radiography

Tomoscopy

(gated tomography, kHz time resolution)

L4-9

ETH zürich

Slicing Imaging – Why ?

- Tomography means imaging by sections or slices.
  (From the Greek word tomos, meaning "a section" or "a cutting)

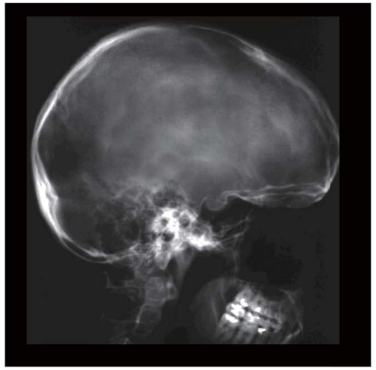

Radiographic projection

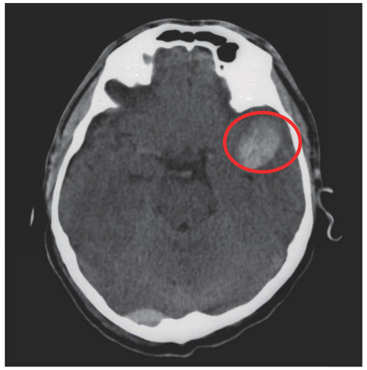

Tomographic slice

L4-10

ETH zürich

Tomographic vs Radiographic Imaging

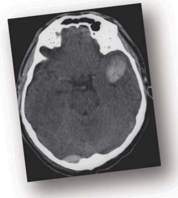

- Radiographic imaging:
  - 3D structures collapsed
  - Not quantitative
- Tomographic imaging:
  - 3D structure solved
  - Computed image reconstruction

HIGH CONTRAST !!

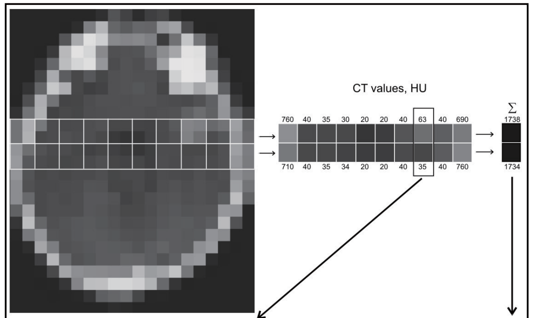

CT image:

High local contrast of soft tissue structures

$$Contrast = \frac{I_1 - I_2}{(I_1+I_2)/2} = \frac{(63-25)}{(63+35)/2} = 0.57$$

X-ray image:

Low contrast of soft tissue structures due to superposition of bones

$$Contrast = \frac{I_1 - I_2}{(I_1+I_2)/2} = \frac{(1738-1734)}{(1738+1734+35)/2} = 0.0023$$

L4-11

ETH zürich

Beer-Lambert law

- Homogeneous object, monochromatic radiation

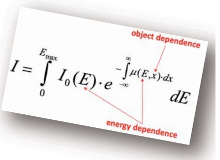

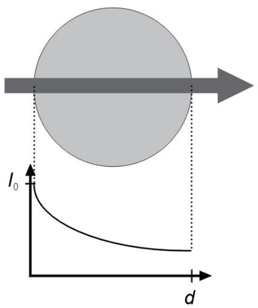

$$I = I_0 \cdot e^{-\mu d}$$

$$P = ln\frac{I_0}{I} = \mu d$$

$$\mu = \frac{P}{d} = \frac{1}{d} ln\frac{I_0}{I}$$

μ = linear attenuation coefficient
$\mu = (\tau + \sigma + \kappa)$

L4-12

ETH zürich

Beer-Lambert law

- Inhomogeneous object, polychromatic radiation

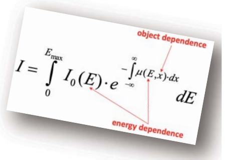

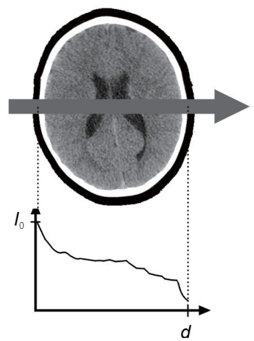

$$I = \int_0^{E_{max}} I_0(E) \cdot e^{-\int_0^d \mu(E,z)dz} dE$$

$$\mu(z) = ?$$

$$I = I_0 \cdot e^{-\int_0^d \mu(z)dz}$$

$$P = ln\frac{I_0}{I} = \int_0^d \mu(z)dz$$

Radon Transform, i.e. integral of a function over a (straight) line...

L4-13

ETH zürich

Beer-Lambert law

- Arbitrary Object:

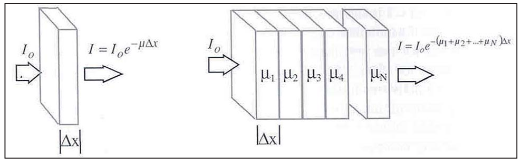

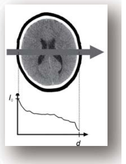

- It holds : $I = I_0 e^{-\mu_1\Delta x} e^{-\mu_2\Delta x}\, e^{-\mu_3\Delta x} \ldots e^{-\mu_n\Delta x} = I_0 e^{-\sum_{n=1}^{N}\mu_n\Delta x}$
- Define the projection measurement: $\boxed{p} = \ln\left(\frac{I_0}{I}\right) = \sum_{n=1}^{N}\mu_N\Delta x = \int_L \boxed{\mu(x)}dx$?

The question is: Given the (1D) measured projections, corresponding to the line integrals of the attenuation coefficient, how do we reconstruct its (2D) distribution?

L4-14

ETH zürich

Projection data: demonstration

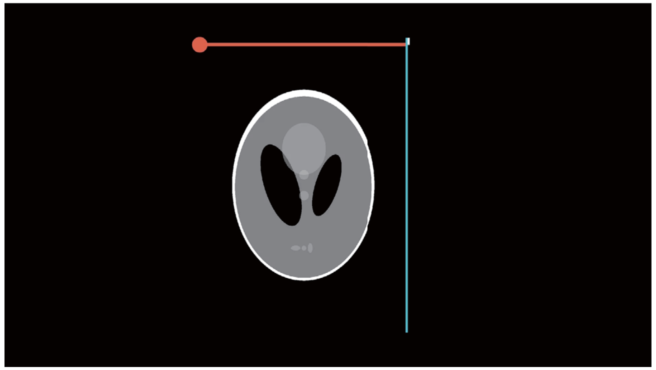

https://youtu.be/TbLaQo3rgEE

L4-15

ETH zürich

Computed tomography: from 2D to 3D

L4-16

ETH zürich

Acquisition schemes: point detector

- Simplest beam geometry
- Integrating one detector pixel at a time

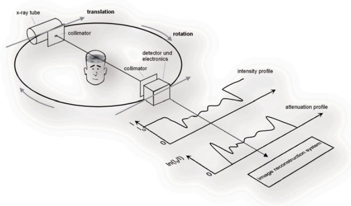

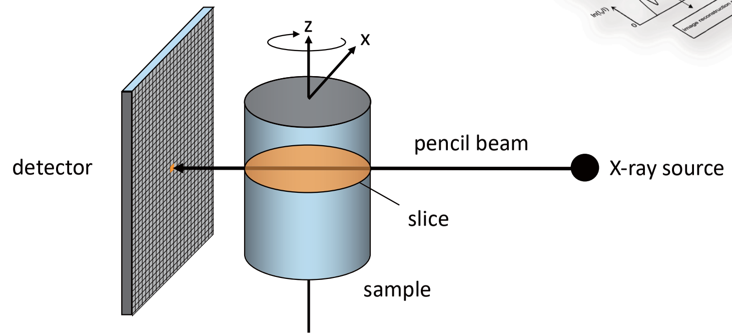

L4-17

ETH zürich

Acquisition schemes: line geometry

- Integrating a row of detector pixels at a time (→ faster scans)

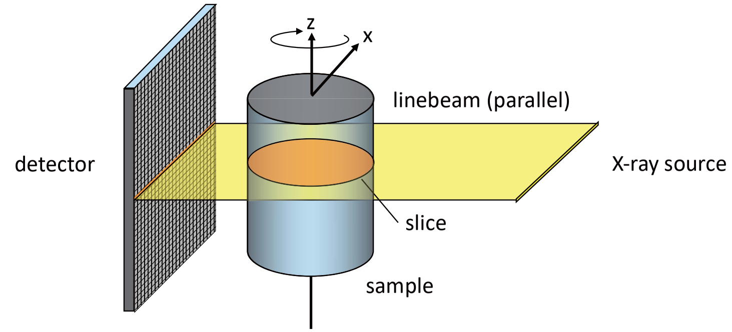

L4-18

ETH zürich

Acquisition schemes: parallel beam geometry

- Integrating a 2D array of pixels at a time, very fast
- Simple reconstruction algorithm

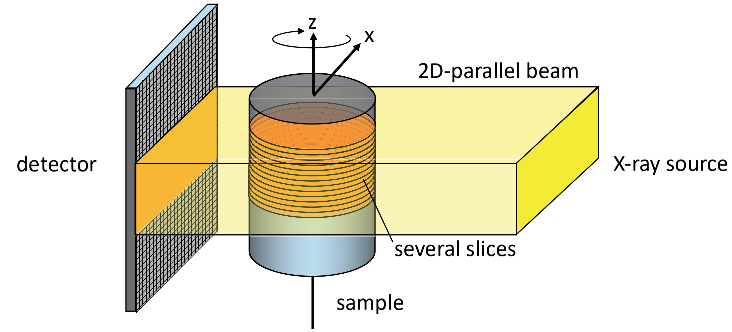

L4-19

ETH zürich

Acquisition schemes: fan-beam geometry

- Integrating a row of pixels at a time
- Magnification effect by fan geometry

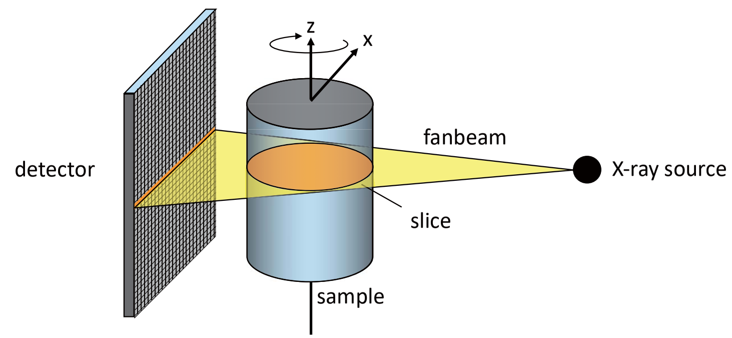

L4-20

ETH zürich

Acquisition schemes: cone-beam geometry

- Integrating a 2D array of pixels at a time
- Magnification effect by cone geometry
- Reconstruction is non-trivial, since beam travels through different slices

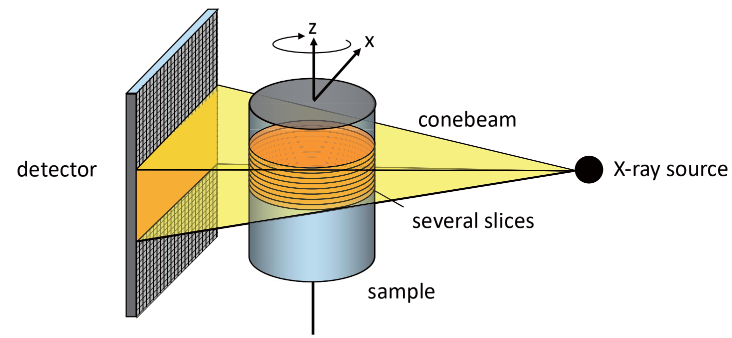

L4-21

ETH zürich

Tomographic reconstruction algorithms

- Fundamental Tools:
  - Radon Transform
  - Fourier Slice Theorem
- Analytical algorithms
  - Direct Fourier Methods
  - Filtered backprojection
- Iterative algorithms
  - Algebraic
  - Statistical

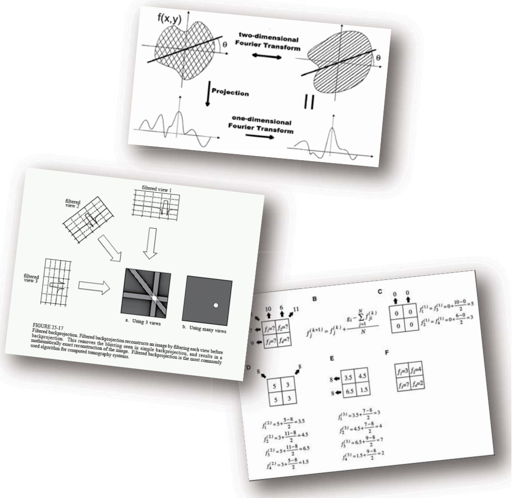

L4-22

ETH zürich

Direct inversion (historic)

- Brute force approach
  - N equations with N unknowns
  - Need more than N² equations to ensure linear independence

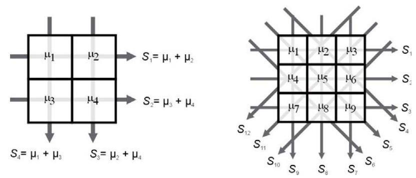

- Sir Godfrey Hounsfield (in the late 60s)
  - Reconstructed the first human head
  - Solved 28000 equations simultaneously
  - Nobel Prize in 1979 together with A. Cormack

L4-23

ETH zürich

Radon transform

- The Radon transform in 2D is the integral of a function over straight lines and therefore represents the projections data as obtained in a tomographic scan

$$R(t,\phi) = \int_l \mu(x,y)\,dl$$

$$R(t,\phi) = P_\phi(t) := -\ln\left(\frac{I_\phi(t)}{I_0}\right)$$

$$R(t,\phi) = \int_{-\infty}^{+\infty}\int_{-\infty}^{+\infty} \mu(x,y)\,\delta(x\cos\phi + y\sin\phi - t)\,dx\,dy$$

Wanted !

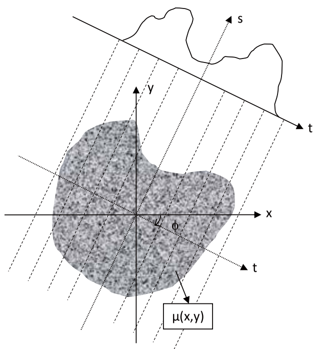

L4-24

ETH zürich

Radon Transform aka "sinogram"

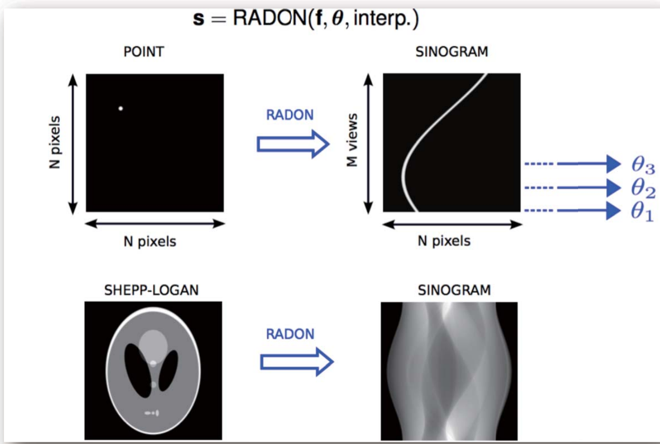

The Radon transform is often called a sinogram because the Radon transform of a Dirac delta function corresponds to the graph of a sine wave

L4-25

ETH zürich

Sinogram formation: demonstration

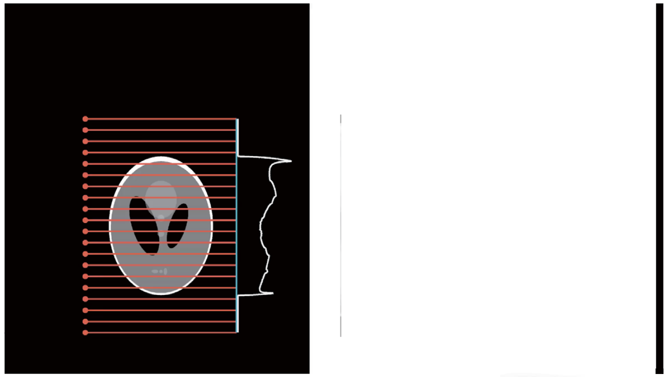

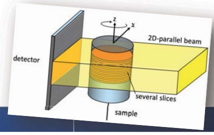

https://youtu.be/5Vyc1TzmNI8

L4-26

ETH zürich

Radon transform

- The Radon transform was introduced by Johann Radon, who also provided a formula for the inverse transform
- The inverse of the Radon transform can be used to reconstruct the original density from the projection data, and thus it forms the mathematical underpinning for tomographic reconstruction
- Radon found the solution to the tomographic problem already in 1917
  - but assumed an infinite number of projections and continuous projection functions
  - while we only have a finite number of projections and a finite number of detector points

$$R(t,\phi) = \int_{-\infty}^{+\infty} \int_{-\infty}^{+\infty} \mu(x,y)\,\delta(x\cos\phi + y\sin\phi - t)\,dx\,dy$$

Wanted !

L4-27

ETH zürich

Fourier Slice Theorem

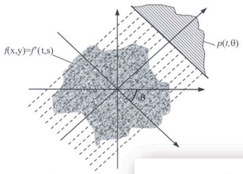

The Fourier transform of a parallel projection of an object f(x,y) obtained at an angle θ equals a line of the 2D Fourier transform of f(x,y) taken at the same angle.

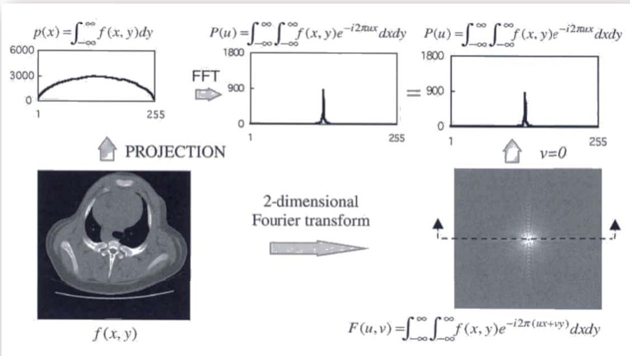

L4-28

ETH zürich

Direct Fourier Method

- Algorithm:
  - 1D FFT of the projections
  - Filtering
  - Resampling
  - 2D inverse FFT
- Resampling issues:
  - Interpolation
    - Limited accuracy
  - (Re-)gridding
    - Most accurate Fourier reconstruction method
    - Mapping by convolution with FFT of w(x,y)
  - Gridrec
    - W(x): 1D Prolate Spheroidal Wave Functions (PSWF) of zeroth order
    - W(x,y): maximally concentrated in a square region of interest
    - FFT(w(x,y)): concentrated as much as possible around 0
    - PSWF: calculated using rapidly converging expansion in terms of Legendre polynomials
    - PSWF and FFT (PSWF) can be efficiently computed and stored at run time

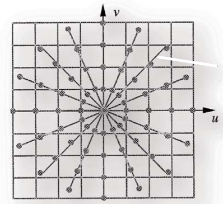

Marone et al., JSR, 2012

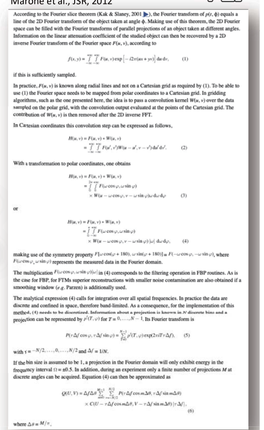

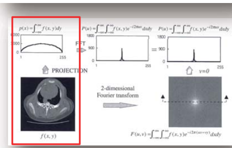

L4-29

ETH zürich

Filtered backprojection (mathematical background)

$$-\ln\left(\frac{I_\phi(r)}{I_0}\right) := P_\phi(r) = R(t,\phi) = \int_{-\infty}^{+\infty}\int_{-\infty}^{+\infty} \mu(x,y)\,\delta(x\cos\phi + y\sin\phi - t)\,dx\,dy$$

Image function: $$\mu(x,y) = \int_{-\infty}^{\infty}\int_{-\infty}^{\infty} \tilde{M}(u,v)\,e^{j2\pi(ux+vy)}\,du\,dv$$

Coordinate transform: (cartesian to polar) $$\mu(x,y) = \int_0^{2\pi} d\theta \int_0^{\infty} \tilde{M}(\omega\cos\theta,\omega\sin\theta)\,e^{j2\pi\omega(x\cos\theta+y\sin\theta)}\,|g|\,du\,dv$$

$$\text{with} \begin{cases} u = \omega\cos\theta \\ v = \omega\sin\theta \end{cases} \text{and} \quad g = \begin{pmatrix} \frac{\partial u}{\partial \omega} & \frac{\partial u}{\partial \theta} \\ \frac{\partial v}{\partial \omega} & \frac{\partial v}{\partial \theta} \end{pmatrix} = \begin{pmatrix} \cos\theta & -\omega\sin\theta \\ \sin\theta & \omega\cos\theta \end{pmatrix}$$

Fourier Slice Theorem: $$\mu(x,y) = \int_0^{2\pi} d\theta \int_0^{\infty} \tilde{P}(\omega,\theta)\,e^{j2\pi\omega(x\cos\theta+y\sin\theta)}\,\omega\,d\omega$$

Symmetry properties: $$\tilde{P}(\omega,\theta+\pi) = \tilde{P}(-\omega,\theta)$$

Image function: $$\boxed{\mu(x,y) = \int_0^{\pi} d\theta \int_{-\infty}^{\infty} \tilde{P}(\omega,\theta)\,|\omega|\,e^{j2\pi\omega t}\,d\omega}$$

A. C. Kak, M. Slaney, Principle of Computerized Tomographic Imaging", SIAM Classics in Applied Mathematics 33, New York, 2001, ISBN 0-89871-494-X

L4-30

ETH zürich

Reconstruction using backprojection (only)

- If no a priori information is known, the intensity of the object is assumed to be uniform along the beam path.
- The projection intensity is evenly distributed among all pixels along the ray path

→ Concept of backprojection!

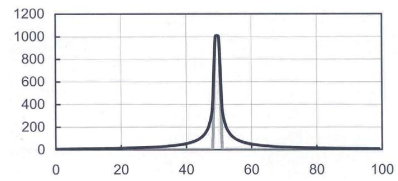

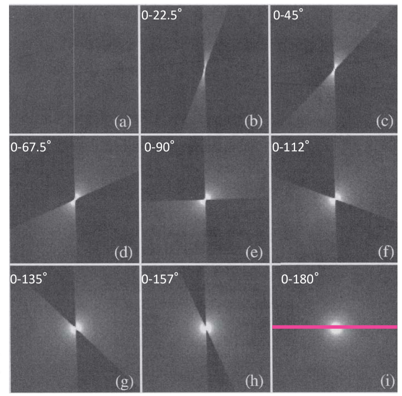

Backprojection of a point …

L4-31

ETH zürich

Image reconstruction

$$f(x,y) = \int_0^{\pi} d\theta \int_{-\infty}^{\infty} P(\omega,\theta)\,|\omega|\,e^{j2\pi\omega t}\,d\omega$$

without pre-filtering | with filtering

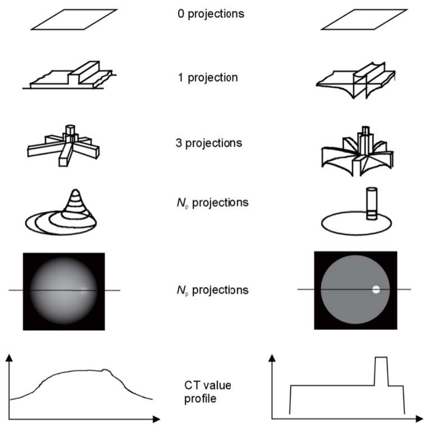

L4-32

ETH zürich

Filtered backprojection

- Image characteristic can be influenced by the choice of a convolution kernel, whereby increasing spatial resolution or edge enhancement also means increasing image noise!

original profile | **convolution kernel** | **filtered profile**

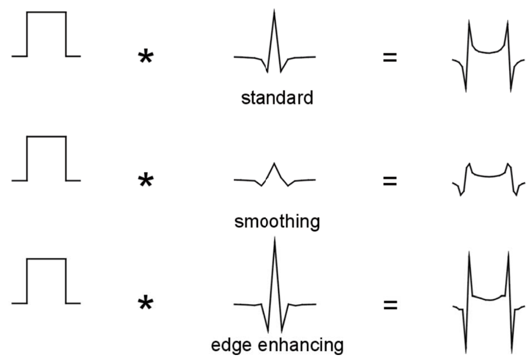

L4-33

ETH zürich

Filtered backprojection: a few hints

- Due to the high-pass nature of the ramp filter, the filtering step enhances the noise affecting the projections. As a matter of fact, the "pure" ramp filter should be employed only with almost noiseless data.
- In general, the ramp filter is multiplied with a window, that considers low frequencies and suppresses the highest frequencies to a certain extent

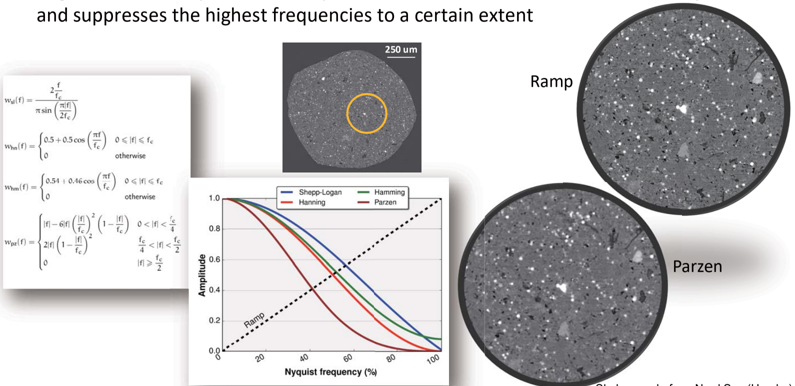

Shale sample from Nord Sea (Hornby)

L4-34

ETH zürich

FBP at work: demonstration

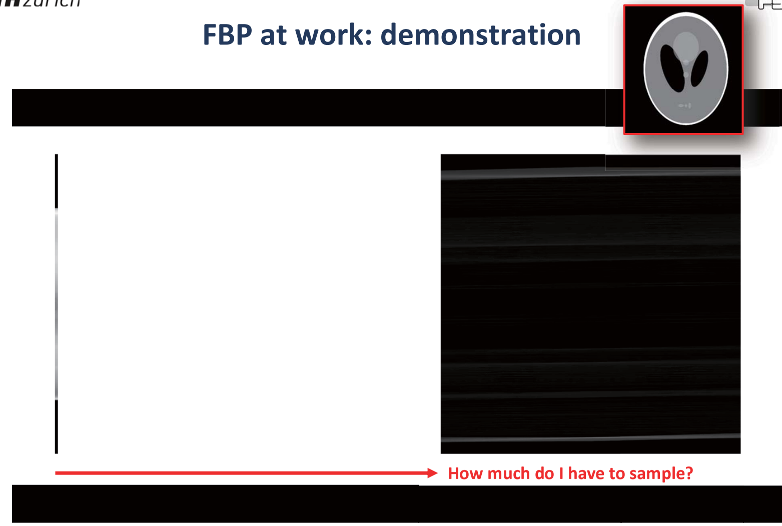

https://youtu.be/ddZeLNh9aac

L4-35

ETH zürich

Optimal sampling for FBP

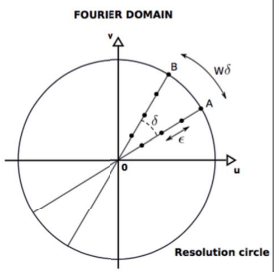

Optimal sampling condition for FBP:

$$\frac{N_{views}}{N_{pixels}} \approx \frac{\pi}{2}$$

This condition comes from setting the worst-case azimuthal resolution to be approximately the same as the radial one:

$$\epsilon \approx arc(AB)$$

$$\epsilon = \frac{2W}{N_{pixels}} = \frac{1}{\tau N_{pixels}} \qquad arc(AB) = W\delta = \frac{1}{2\tau}\frac{\pi}{N_{views}}$$

ϵ = radial resolution $arc(AB)$ = azimuthal resolution

τ = projection sampling interval $W = \frac{1}{2\tau}$ = bandwidth

N_{views} = number of projections N_{pixels} = number of projection samples

L4-36

ETH zürich

Hilbert Filter for DPC reconstruction

$$G(x,\phi) = \int_{-\infty}^{+\infty} g(x,z)dz \qquad D(x,\phi) = \int_{-\infty}^{+\infty} \frac{\partial g(x,z)}{\partial x} dz$$

$$\tilde{G}(u,\phi) = \int_{-\infty}^{+\infty}\int_{-\infty}^{+\infty} g(x,z)\cdot e^{-i2\pi ux} dxdz \qquad \tilde{D}(u,\phi) = \int_{-\infty}^{+\infty}\int_{-\infty}^{+\infty} \frac{\partial g(x,z)}{\partial x}\cdot e^{-i2\pi ux} dxdz$$

Integration per parts

$$\tilde{D}(u,\phi) = \int_{-\infty}^{+\infty}\int_{-\infty}^{+\infty} \frac{\partial g(x,z)}{\partial x}\cdot e^{-i2\pi ux} dxdz = \int_{-\infty}^{+\infty}\Big[\underbrace{\cancel{g(x,z)\cdot e^{-i2\pi ux}\big|_{-\infty}^{+\infty}}}_{\approx 0} - \int_{-\infty}^{+\infty}(-2i\pi u)\cdot g(x,z)\cdot e^{-i2\pi ux}dx\Big]dz$$

$$= 2i\pi u \int_{-\infty}^{+\infty}\int_{-\infty}^{+\infty} g(x,z)\cdot e^{-i2\pi ux} dxdz = 2i\pi u\,\tilde{G}(u,\phi)$$

$$\boxed{\tilde{G}(u,\phi) = \frac{1}{2i\pi u}\tilde{D}(u,\phi)}$$

$$\boxed{\alpha(t,\varphi) = \frac{\lambda}{2\pi}\frac{\partial\Phi(t,\varphi)}{\partial t} = \int_{-\infty}^{+\infty}\frac{\partial\delta(t,s)}{\partial t}ds}$$

Refraction of a beam transmitted through a phase object is directly proportional to the local gradient of the phase of the wave front!

$$\boxed{\mu(x,y) = \int_0^{\pi} d\theta \int_{-\infty}^{\infty} \tilde{P}(\omega,\theta)|\omega| e^{j2\pi\omega t}\, d\omega}$$

$$\boxed{\delta(x,y) = \int_0^{\pi} d\theta \int_{-\infty}^{+\infty} \tilde{D}(\omega,\theta)\frac{1}{2\pi j}\frac{|\omega|}{\omega} e^{j2\pi\omega t} d\omega}$$

Pfeiffer et al., PRL 2007

L4-37

ETH zürich

Phase vs absorption CT

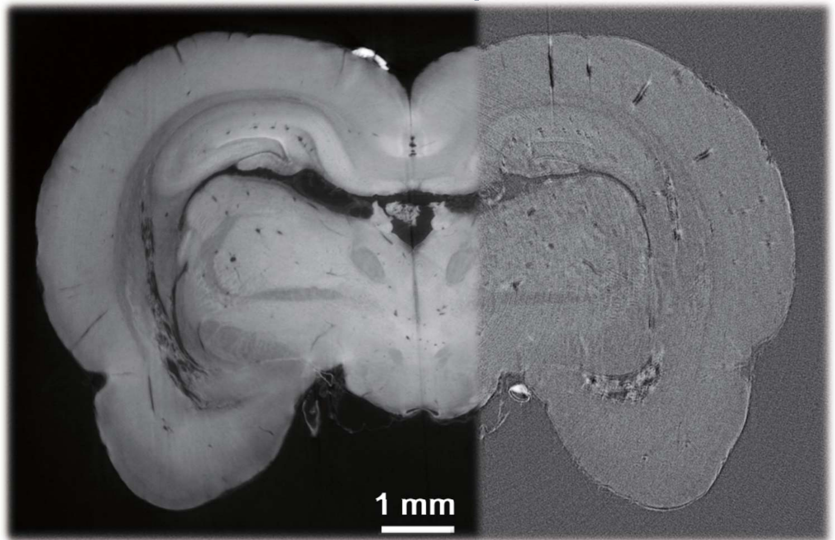

L4-38

ETH zürich

TAKE HOME MESSAGE - Algebraic Methods

Pro: Simple and fast

Req: Need large number of projections
(same order as detector pixels)

Cons: Cannot include a-priori information
(not suitable for under-sampled datasets)

L4-39

ETH zürich

Limitations of FBP: underconstrained tomograms

In many tomographic applications the following constraints are encountered:

- short acquisition times for fast evolving samples
- dose limit tolerated by the sample
- projections that cannot be acquired homogeneously in [0, 180)

$\Downarrow$

These circumstances lead to **underconstrained tomograms** that cannot be accurately reconstructed by means of FBP

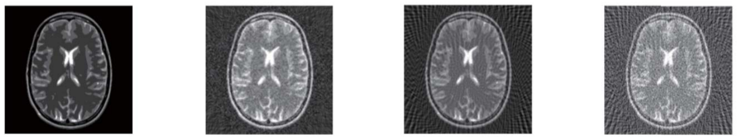

Original phantom 256 X 256 pixels | Reconstruction simulating low exposure time | Reconstruction with too few projections (50) | Reconstruction with low exposure time and few projections

L4-40

ETH zürich

Iterative algorithms

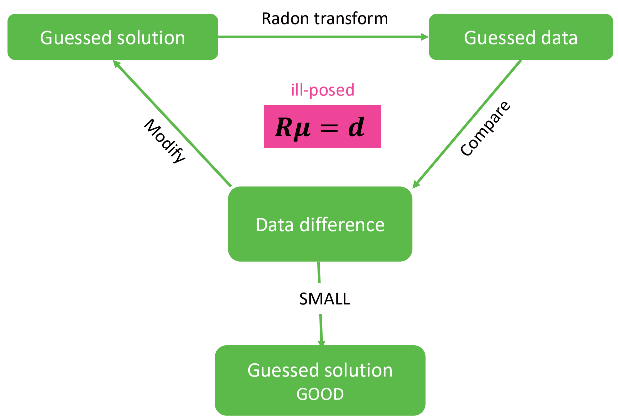

L4-41

ETH zürich

Iterative algorithms: Algebraic Reconstruction Technique (ART)

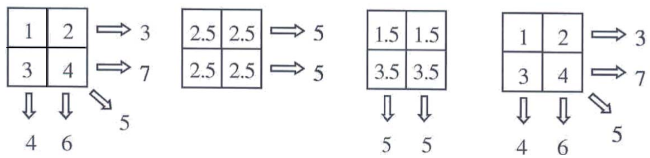

- Consider a four-block object and assign a specific attenuation value to each block (projection measurements are given).
- Assume, "a priori", an homogenous object. As initial estimate use the average of the projection samples (horizontal and vertical) which is 10/4 = 2.5.
- Calculate the line integrals of our estimated distribution along the paths used for the original projection measurement. This gives a sum of 5 along all directions.
- "Fix the raws": Compare the calculated projections against the measured values of 3 and 7: the top row is overestimated by 2 (5-3) and the bottom row is underestimated by 2 (5-7). Since, again, we have no "a priori" knowledge of the object, we assume again that the difference between the measured and calculated projections needs to be split evenly among all pixels along each ray path. Therefore we decrease the value of each block in the top row by 1 and increase the bottom row by 1.
- "Fix the columns": The calculated projections in the horizontal direction are now consistent with the measure projections. We repeat the same process for projections in the vertical directions and reach the conclusion that each element in the first column must be decreased by 0.5 and each element in the second column must be increased by 0.5.
- The calculated projections in all directions are now consistent with the measured projections (including the diagonal direction) and the reconstruction process stops.

L4-42

ETH zürich

Iterative algorithms (algebraic)

ill-posed

$$\boldsymbol{R\mu = d}$$

Optimization problem

Cost function $\quad \underset{\mu}{\operatorname{argmin}} f(\mu, d) + g(\mu)$

Fidelity term

Regularization term

- The fidelity term serves to enforce the consistency between the synthesized forward projections and the measured raw data projections throughout the iterative process.
- If one were to perform iterative reconstruction with just the data fidelity term alone, the iteration might not converge to a low-noise solution. Therefore, the regularization term is employed, usually to reduce noise while preserving spatial resolution. This is accomplished by penalizing large differences in neighboring voxels. The mathematical approach used for regularization can vary significantly.

L4-43

ETH zürich

Iterative algorithms

Optimization problem

Cost function $\quad \underset{\mu}{\operatorname{argmin}} f(\mu, d) + g(\mu)$

For DPC...

$$\boxed{f(\mu, d) = \frac{1}{2}\left\| R\frac{\partial\delta}{\partial x} - d \right\|_2^2}$$

Fidelity term

Regularization term

- Stability
- A priori knowledge

Algebraic methods (ART,...) $\quad f(\mu, d) = \frac{1}{2}\|R\mu - d\|_2^2 \quad g(\mu) = 0$

Tikhonov
small norm $\quad g(\mu) = \lambda\|\mu\|_2^2$

Lasso
for sparse data $\quad g(\mu) = \lambda\|\mu\|_1$

$$\|\mathbf{x}\|_p := \left(\sum_{i=1}^{n} |x_i|^p\right)^{1/p}$$

Total Variation (TV)
piecewise constant, edge preserving... $\quad g(\mu) = \lambda\|\nabla\mu\|_1$

L4-44

ETH zürich

Iterative algorithms - statistical

$$\boldsymbol{\bar{N}_i = N_0^i \cdot e^{-[R\mu]_i}}$$

N – expected photon counts
i – each pixel in each view

Optimization problem

Cost function $\quad \underset{\mu}{\operatorname{argmin}} f(\mu, d) + g(\mu)$

Fidelity term

Regularization term

Probabilistic description of the imaging process: number of photons as a random variable, assumed Poisson distributed.

Negative log-likelihood $\quad L(\mu|N) = \sum_i N_i \log \bar{N}_i - \bar{N}_i$

→ Evaluating the probability that an image "belongs" to the input data

L4-45

TAKE HOME MESSAGE - Iterative Methods

Pros:

- Can include *a-priori* information
- Flexible – can model almost anything
- Suitable for under-sampled datasets

Cons:

- Computational intensive
- Highly dataset specific
- Needs to tune (lots of) parameters

L4-46

References – Computed tomography

- A. C. Kak, M. Slaney, Principle of Computerized Tomographic Imaging", SIAM Classics in Applied Mathematics 33, New York, 2001, ISBN 0-89871-494-X
- F. Natterer, "The Mathematics of Computerized Tomography", SIAM Classics in Applied Mathematics 32, Philadelphia 2001, ISBN 0-89871-493-1
- W. A. Kalender, "Computed Tomography – Fundamentals, System Technology, Image Quality, Applications", 2nd revised edition, 2005, Publicis Corporate Publishing, ISBN 3-89578-216-5
- J. Hsieh, Computed Tomography: Principles, Design, Artifacts and Recent Advances, SPIE Press Monograph, ISBN 0-8194-4425-1

Tutorial 5

(16:40 – 17:10)

Fabrication technology of gratings

Christian David

Paul Scherrer Institut,

Switzerland

L5-1

Christian David, Paul Scherrer Institut, Switzerland

Fabrication technology of gratings

XNPIG2019 Tutorial Session, Sendai, Japan, October 20, 2019

L5-2

Outline

- Basic considerations and design parameters
- The early years of grating fabication
- Gratings for neutrons
- Gratings for hard x-rays
- Alternative approaches for grating fabrication
- The best grating is no grating?

L5-3

Basic considerations and design parameters

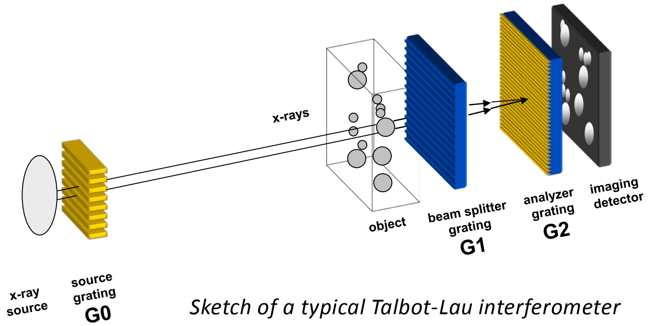

Sketch of a typical Talbot-Lau interferometer

Purpose of the gratings: detect small changes in the propagation of x-rays by:

- *refraction due to differences in phase shift => **phase contrast imaging***
- *small-angle scattering => **dark-field imaging***

Angular sensitivity depends on grating periods => **micron pitches**

F. Pfeiffer, T. Weitkamp, O. Bunk, and C. David, *Nature Physics* **2** (2006) p. 258-261

L5-4

Basic considerations and design parameters

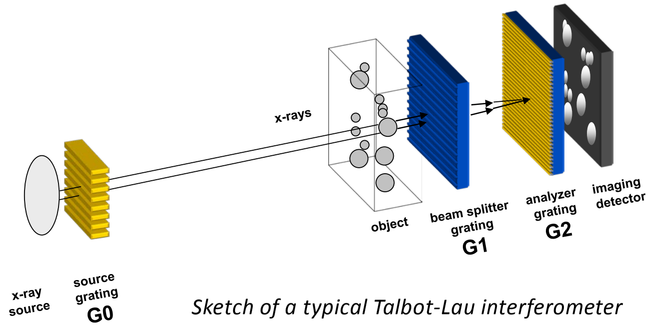

Sketch of a typical Talbot-Lau interferometer

Grating	Interaction with x-rays	typ. materials	typ. pitch	size
G0	high absorbtion	Au, Ir, Pb, W, ...	p0: many µm	small
G1	π-phase shifting (or $\pi/2$)	Si, Ni	p1: few µm	field of view (FOV)
G2	high absorbtion	Au, Ir, Pb, W, ...	p2: few µm	larger than FOV

F. Pfeiffer, T. Weitkamp, O. Bunk, and C. David, *Nature Physics* **2** (2006) p. 258-261

L5-5

PAUL SCHERRER INSTITUT

Early years of grating fabrication

(When photons were soft)

L5-6

PAUL SCHERRER INSTITUT

G1 gratings

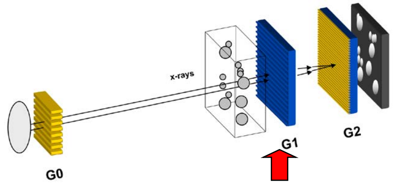

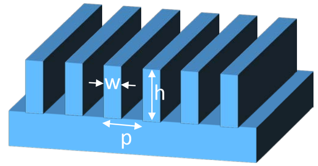

Requirements:

- Size limits field of view
- Periods p of a few microns
- Low zero[th] order efficiency

- Low absorption
- Duty cycle DC = w/p = 0.5
- Introduce phase shift of π

- <u>Grating lines with high aspect ratio AR = h/w</u>

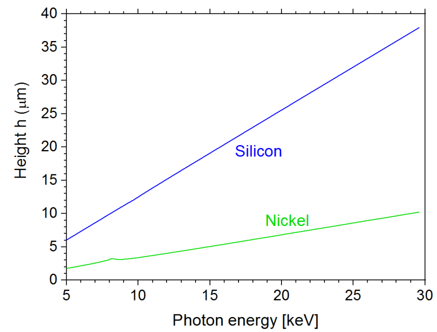

Calculated structure height to give π-phase shift

L5-7

PAUL SCHERRER INSTITUT

Silicon phase gratings – fabrication by wet etching

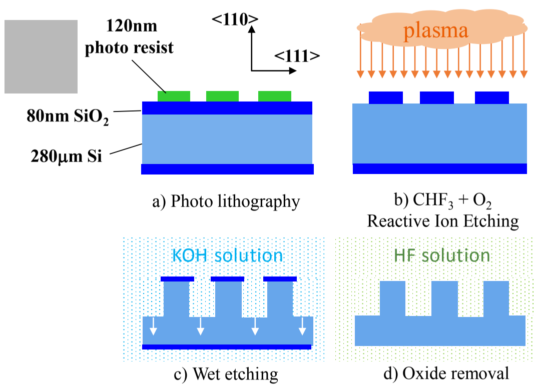

Anisotropic etching of <110> oriented Si gives vertical side walls with <111> orientation

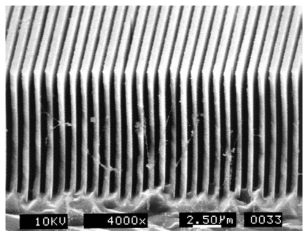

First silicon gratings for x-ray phase imaging, p = 1 µm, h = 12 µm

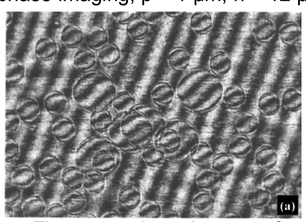

First x-ray phase images of latex spheres, E = 12.4 keV

C. David, B. Nöhammer, H.H. Solak, E. Ziegler, *Applied Physics Letters* **81** (2002) 3287

L5-8

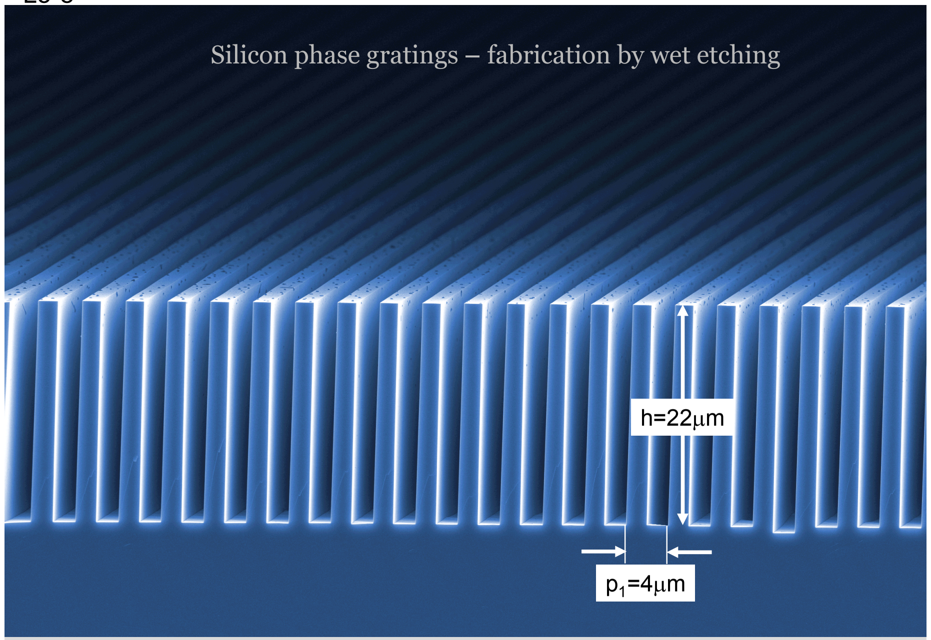

C. David, et al. *Microelectron. Eng.* **84** (2007) 1172

L5-9

Silicon phase gratings – fabrication by wet etching

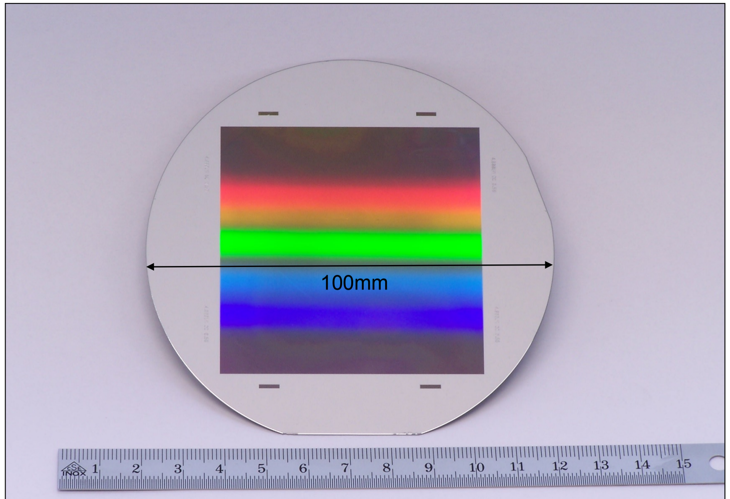

64mm x 64mm Si beam splitter grating, p = 4μm

C. David, et al. *Microelectron. Eng.* **84** (2007) 1172

L5-10

Gold absorber gratings

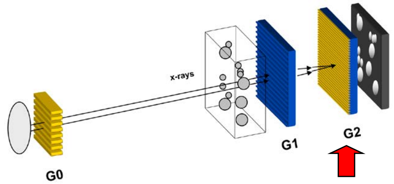

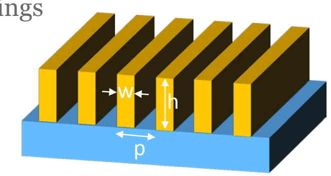

Requirements:

- Size limits field of view
- Periods 2x smaller than phase grating
- Duty cycle typ. DC = 0.5
- High absorption required

- Grating lines with very high aspect ratio AR = h/w

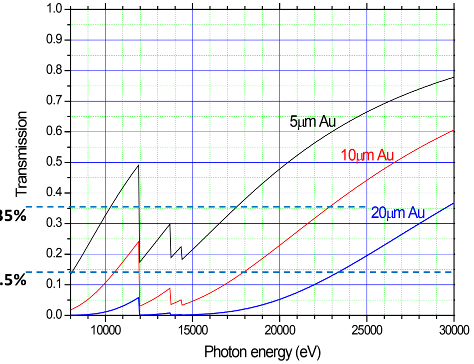

C. David, et al. *Microelectron. Eng.* **84** (2007) 1172

L5-11

Gold absorber gratings

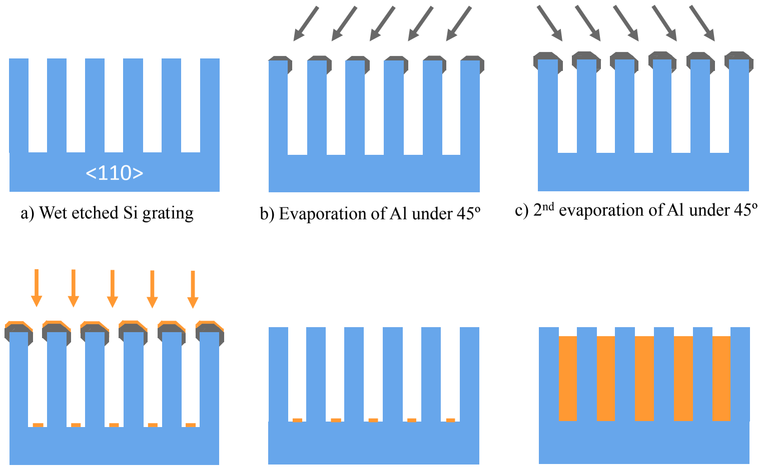

a) Wet etched Si grating

b) Evaporation of Al under 45°

c) 2nd evaporation of Al under 45°

d) Normal evaporation of Au

e) Al etching, lift-off

f) Electroplating of Au

C. David, et al. *Microelectron. Eng.* **84** (2007) 1172

L5-12

Gold absorber gratings

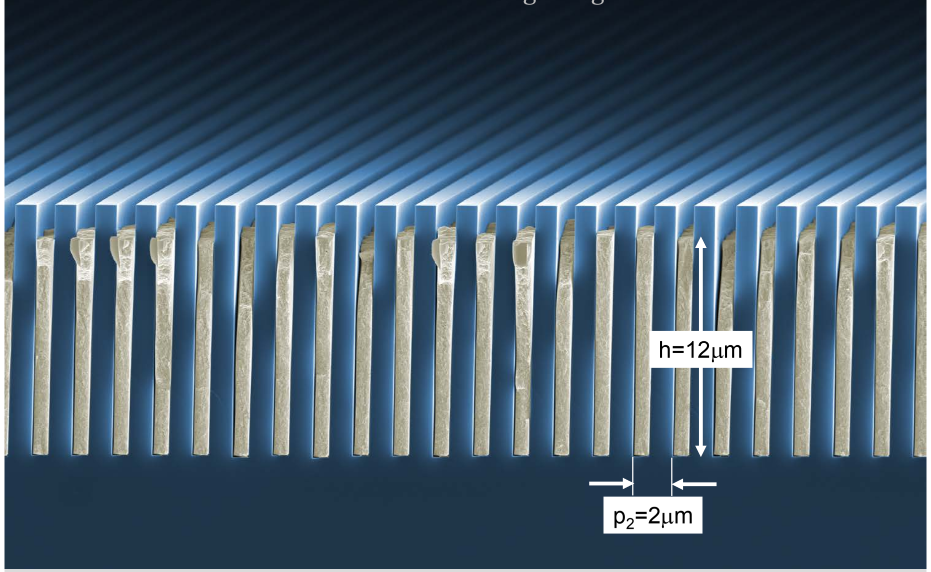

C. David, et al. *Microelectron. Eng.* **84** (2007) 1172

L5-13

Gold absorber gratings

Problem:
Aspect ratio (AR) is limited by precision of Au plating base deposition

=> limited by grating size to AR ~10

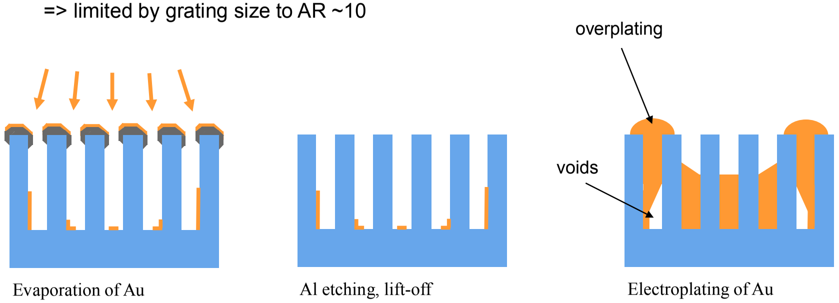

L5-14

Gold absorber gratings – line doubling

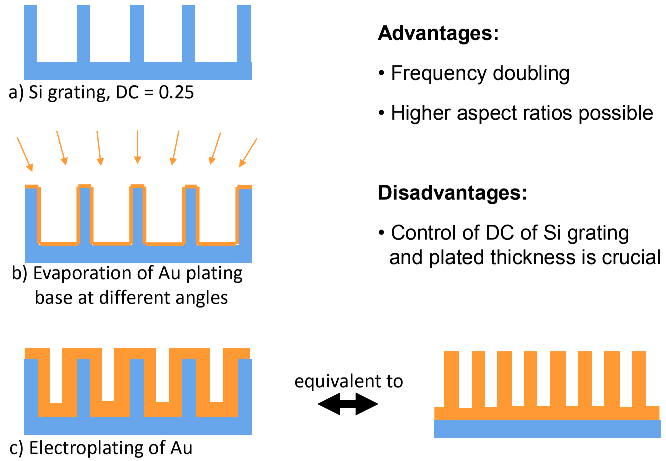

Advantages:

- Frequency doubling
- Higher aspect ratios possible

Disadvantages:

- Control of DC of Si grating and plated thickness is crucial

L5-15

Gold absorber gratings – line doubling

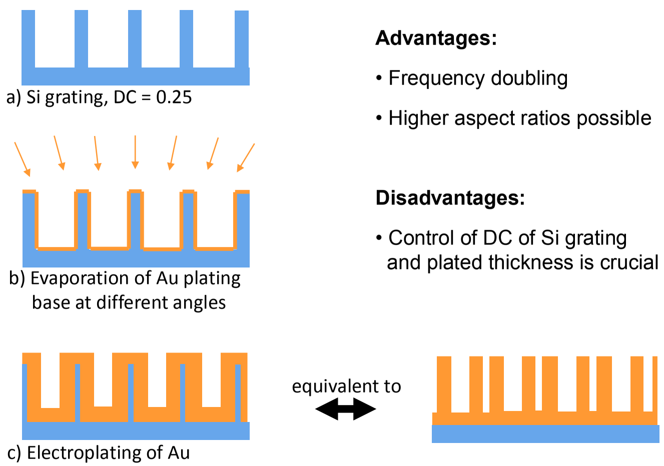

Advantages:

- Frequency doubling
- Higher aspect ratios possible

Disadvantages:

- Control of DC of Si grating and plated thickness is crucial

L5-16

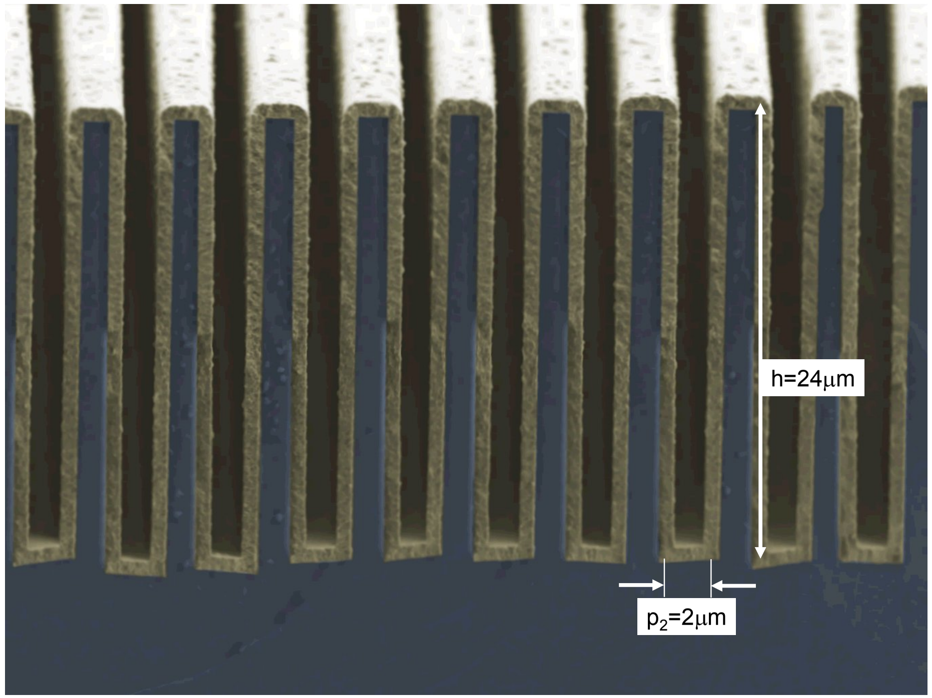

L5-17

Gratings for neutrons
(easier than we thought)

L5-18

Gratings for neutrons

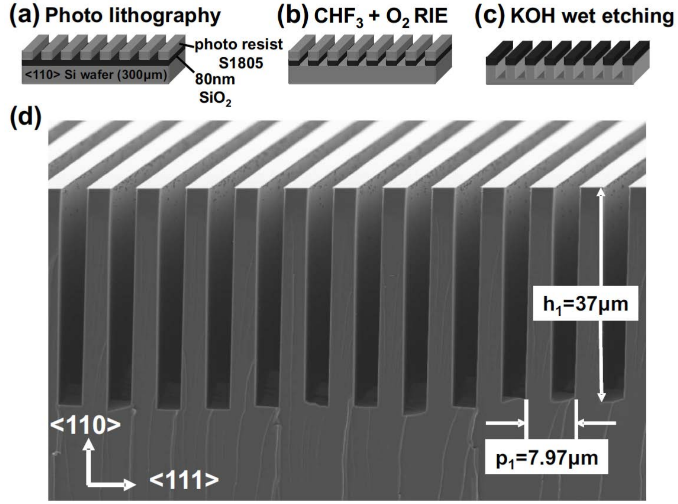

At λ = 4.1 Å, the neutron π-shift length for Si is 37 μm

C. Grünzweig, F. Pfeiffer, O. Bunk, T. Donath, G. Kühne, G. Frei, M. Dierolf, C. David, *Rev. Sci. Instrum.* **79** (2008) 053703

L5-19

Gratings for neutrons

At λ = 4.1 Å, the neutron 1/*e* length for Gd is 3 μm

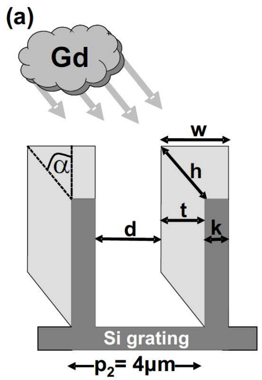

For progress on neutron gratings see XNPIG session VII, Tuesday afternoon

C. Grünzweig, F. Pfeiffer, O. Bunk, T. Donath, G. Kühne, G. Frei, M. Dierolf, C. David, *Rev. Sci. Instrum.* **79** (2008) 053703

L5-20

Gratings for hard x-rays
(when things become much, much more difficult)

L5-21

High photon energies require high structures

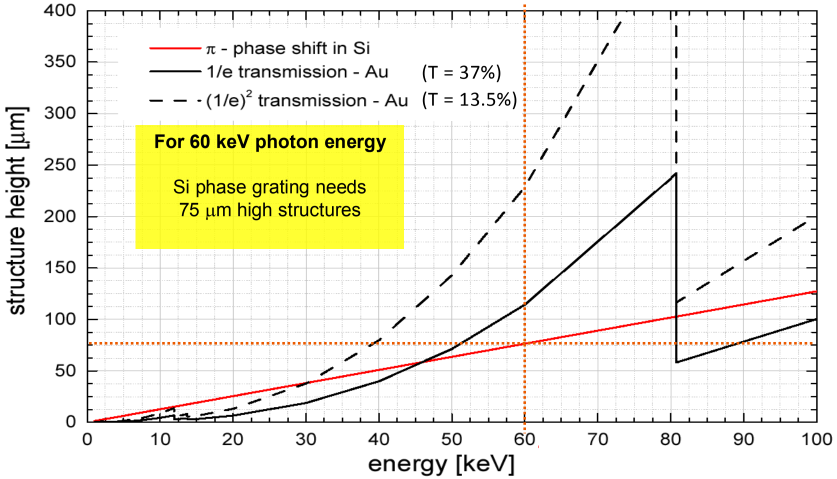

Structure heights for phase gratings and absorber gratings

Courtesy F. Pfeiffer

L5-22

Silicon phase gratings – fabrication by wet etching

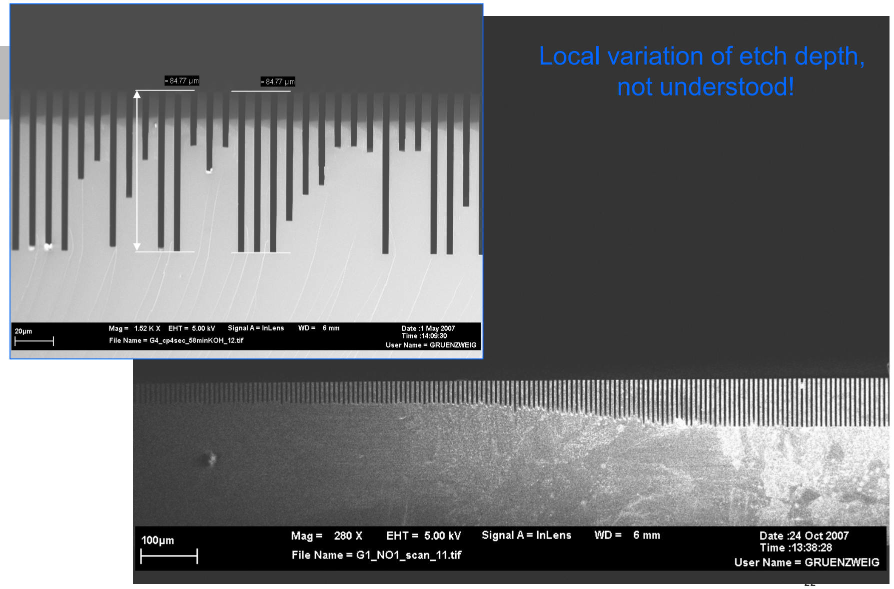

L5-23

Bosch plasma etching process

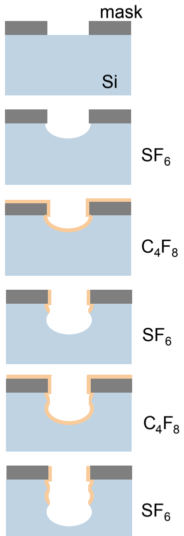

Courtesy of K. Jefimovs

- 2 step plasma etching process
- Etching: SF_6
- Passivation: C_4F_8
- variables: etching/passivation times, gas flows, temperature, pressure, RF/ICP power

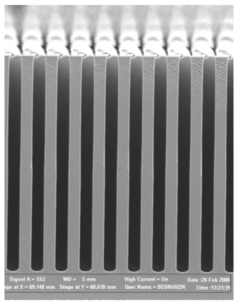

Silicon phase grating, p = 8.5 µm, h = 75 µm, AR = 17.5
(by M. Bednarzik)

T. Donath, Review of Scientific Instruments **80** (2009) p. 053701-4

L5-24

Bosch plasma etching process

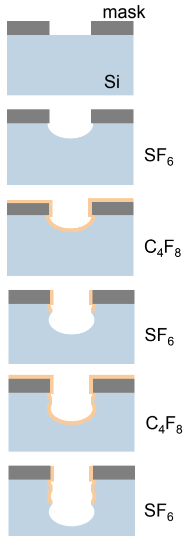

Courtesy of K. Jefimovs

- 2 step plasma etching process
- Etching: SF_6
- Passivation: C_4F_8
- variables: etching/passivation times, gas flows, temperature, pressure, RF/ICP power

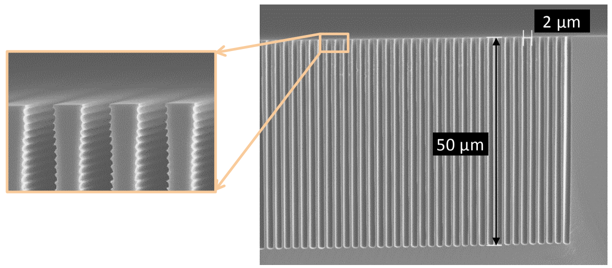

Silicon phase grating,
p = 2 µm, h = 50 µm, **AR = 50**
(recent results by K. Jefimovs)

K. Jefimovs et al., *Proc. SPIE* **10146**, 101460L (2017), M. Kagias et al., *Phys. Rev. Lett.* **116**, 093902 (2016)

L5-25

Bosch plasma etching process

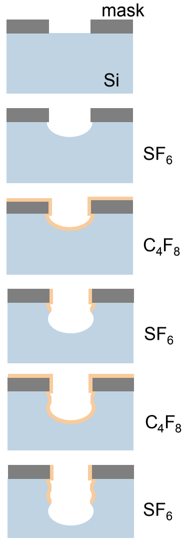

Courtesy of K. Jefimovs

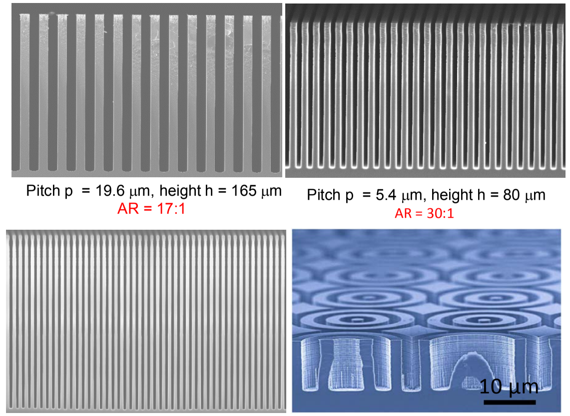

Pitch p = 19.6 µm, height h = 165 µm
AR = 17:1

Pitch p = 5.4 µm, height h = 80 µm
AR = 30:1

Pitch p = 1.0 µm, height h = 30 µm
AR = 60:1

Grating for 2D-omnidirectional hard-X-ray dark field imaging

K. Jefimovs et al., XNPIG2019, Poster P8, Monday 21 Oct., 17:00
M. Kagias et al. XNPIG2019, Session XI, Thursday, 24 Oct., 9:50
J. Vila-Comamala et al., XNPIG2019, Session X, Wednesday, 23 Oct., 11:40

K. Jefimovs et al., *Proc. SPIE* **10146**, 101460L (2017), M. Kagias et al., *Phys. Rev. Lett.* **116**, 093902 (2016)

L5-26

Metal assisted chemical etching (MACE)

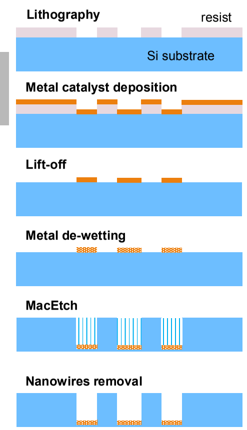

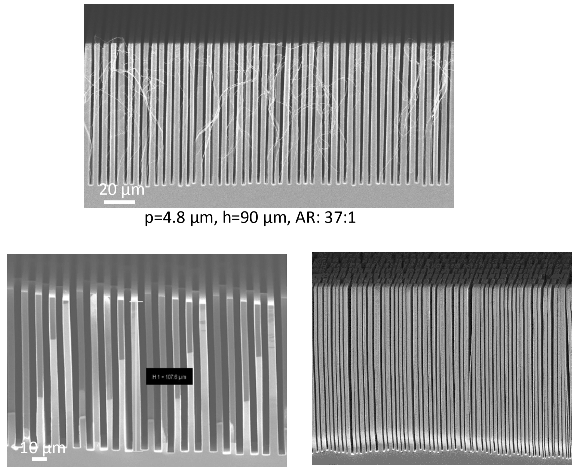

p=4.8 µm, h=90 µm, AR: 37:1

p=10 µm, h=107 µm, AR= 21:1
(after nanowires removal)

p= 400 nm, h=18 µm, AR >90:1

L. Romano et al., XNPIG2019, Session XI (INVITED), Thursday, 24 Oct., 9:00

L. Romano et al., *RSC Advances* **6** (2016) 16025, L. Romano et al., *Microelectron. Eng.* **177**, 59-65 (2017)

L5-27

High photon energies require high structures

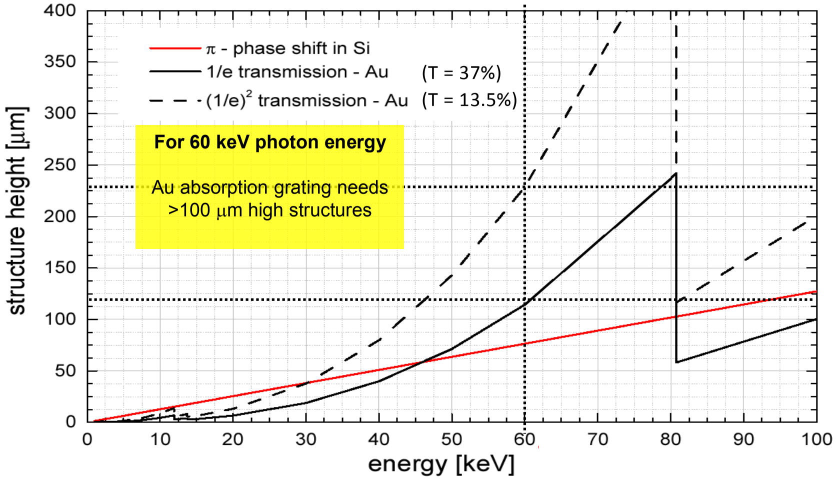

Structure heights for phase gratings and absorber gratings

Courtesy F. Pfeiffer

L5-28

Au gratings for high photon energies

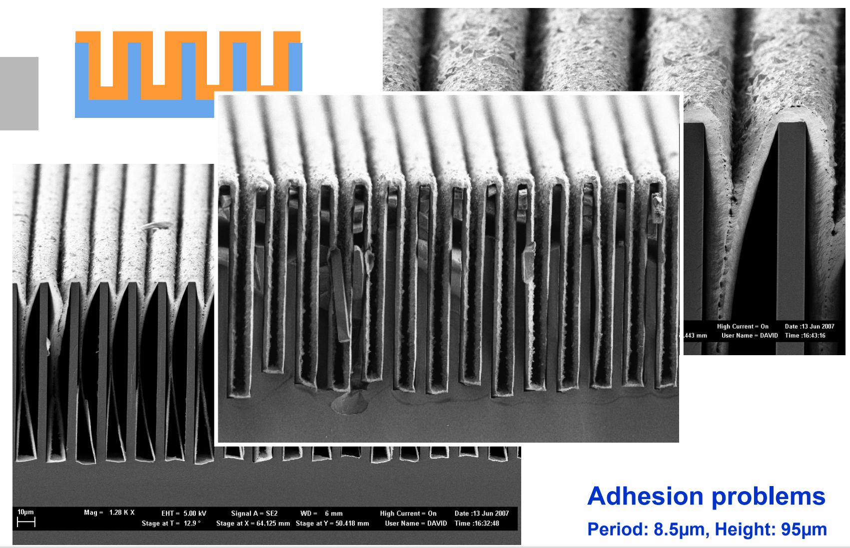

Adhesion problems

Period: 8.5µm, Height: 95µm

T. Donath, *Review of Scientific Instruments* **80** (2009) p. 053701-4

L5-29

PAUL SCHERRER INSTITUT PSI

Seedless Au electroplating

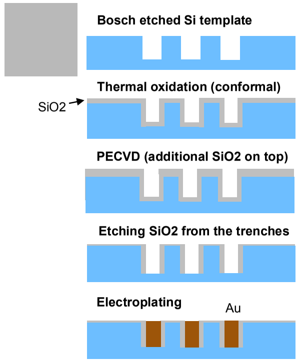

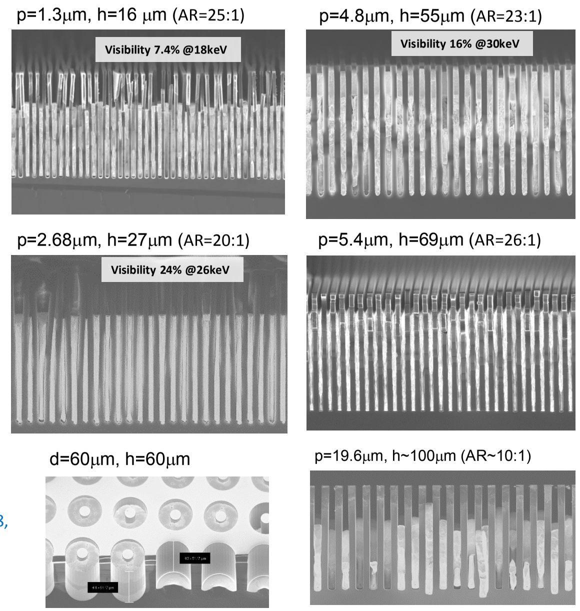

D. Noda, et al., AIP Conference Proceedings **1466**, 187 (2012)
K. Jefimovs et al., XNPIG2019, Poster P8, Monday 21 Oct., 17:00
M. Kagias et al., *Mater. Sci. Semicond. Process.* **92** (2019) 73-79

L5-30

PAUL SCHERRER INSTITUT PSI

Metal casting

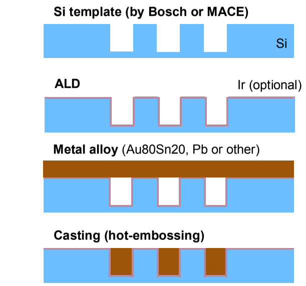

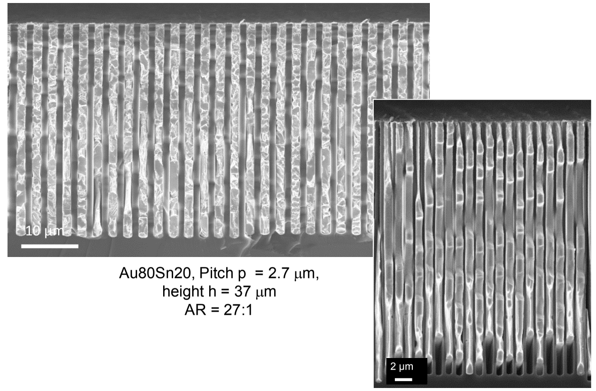

Au80Sn20, Pitch p = 2.7 µm, height h = 37 µm AR = 27:1

Pb95In5, p = 1.2 µm Height = 30 µm, AR = 50:1

L. Romano et al., XNPIG2019, Session XI (INVITED), Thursday, 24 Oct., 9:00

L. Romano et al., *Microelectron. Eng.* **176** (2017) 6-10, L. Romano et al., *J. Vac. Sci. Technol. B* **35** (2017) 06G302

L5-31

PAUL SCHERRER INSTITUT PSI

Fabrication of gratings by Silicon RIE and Iridium ALD

Atomic layer deposition for iridium to coat the silicon structures.

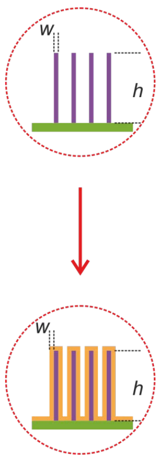

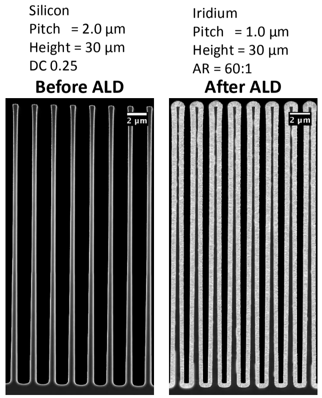

J. Vila-Comamala et al., XNPIG2019, Session X, Wednesday, 23 Oct., 11:40
M. Kagias et al. XNPIG2019, Session XI, Thursday, 24 Oct., 9:50

J. Vila-Comamala et al., *Microelectron. Eng.* **192** (2018) 19-24

L5-32

PAUL SCHERRER INSTITUT PSI

The LIGA technique

Karlsruhe Institute of Technology

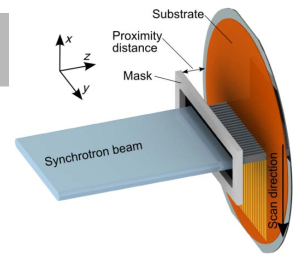

LIGA technology developed at KIT

- Thick resist layers (PMMA, SU8, ...) are exposed with x-rays through a mask of Au absorbers
- Resist is developed and filled by electroplating
- High penetration and low scattering of x-rays allows for fabrication of µm structures with <u>extreme aspect rations</u> (AR > 100)
- **Very successful technique for grating fabrication**

Schematic view of the process steps of the LIGA process.

J. Mohr, et al., AIP Conference Proceedings **1466** (2012) 41

L5-33

The LIGA technique

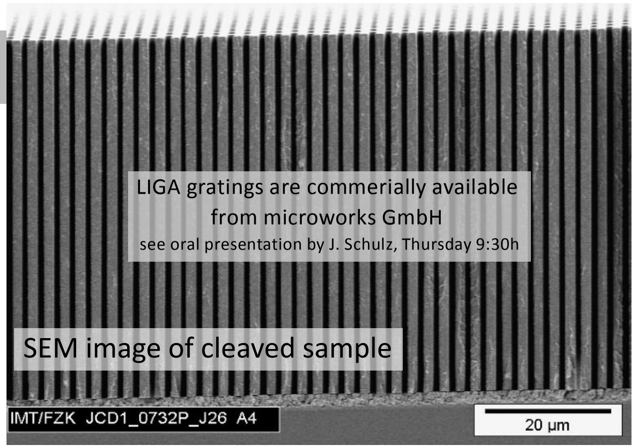

- Pitch: 2.4 µm
- Height: 60 µm
- Pattern area: 60 x 20 mm^2

Made by LIGA technology at IMT, Karlsruhe Institute of Technology

E. Reznikova, J. Mohr, M. Börner et al., Microsyst. Technol. **14** (2008) 1683

L5-34

Bent gratings made at KIT

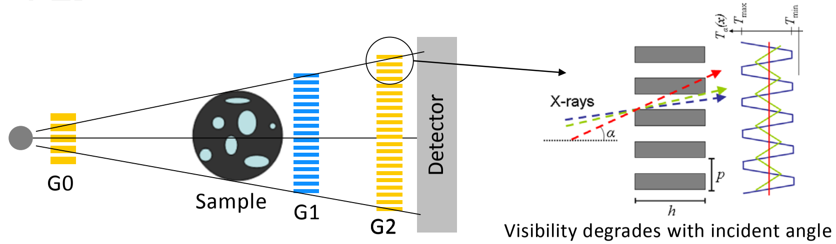

T. Thüring, P. Modregger, T. Grund, J. Kenntner, C. David, and M. Stampanoni, Appl. Phys. Lett. **99**, 041111 (2011)

L5-35

Bent gratings made at KIT

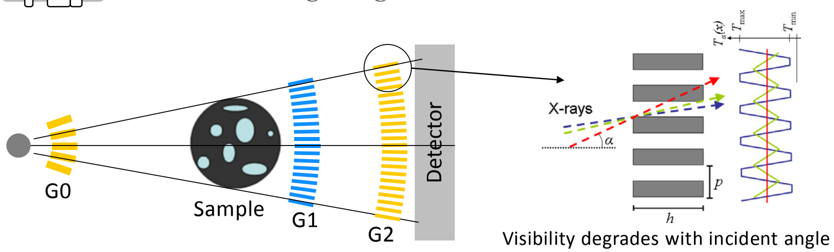

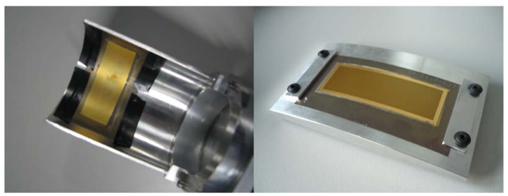

Gratings made by KIT on flexible titanium substrates.
Right: G0 grating with 30 mm radius. Left: G2 grating

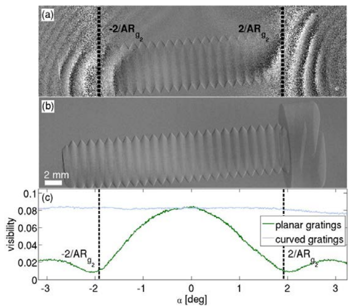

T. Thüring, P. Modregger, T. Grund, J. Kenntner, C. David, and M. Stampanoni, Appl. Phys. Lett. **99**, 041111 (2011)

L5-36

Alternative approaches for grating fabrication

L5-37

PAUL SCHERRER INSTITUT

Fabrication of Go gratings by metal stacking

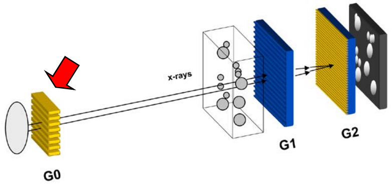

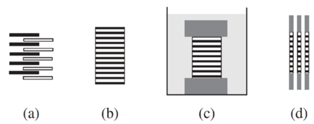

Fig. 2. Illustration of fabrication by the stacked-sliced method: Heavy and light metal foils (a) are stacked alternately (b); then, the stack is sandwitched between Cu blocks and fixed with solder (c). Finally, the entire body is sliced and polished (d).

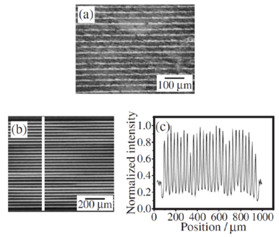

Fig. 3. (a) Optical microscopy image of the surface of the multiple slit in which the dark lines denote Ta and white lines denote Al. (b) X-ray projection image of the multiple slit measured using a micro-focus W source. (c) Normalized intensity profile on the white line in (b).

Alternative fabrication method for G0 gratings

- Stacking of absorbing and transparent metal foils (Ta, 20 µm thick and Al, 10 µm thick)
- Pressing, fixation, cutting and polishing
- Results in G0 gratings with 30 µm pitch and 600 µm thickness

K. Wan, Y. Takeda, W. Yashiro and A. Momose, *Jpn. J. Appl. Phys.* **47** (2008) 7412

L5-38

PAUL SCHERRER INSTITUT

Patterned scintillator

- Grating interferometry becomes problematic for high photon energies
  => low absorption in G0
  => low visibility
- Idea: replace absorbing G0 by a grating of scintillator lines

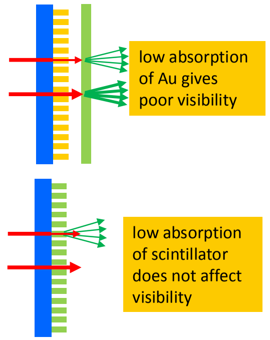

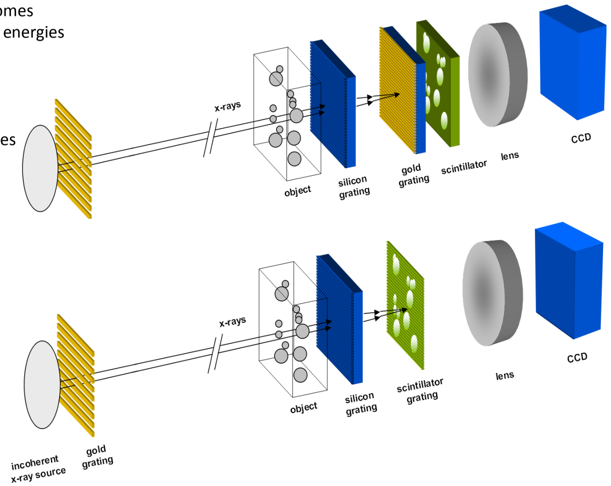

S. Rutishauser, I. Zanette, T. Donath, A. Sahlholm, J. Linnros, and C. David, *Appl. Phys. Lett.* **98**, 17 [2011], 171107

L5-39

PAUL SCHERRER INSTITUT

Patterned scintillator

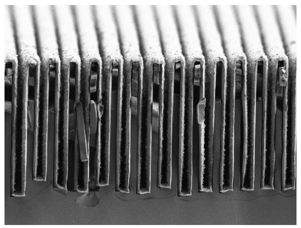

Au analyzer grating, p=8.5 µm, h=95 µm

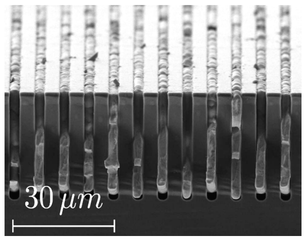

CsI analyzer grating, p=8.5 µm, h=30 µm
(made by Scint-X, Stockholm)

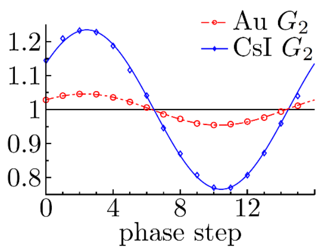

- Comparison of Au G2 grating and CsI G2 grating at x-ray tube, E=60 keV
- 4x improved visibility (Au grating: 5.5%, CsI grating: 22.0%)
- CsI G2 had much worse efficiency (could be improved, and may not be relevant in synchrotron applications)

S. Rutishauser, I. Zanette, T. Donath, A. Sahlholm, J. Linnros, and C. David, *Appl. Phys. Lett.* **98**, 17 [2011], 171107

L5-40

PAUL SCHERRER INSTITUT

Planar grating geometry

Planar geometry:

- X-rays propagate parallel to grating substrates
- Allows for «unlimited» aspect ratio of gratings
- Fan-like grating lines for strongly divergent setups can be easily implemented

Ideally suited for compact setup and high photon energies

- FOV in vertical direction is limited to structure height

Scanning setup

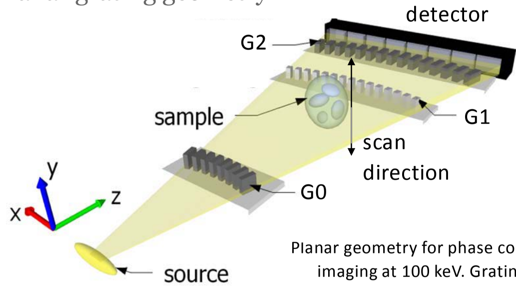

Planar geometry for phase contrast imaging at 100 keV. Gratings are made by LIGA technology

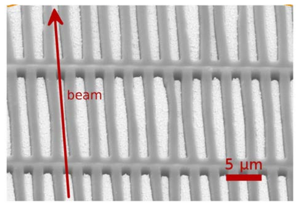

SEM image of grating (by Microworks GmbH). Height h=100 µm, pitch p2=2.8 µm.

T. Thüring, et al., *Scientific Reports* **4** (2014) 5198

L5-41

Gratings made by multilayer deposition

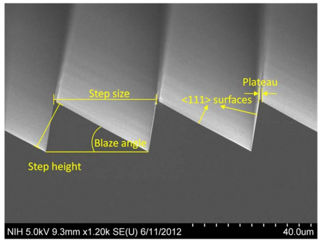

Anisotropic wet etching of silicon

- Fabrication of gratings with very small pitches and very high aspect ratios
- Anisotropic etching of Si substrate to form «staircase»
- Deposition of Si/W multilayer with 200 nm pitch
- Extreme aspect ratios can be made (AR > 200)
- Implementation of three identical gratings in a P-P-P configuration

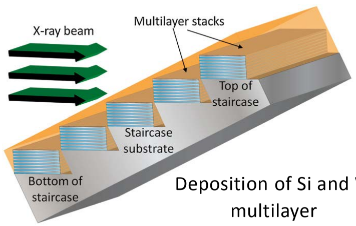

Deposition of Si and W multilayer

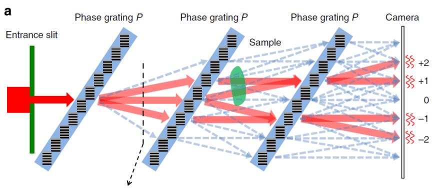

Schematic view of a P-P-P grating interferometer

Lynch, S. K. et al., *J. Micromech. Microeng.* **22** (2012) 105007, H. Wen, et al., *Nature Comms.* **3659** (2013)

L5-42

The best grating is no grating?

L5-43

The best grating is no grating?

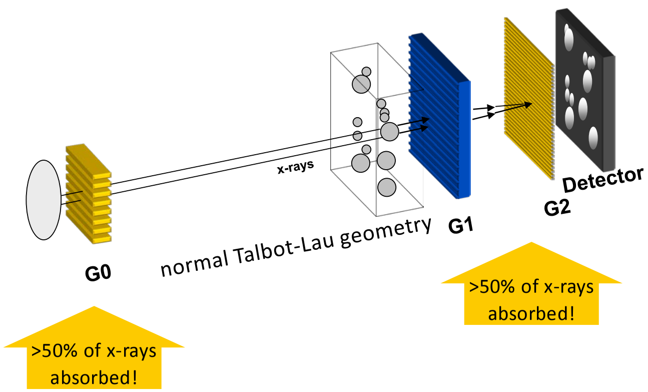

>75% of photons are absorbed in G0 & G2

How can we get rid of them?

T. Donath, et al., *Journal of Applied Physics* **106** (2009) 054703

L5-44

Setup without G2

«Inverse geometry»:

- l << d
- p2 >> p0
  The grating with biggest area has biggest pitch
- Interference fringes become big enough to be resolved by detector
- G2 is no longer required!

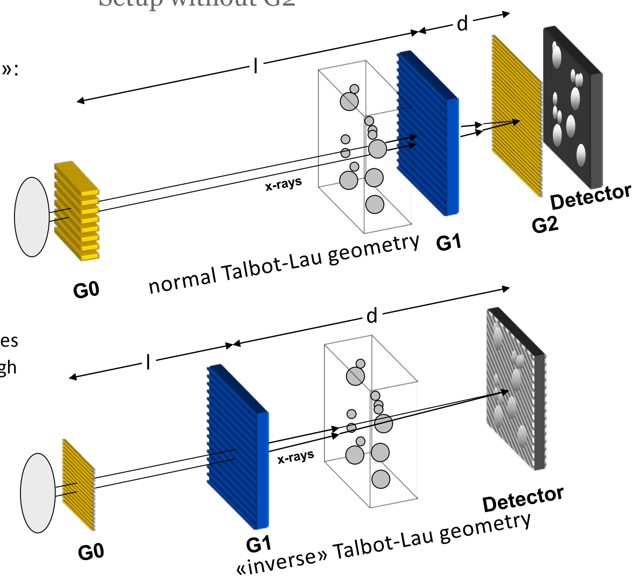

L5-45

Setup without G0 – structured anode of x-ray tube

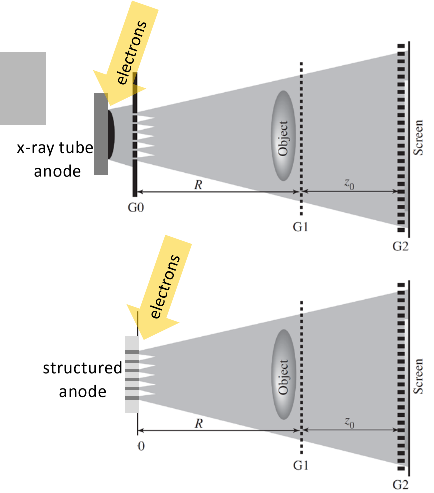

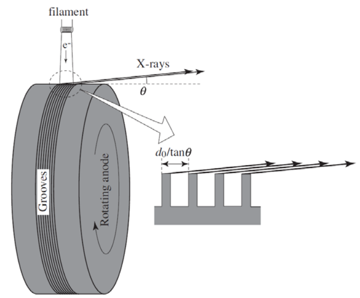

Fig. 2. Structure of multi-line X-ray source. Grooves are made on a rotating anode, and only the X-rays from the area between the grooves are used.

For progress on structures sources see XNPIG session X, Wednesday morning

A. Momose, W. Yashiro, H. Kuwabara, and K. Kawabata, Jap. J. Appl. Phys. **48** (2009) 076512

L5-46

Setup without G0 and without G2

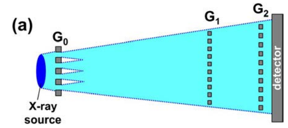

Conventional Talbot-Lau geometry with G0, G1, and G2

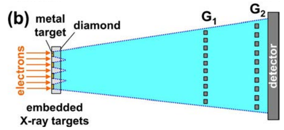

Geometry with structured anode and G1 & G2

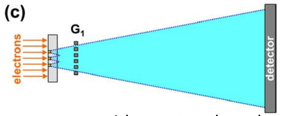

Inverse geometry with structured anode and G1

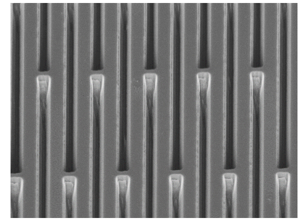

Structured diamond substrate, P0 = 3 µm (PSI, in collaboration with Sigray Inc.)

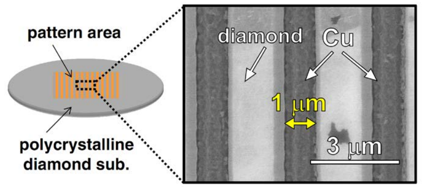

Fig. 2. Scanning electron micrograph of the multiline Cu targets embedded in the polycrystalline diamond substrate.

For progress on structures sources see XNPIG session X, Wednesday morning

N. Morimoto, S. Fujino, K. Ohshima, J. Harada, T. Hosoi, H. Watanabe, and T. Shimura, *Opt. Lett.* **39**(15) 4297-4300 (2014)

L5-47

Summary and conclusion

- Gratings for x-ray phase contrast imaging require:
  - Small pitch for angular sensitivity
  - High contrast for x-rays

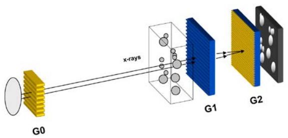

- Lithographic techniques have been developed based on wet-etching, dry etching, and x-ray lithography (LIGA).

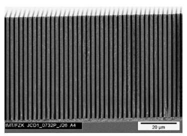

- Gratings for hard x-rays become very challenging due to extreme aspect ratios.
  Alternative strategies are pursued.

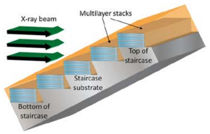

- New developments towards making absorber gratings (G0, G2) obsolete.